Effects of Surface Parameters on Boiling Heat Transfer Phenomena

by

Bao Hoai Truong

B.S. Nuclear Science and Engineering, B.S. Physics, 2007
M.S. Nuclear Science and Engineering, 2008
Massachusetts Institute of Technology

SUBMITTED TO THE DEPARTMENT OF NUCLEAR SCIENCE AND ENGINEERING
IN PARTIAL FULFILLMENT OF THE REQUIREMENTS FOR THE DEGREE OF

DOCTOR OF PHILOSOPHY IN NUCLEAR SCIENCE AND ENGINEERING
AT THE
MASSACHUSETTS INSTITUTE OF TECHNOLOGY

MAY 2011
[JUNE 2011]

Signature of Author: _____
Bao Hoai Truong
Department of Nuclear Science and Engineering
May 19, 2011

Certified by: _____
Lin-Wen Hu - Thesis Supervisor
Associate Director, MIT Nuclear Reactor Laboratory

Certified by: _____
Jacopo Buongiorno - Thesis Co-supervisor
Associate Professor of Nuclear Science and Engineering

Certified by: _____
Tom McKrell - Thesis Co-supervisor
Research Scientist, Nuclear Science and Engineering

Certified by: _____
Peter Griffith - Thesis Reader
Professor Emeritus, Mechanical Engineering

Certified by: _____
Mujid Kazimi
TEPCO Professor of Nuclear Science and Engineering
Chair, Department Committee on Graduate Students

Effects of Surface Parameters on Boiling Heat Transfer Phenomena

by

Bao Hoai Truong

Submitted to the Department of Nuclear Science and Engineering
on May 19, 2011 in Partial Fulfillment of the
Requirements for the Degree of Doctor of Philosophy in
Nuclear Science and Engineering

ABSTRACT

Nanofluids, engineered colloidal dispersions of nanoparticles in fluid, have been shown to enhance pool and flow boiling CHF. The CHF enhancement was due to nanoparticle deposited on the heater surface, which was verified in pool boiling. However, no such work has been done for flow boiling. Using a cylindrical tube pre-coated with Alumina nanoparticles coated via boiling induced deposition, CHF of water was found to enhance up to 40% compared to that of the bare tube. This confirms that nanoparticles on the surface is responsible for CHF enhancement for flow boiling. However, existing theories failed to predict the CHF enhancement and the exact surface parameters attributed to the enhancement cannot be determined.

Surface modifications to enhance critical heat flux (CHF) and Leidenfrost point (LFP) have been shown successful in previous studies. However, the enhancement mechanisms are not well understood, partly due to many surface parameters being altered at the same time, as in the case for nanofluids. Therefore, the remaining objective of this work is to evaluate separate surface effect on different boiling heat transfer phenomena.

In the second part of this study, surface roughness, wettability and nanoporosity were altered one by one and respective effect on quenching LFP with water droplet was determined. Increase in surface roughness and wettability enhanced LFP; however, nanoporosity was most effective in raising LFP, almost up to 100°C. The combination of the micro posts and nanoporous coating layer proved optimal. The nanoporous layer destabilizes the vapor film via heterogeneous bubble nucleation, and the micro posts provides intermittent liquid-surface contacts; both mechanisms increase LFP.

In the last part, separate effect of nanoporosity and surface roughness on pool boiling CHF of a well-wetting fluid, FC-72, was investigated. Nanoporosity or surface roughness alone had no effect on pool boiling CHF of FC-72. Data obtained in the literature mostly for micro-porous coatings showed CHF enhancement for well wetting fluids, and existing CHF models are unable to predict the enhancement.

Thesis Supervisor: Lin-wen Hu, PhD, PE
Title: Associate Director, MIT Nuclear Reactor Laboratory

Thesis Supervisor: Jacopo Buongiorno, PhD
Title: Associate Professor of Nuclear Science and Engineering

Thesis Supervisor: Tom McKrell, PhD
Title: Research Scientist

Thesis Reader: Peter Griffith, PhD
Title: Professor Emeritus, Mechanical Engineering

Acknowledgements

Dr. Lin-wen Hu: Thank you for your support over all these years. Your suggestions on my thesis work and your real-world advice have been invaluable. Thank you for all the opportunities for conferences and summer internships, all of which have widened my perspectives. I have learned a lot from you.

Professor Jacopo Buongiorno: You have taught me so much since I was a sophomore in college. It has been a great pleasure to be one of your students, both in class and in the laboratory. Your technical guidance and advice have always helped me to understand the material in class and in the laboratory much better. Your advice on career paths and options are invaluable. All of these have prepared me well to go into the real world. It has been a great pleasure and an honor for me.

Dr. Tom McKrell: Thank you for all your guidance in the laboratory. Your expertise, your ideas and encouragement have been invaluable for me to complete all my experimental work in the laboratory. It has been a lot of fun working with you and I especially enjoyed the non-work related conversations we had from time to time.

Dr. Hyung-dae Kim: Thank you for starting the quenching work and for your guidance/collaboration thorough the project to help me finish it up. It has been an honor for me to take part in this project. I would not be able to include this part of work in my thesis without you.

Professor Griffith: Thank you for reading my thesis and providing constructive critique on my work. It is an honor for me.

Professor Kazimi: Thank you for sitting on my thesis committee, and for the opportunities and advice you have provided over my years at MIT.

Dr. Sung Joong Kim: Thank you for helping me with the flow boiling CHF work. Your advice and expertise in operating the CHF loop help me to sail smoothly with the experiments.

Professor Rubner: Thank you for allowing me to use the layer by layer coating facility.

To my sponsors, in particular the Electrical Power Research Institute, the Nuclear Engineering University Program Fellowship, the Nuclear Regulatory Commission fellowship and Doug Spreng, for supporting my projects over these years.

To the MTL staff, in particular Kurt Broderick and Scott Poesse: You have been tremendous in helping me start my work in the clean room to make surfaces for my experiments. Your help and guidance have always been valuable.

To the Schlumberger engineers, in particular Mike Subb, Albert Perez and Roy Koveleski, for assisting and letting me use the Confocal microscope for the surface characterization.

To the NRL machine shop staff, in particular Josh and Adam: thank you for letting me use the machines and providing advice for machining the parts for my experiments.

To the students in nanofluid groups, in particular Greg DeWitt, Bren Phillips, Eric Forrest, Vivek Sharma and Harry O' Hanley: Thank you for all your support and encouragement over the years. I enjoyed discussing with you about different experiments. It have been a pleasure working with all of you over the years. Bren, thank you for helping me with the LBL coating and the porosity measurement. I wish you all the best of luck in your future studies.

Thank you Heather, Peter, Clare and all the NSE administrative staff to make things go smoothly over these past many years.

To all members of the NSE Intramural teams I have been in: Thank you for playing and letting me play. IM sport has always been a great part of my graduate student life at MIT. Good luck with the future teams.

To all my friends, in particular Clara, Dustin, Bo, Karl, Thuy-Tien, Greg, Matt D., Natalie, Frank, Nhien, Koroush, Lan-Anh, Stefano, Isaiah, Tri, Vivek, Joe F., Joe Y., Eugeny, Bren, Paul, Jacob D., Jenn T., Susanna, Brittany, Caroline, Tom, Jayodita, Roshni, Matt Z. and anyone I may have inadvertently missed. Thank you for all the fun, good conversations and company for all these years.

To Chelsea: Thanks for helping with the final editing of my thesis. More importantly, thank you for making this past year a lot of fun and meaningful. Love you!

To my family: Mom, Dad, Be and Gai. Thank you for all the love and support my entire life. I would not be here without you guys. I love you all!

I dedicate this work the ones I love.

Table of Contents

1 INTRODUCTION 13
1.1 Background 13
1.2 Literature Review 14
1.2.1 Nanofluid Boiling Heat Transfer 14
1.2.2 Quenching Heat Transfer with Nanofluids 16
1.2.3 Nano-Micro Engineering Surfaces for Heat Transfer Enhancement 18
1.3 Thesis Objectives and Motivations 22
1.4 Thesis Outline 23
2 PRE-COATED SUBCOOLED FLOW BOILING CHF 24
2.1 Introduction to Flow Boiling CHF of Nanofluids 24
2.2 Flow CHF Experimental Facilities and Procedure 24
2.2.1 Experimental Loops 24
2.2.2 Experimental Procedure 32
2.2.3 Flow Boiling Performance of Alumina and Alumina + PAH Coatings 34
2.3 Surface Characterization 46
2.3.1 SEM Images 46
2.4 Analysis of Surface Parameters Affecting Flow Boiling CHF 56
2.4.1 Effect of Wettability on Flow Boiling CHF 56
2.4.2 Effect of Porosity on Flow Boiling CHF 59
2.5 Summary of Pre-coated CHF Experiments 62
3 SURFACE EFFECTS ON QUENCHING LEIDENFROST POINT 63
3.1 Introduction 63
3.2 Experiments 66
3.2.1 Surface Preparation 66
3.2.2 Measurement of LFP 69
3.3 Results 70
3.4 Data Interpretation 73
3.5 Conclusions 75
4 SEPARATE SURFACE EFFECTS ON CRITICAL HEAT FLUX 76
4.1 Introduction 76
4.2 Experiments 76
4.2.1 CHF Experimental Matrix and Facility Design Considerations 76
4.2.2 Experimental Facility, Procedure and Uncertainty Analysis 80
4.3 CHF Results and Surface Characterization 85
4.3.1 CHF Results 85
4.3.2 Boiling Curves 89
4.4 Surface Characterization 92
4.5 Conclusions 98
5 ANALYSIS OF EFFECT OF SURFACE PARAMETERS ON CHF 99

5.1 Existing CHF Models 99
5.1.1 Hydrodynamic Instability Theory 99
5.1.2 Macrolayer Dryout Theory 100
5.1.3 Dynamic Microlayer Theory 102
5.1.4 Bubble Interaction Theory 102
5.1.5 Hot/dry Spot CHF Theory 103
5.1.6 Summary 104
5.2 Effect of Surface Roughness on CHF 105
5.2.1 Surface Roughness Enhancing Heat Transfer Area and Wettability 105
5.2.2 Effect of Surface Roughness on Macrolayer Thickness 106
5.3 Effect of Porosity on CHF 107
5.3.1 CHF Models and Data for Porous Surface 108
5.3.2 Effect of Porous Coating Parameter on CHF 116
5.4 Summary 121
6 CONCLUSIONS AND FUTURE WORK 122
6.1 Conclusions 122
6.2 Recommendations for Future Work 123

Table of Figures:

Figure 2-1: Schematic of the Pre-coating Loop 25
Figure 2-2: Schematic Test Section Assembly (left), Photo (right) 26
Figure 2-3: Representative Temperature Profiles during a Coating Process 30
Figure 2-4: Representative Heat Flux Profile during a Coating Process 30
Figure 2-5: Flow Boiling Two-Phase CHF Loop – Schematic (adopted from Kim [2]). 31
Figure 2-6: Typical Heat Flux Profile in a CHF Experiment 33
Figure 2-7: Picture of Burn-out and Intact Test Sections 33
Figure 2-8 Temperature vs. Heat Flux for a Typical CHF Experiment with a Bare Test section 36
Figure 2-9: Heat Transfer Coefficient as a Function of Heat Flux for Bare Test Sections 38
Figure 2-10: Comparison of Current Data to those of Kim [2] and Look Up Table Values [50] 40
Figure 2-12: Measured Heat Transfer Coefficient of Test Sections C19Al to 21Al at G = 2500 kg/m^{2}s 42
Figure 2-14: Measured Heat Transfer Coefficient of Test Sections at G = 1500 kg/m^{2}s (bare data is from S.J. Kim [2]) 43
Figure 2-15:Measured Heat Transfer Coefficient of Test Sections C31AlPAH and C32AlPAH at G = 2500 kg/m^{2}s 44
Figure 2-16: Heat Transfer Coefficient Ratio of Alumina Coated Test Section (C7Al to C13Al) to a Bare Test Section at G = 2500 kg/m^{2}s 44
Figure 2-17: Heat Transfer Coefficient Ratio of Alumina Coated Test Section (C19Al to C21Al) to a Bare Test Section at G = 2500 kg/m^{2}s 45
Figure 2-18: Heat Transfer Coefficient Ratio of Alumina/PAH Coated Test Section (C27AlPAH to C39PAH) to a Bare Test Section at G = 2500 kg/m^{2}s 45
Figure 2-19: SEM Images (~5000X) of Test Section C1Al to C6Al 46
Figure 2-20: SEM Images (~1000x) of Alumina Coated Test Sections 48
Figure 2-21:SEM images (~10000X) and their associate EDS spectrum 49
Figure 2-22: SEM images(~1000x) of Alumina/PAH Pre-coated Test Sections and Some of Their Associate EDS Spectra 50
Figure 2-23: SEM images (~1000x) of PAH Pre-coated Test Sections and Some of Their Associate EDS Spectra 51
Figure 2-24: Representative Contact Angle of Water on Bare and Pre-coated Test Sections 53
Figure 2-25: Representative Confocal Images of Flow Boiling Test Sections (256μm by 256 μm) 55
Figure 2-26: Force Balance for Liquid-Vapor Interface in Flow Boiling per Kandlikar's Model 57
Figure 2-27: Flow Boiling CHF Dependence on Contact Angle 58
Figure 2-28: Liquid and vapor flow path in viscous-drag choking limit model 60
Figure 2-29: CHF as Function of Particle Diameter Based on Liter and Kaviany model 61
Figure 3-1: Photolithography - Deep Reactive Ion Etching Process 67
Figure 3-2: SEM Images of Surface With Micron-Size Posts 67
Figure 3-3: SEM images of fabricated samples for LFP tests: (a) smooth Au layer; (b) 15 μm posts on smooth Au layer; (c) 15 μm posts on smooth SiO_2 layer; (d) layer-by-layer

(LBL) SiO_2 layer. Insets show static contact angle on the fabricated samples for 10-μL water droplets on (a) smooth Au (83°), (b) Au with micro-posts (83°), (c) SiO_2 layer (19°), (d) nano-porous SiO_2 layer (~0°). 68
Figure 3-4: Schematic of Quenching Facility to Measure LFP 69
Figure 3-5: Water droplet evaporation time vs. surface temperature. The nominal uncertainty in the measurement of the LFP temperature was found to be less than ±5°C. 71
Figure 3-6: Effect of Surface Roughness on LFP of Au Coated Surfaces..... 71
Figure 3-7: Effect of Roughness on LFP of Smooth SiO_2 Coated Surfaces..... 72
Figure 3-8: Effect of Roughness on Surface with Nanoporous SiO_2 (LBL) Coating..... 72
Figure 3-9: Photographs of evaporating water droplets on test surfaces held at 400°C: (a) Au without posts; (b) Au with 15 μm posts; (c) SiO_2 with 15 μm posts; (d) nano-porous SiO_2 layer with 15 μm posts. Arrows show location of droplet-to-surface bridging by liquid filaments. 73
Figure 4-1: Pool Boiling CHF Facility- Left: Photograph of Entire Facility; Right: Schematic 81
Figure 4-2: Schematic of Heater Assembly - Left: Isometric view; Right: Front View... 82
Figure 4-3: Typical Surface Temperature and Heat Flux Profile in CHF Experiment..... 83
Figure 4-4: Uncertainty in Surface Heater Temperature Measurement From Experiment to Experiment 85
Figure 4-5: Boiling Curves of LBL Coated Surfaces Compared to Plain (Bare) Surfaces 89
Figure 4-6: Boiling Curves of Surfaces with 5 μm Posts Compared to Plain (Bare) Surfaces 90
Figure 4-7: Boiling Curves of Surfaces with 200 μm Posts Compared to Plain (Bare) Surfaces 90
Figure 4-8: Boiling Curves of Surfaces with 5μm Posts and LBL Compared to Plain (Bare) Surfaces 91
Figure 4-9: Boiling Curves of Surfaces with 200μm Posts and LBL Compared to Plain (Bare) Surfaces 91
Figure 4-10 : SEM Images of Surface with Posts and LBLB - Left (5 μm); Right (200 μm). Top: Single post (LBL). Center: Array of Posts; Bottom: Single posts with LBL.. 93
Figure 4-11: SEM of a Smooth Wafer (bottom) and LBL Coated Wafer (top) 94
Figure 4-12: Representative Contact Angle Measurement 95
Figure 4-13: Representative Confocal Image for Surface Used in CHF Tests 96
Figure 4-14: FIB Images - Left: Cross Sectional Cut Are; Right: The Porous Structure. 97
Figure 5-1: Vapor Mushroom and the Liquid Macrolayer 101
Figure 5-2: Effect of Particle Diameter and Porosity on CHF of FC-72 109
Figure 5-3: Effect of Particle Diameter on CHF - Lu & Chang Model [100] 112
Figure 5-4: Effect of Vapor Channel on CHF by Mori & Okuyama Model [101]..... 113
Figure 5-5: Effect of Modulated Wavelength on CHF - Liter and Kaviany Model [60] 115
Figure 5-6: Effect of Particle Diameter on CHF Enhancement for Refrigerants 117
Figure 5-7: Effect of Thickness on CHF Enhancement for Refrigerants 117
Figure 5-8: Effect of Thickness to Diameter Ratio on CHF Enhancement for Refrigerants 118
Figure 5-9: Effect of Particle Diameter on CHF Enhancement for Water 119

Figure 5-10: Effect of Coating Thickness on CHF Enhancement for Water..... 119
Figure 5-11: Effect of Thickness to Diameter Ratio on CHF Enhancement for Water.. 120
Figure 5-12: Effect of Porosity on CHF Enhancement for Porous Coating Surface..... 120

List of Tables:

Table 1-1: List of Previous Nanofluids Study on CHF in Pool and Flow Boiling 15
Table 2-2: CHF Values of Water Measured Using Bare Test Sections (No Coating) 34
Table 2-3: Water CHF with Alumina nanoparticle Pre-coated Test Sections at G = 2500 kg/m^2s 39
Table 2-4: Water CHF with Alumina nanoparticle Pre-coated Test Sections at G = 1500 kg/m^2s 40
Table 2-5: Water CHF with PAH/Alumina Particle Pre-coated Test Sections at G = 2500 kg/m^2s 41
Table 2-6: Contact Angle Measurement (±5°) for Pre-coated Test Sections 52
Table 2-7: Confocal Microscopy Results (Average Values of Two Locations) 54
Table 3-1: Summary of LFP of Water for Tested Surfaces (°C) 70
Table 4-1 : Desired CHF Experimental Matrix 77
Table 4-2 : Comparison of Water and Refrigerants for CHF Experiments 78
Table 4-4: Critical Heat Flux of FC-72 for Plain Surface 86
Table 4-5 : CHF Values of Surface with 25 LBL layers of SiO_2 nanoparticle 87
Table 4-6: CHF Values of Surface with Posts (500 μm pitch) 88
Table 4-7 : Surface with Posts and 25 LBL layers of SiO_2 nanoparticles 88
Table 4-8 : Summary of Average CHF of FC-72 and surface roughness for All Surfaces 88
Table 4-9: Summary of Contact Angle of FC-72 on Different Surfaces (Uncertainty: ±3°) 94
Table 4-10: Summary of Confocal Data for Surface Roughness 95

Nomenclature:

A_{surf}	Surface area (m^2)
A_w	Wetted area(m^2)
A_v	Vapor channel area (m^2)
c_v	Kinematic viscosity ratio (liquid to vapor)
c_ρ	Density ratio (liquid to vapor)
C	Constant in Biance model
C_E	Ergun coefficient
C_j	Constant in Liter model
D	Diameter of tube (m)
d_p	Particle diameter (m)
f	Amount of water in nanofluid dilution
f'	Empirical function of saturation in Udell model
F	Force per unit length in Kandlikar model (N/m)
e	Thickness of thin film layer
g	Gravitational constant (m^2/s)
G	Mass flux (kg/m^2s)
h	Heat transfer coefficient (W/m^2K)
h_{fg}	Latent Heat of Evaporation (J/kg)
H	Height of micro post (m)
I	Current (A)
k_h	Tube thermal conductivity (W/m-K)
L	Length of test section (m)
n	Amount of x w% nanofluid
	Number of vapor escape channel
N	Number of micro posts
Nu	Nusselt number
P	Pressure (Pa)
q''	Heat flux (W/m^2)
r	Radius (m)
	Roughness factor
	Cone base radius (m)
r_{eff}	Effective pore radius (m)
Ra	Raleigh number
	Surface roughness (m)
Rz	Surface roughness parameter (m)
R_{bg}	Breakthrough radius (m)
s	Side of heater (m)
	Saturation factor in Udell model
s_{cone}	Length of side on cone (m)
S	Suppression factor in Chen corr.
t	Thickness (m)
T	Temperature (C)
U	Uncertainty
v_g	Critical Helmholtz Velocity (m/s)
v_1	Volumetric flow rate of bubbles (m^3/s)
V	Voltage (V)
V_{red}	Reduced volume (m^3)
V_{pore}	Volume of pores in porous coating (m^3)
x	Weight percent of original nanofluid
X	Flow quality
y	Volumetric fraction of desired nanofluid

Greek Symbols

β	Ratio of kinematic viscosity
δ_c	Macrolayer thickness (m)
δ_s	Thickness of coating (m)
ϵ	Porosity
ϵ_S	Base to surface area ratio
γ	Surface tension (N/m)
κ	Permeability (m^2)
	Constant in Kim model
λ	Taylor instability wavelength (m)
λ_D	Size of square unit cell (m)
	Most dangerous wavelength (m)
λ_m	Modulated wavelength (m)
μ	Viscosity (Pa-s)
ν	Specific volume (m^3/kg)
ν_v	Vapor kinematic viscosity (m^2/s)

ω	Dimensionless value in Udell model
ϕ	Angle of orientation of heater
ρ	Density (kg/m^3)
σ	Surface tension (N/m)
τ_D	Hovering time for bubble (s)
θ_R	Receding contact angle (°)
ξ	Volumetric ratio of liquid to bubble

Subscript

CHF	Critical heat flux
f	Fluid
g	Gas
i	Inner
l	Liquid
nb	Nucleate boiling
o	Outer
p	Post
sat	Saturation
si	Silicon
SL	Solid-liquid
LV	Liquid Vapor
v	vapor
w	wall

Abbreviation

CHF	Critical heat flux
EDM	Electron Discharge Machine
HTC	Heat transfer coefficient
LBL	Layer by Layer
LUT	Look up table
PAH	Polyallylamine hydrochloride
SEM	Scanning Electron Microscopy
SS316	Stainless Steel 316

1 Introduction

1.1 Background

Most current nuclear reactors use water as the heat transport fluid due to its high heat capacity as well as natural abundance. In the Boiling Water Reactor (BWR), the water boils inside the core and turns into steam. In the Pressurized Water Reactor (PWR), the outlet water temperature does not reach saturation during normal operation because of the higher operating pressure. However, subcooled boiling can occur along the fuel. In transient conditions, boiling at elevated heat flux can lead to dryout in a BWR and departure of nucleate boiling in a PWR. These two conditions occur at the critical heat flux (CHF), one of most important safety limits for nuclear reactor design and operation. During CHF, the fuel clad is exposed to a continuous layer of vapor, causing the heat transfer coefficient to drop tremendously, usually leading to fuel/clad failure. Therefore, CHF is one of the important limits for reactor power. Everything else being equal, enhancing CHF allows more power output from the reactor.

Techniques to enhance CHF have been researched for many years. Both passive (e.g. fin, wire wraps, groove surfaces, additives to fluid) and active (e.g. vibration, electrostatic field, suctions) techniques have been employed to enhance CHF, according to Rohsenow et al. [1]. Recently, nanofluids, engineered colloidal dispersion of nanoparticles (e.g. metals, metal oxides, carbon, diamond) in common base coolant fluids such as water, refrigerants or oil, have been shown to provide pool boiling CHF enhancement more than 200%. However, the amount of nanoparticle in the nanofluid is often so diluted (less than 1.0% by volume (1%vol)) such that the thermophysical properties of the nanofluids are essentially identical to those of the base fluid. Therefore, researchers have suggested that the change in the heater surface due to the deposition of the nanoparticle during boiling process is responsible for the CHF enhancement. Most of the CHF work for nanofluid has been done in pool boiling conditions. Only few experiments in flow CHF conditions have been done. One of those studies was done at MIT with mass flux up to 2500 kg/m^2s, and CHF enhancement up to 53% was observed for nanofluids [2]. It was also concluded that the deposition of nanoparticle on the surface was responsible for the CHF enhancement. However, there is no experimental data of flow boiling CHF of pure fluid (i.e. water) with a nanoparticle coated surface. Some experimental data for pool boiling CHF

enhancement of pure fluid on pre-coated heaters was done by the author, Truong [3]. Furthermore, in most nanofluid studies, the nanoparticle deposition layer is usually complex and changes many surface properties at the same time. This makes characterization of the surface and identifying individual mechanism of CHF enhancement challenging. Better understanding of CHF and boiling heat transfer enhancement mechanisms will help develop design and management of safer operation of reactors and other heat transfer systems.

While CHF is the key safety limit in normal operation, quenching heat transfer plays an important role in LWR accident scenarios. In this case, the hot fuel rods need to be quenched by the incoming colder fluid. The heater surface conditions have been shown to affect quenching heat transfer rate as well but no separate surface effects have been previously studied. Therefore, it is necessary to perform a separate surface effect on CHF and quenching heat transfer to determine the most important parameters. In the rest of this chapter, a review of data in the literature for heat transfer of nanofluids and other enhanced surfaces are first summarized. Then, the objectives and outline of the thesis are described.

1.2 Literature Review

1.2.1 Nanofluid Boiling Heat Transfer

Nanofluids are engineered colloidal dispersion of nano-sized particles, or nanoparticles (<100 nm), in common fluids (water, refrigerants, ethanol). The nanoparticles materials range from metal, metal oxides to carbon of various forms (diamond, graphite). The term nanofluid was first proposed in the mid 1990s by Choi [4], who showed anomalous enhancement of thermal conductivity of nanofluids. Over the last decade, nanofluids researchers across the globe have spent significant effort to measure thermal conductivity of nanofluids, their convective heat transfer characteristics as well as their ability to enhance CHF. A recent review by Kakac et al. [5] showed that nanofluids have higher thermal conductivity and convective heat transfer compared to the base fluids. The authors noted that further work in the theoretical modeling and experimentation of nanofluids thermal conductivity is needed. A recent international benchmark of nanofluids thermal conductivity by Buongiorno et al. [6] indicated that there is no anomalous enhancement of thermal conductivity of nanofluids beyond the prediction of the effective medium theory. The largest enhancement observed was about 30% for Silica nanofluid with 31%

by volume (vol%) of nanoparticles. Also, this study found that nanofluid thermal conductivity increases with higher nanoparticle concentration and lower base fluid thermal conductivity in accordance with the effective medium theory.

While the potential for high thermal conductivity was the nanofluid property that initially attracted most attention, the ability of nanofluids to enhance CHF in both flow and pool boiling, as well as in quenching heat transfer, has been observed by many researchers. Table 1-1 lists some previous studies of nanofluids on both pool and flow boiling CHF. Overall, researchers have measured CHF enhancement of varying magnitudes with different nanoparticle materials and a wide range of concentrations. However, there is still no consensus on the boiling heat transfer coefficient of nanofluids as the data show that there can be enhancement, deterioration as well as no change in the boiling heat transfer coefficient.

Table 1-1: List of Previous Nanofluids Study on CHF in Pool and Flow Boiling

Reference	Nanofluid	Maximum CHF Enhancement	Heat Transfer Coefficient
You et al. [7]	Al_2O_3 in water	200%	Unchanged
Kim et al. [8]	TiO_2 in water	200%	Not reported
Vassallo et al [9]	SiO_2 in water	60%	Unchanged
Tu et al. [10]	Al_2O_3 in water	67%	Enhanced
Kim and Kim [11]	TiO_2 in water	50%	Not reported
Moreno et al. [12]	Al_2O_3, ZnO in water Al_2O_3 in ethylene glycol	200%	Unchanged
Bang and Chang [13]	Al_2O_3 in water	50%	Deteriorated
Milanova et al. [14]	SiO_2, CeO_2, Al_2O_3 in water	170%	Unchanged
Jackson et al. [15]	Au (3 nm) in water	175%	Deteriorated
Wen and Ding [16]	Al_2O_3 in water	40%	Enhanced
Kim et al. [17]	Al_2O_3, SiO_2, ZrO_2 in water	80%	Deteriorated
Kathiravan et al [18]	Copper nanofluid	50%	Deteriorated
Kwark et al.[19]	Al_2O_3	90%	Unchanged
Park et al. [20]	Graphene/Graphenes oxide	179%	NA
T.J. Kim et al.[21]*	Al_2O_3	70%	Unchanged
Kim et al. [22]*	Al_2O_3, ZnO and diamond	50%	Unchanged

*Flow boiling

Another common finding in most of these studies is the formation of a porous layer on the heater due to nanoparticle deposition during boiling. For example, nanoparticle depositions on heater surfaces are reported by Bang and Chang [13] and Kim et al. [17]. Also, Liu and Qui [23] reported a thin sorption layer on the heated surface when a nanofluid jet impinges on the surface. Kim et al. [22] measured subcooled flow boiling CHF of alumina, diamond and zinc oxide nanfluids and found nanoparticles deposited on the surface of the heater. The deposition of nanoparticles was found to change the morphology and properties (e.g., roughness, wettability) of the heater surface. Since the thermo-physical properties (surface tension, thermal conductivity, viscosity, evaporation heat, specific heat, density) of low volume concentration nanofluids are similar to those of pure water [3], these changes in surface morphology and properties are believed to be the main mechanisms for the CHF enhancement of nanofluids. In fact, a previous study in pool boiling [3] showed that nanoparticle deposited layer helped enhance pool boiling CHF even for stainless steel sandblasted surfaces, which already have higher CHF than smooth surfaces. However, no such work has been done in flow boiling. Therefore, it is necessary to verify that flow boiling CHF can be enhanced by modification of heater surface via boiling-induced deposition. In order to do this, a facility to coat test sections in flow boiling and to measure CHF of a pure fluid (e.g. water) using these test sections is needed.

1.2.2 Quenching Heat Transfer with Nanofluids

In the previous section, nanofluids have been shown to enhance CHF and sometimes also the heat transfer coefficient. While the data for quenching heat transfer on nanofluids are not as abundant as for nucleate boiling and CHF, there are several studies indicating similar effect of nanoparticles on quenching.

Park et al. [24] studied quenching of Alumina nanofluid of high concentration (5 to 20 vol%) using a heated copper sphere. They found that film boiling heat transfer of nanofluid was actually lower than that of water. However, for repeated quenching experiments in nanofluids, they found the nanoparticle fouled sphere had much better heat transfer compared to the clean surface. They proposed that nanoparticles deposited on the previously-quenched sphere prevented the formation of a stable vapor film on the sphere surface, thus bypassing the film boiling regime altogether.

Chun et al. [25] measured quenching rate of a Platinum wire in Si and SiC nanofluids and water. They found little difference between boiling curves of the three fluids while there was little change in CHF values. However, they found nanoparticle coated wires were quenched much faster compared to the quenching rate of a bare wire in water. The transition boiling period for the nanoparticle coated wire was very short compared to that of a bare wire. This again suggests that the nanoparticle coating layer seems to have much better effect than the nanofluids themselves.

K. Babu and Kumar [26] studied quenching heat transfer rate of a rodlet. They found that 0.50 w% carbon nanotube (CNT) nanofluid provided the highest peak heat flux and cooling rate. A higher concentration of CNT started to undermine the enhancement. Also, performing a quenching experiment while the nanofluid being agitated with a mechanical stirrer, they found that the agitated nanofluid had lower quenching heat transfer rate, which was unexpected. They suggested that agitation could cause loss of Brownian motion of CNTs and molecular layering at the liquid/CNT interface. These two factors helped enhance the heat transfer performance of nanofluids. However, the effect of Brownian motion on quenching heat transfer seems unlikely.

Other quenching studies with nanofluids include that of Jagannath and Prabhu [27] and Xue et al. [28]. Similar to previous ones, these studies found nanoparticles deposited on the surface during quenching and helped enhance the quenching heat transfer rate. However, none of these studies provided a thorough characterization of the nanoparticle coating layer to help explain the accelerated quenching results. Recent studies by Kim et al. [29,30] demonstrated that deposition of nanoparticles on a surface significantly increased the nominal LFP up to ~500°C under atmospheric, saturated and subcooled conditions, considerably accelerating the transient cooling of overheated objects. However, such a high LFP could not be explained by the traditional LFP models based on hydrodynamic instability of the vapor film, e.g. Berenson [31]'s and Henry [32]'s models. The deposited nanoparticle layer changed many surface parameters at the same time and made it hard to quantify the surface effect on quenching heat transfer. Therefore, there is a need to quantify the nano-particle coating layer better and/or to have a separate surface effect study on quenching heat transfer.

1.2.3 Nano-Micro Engineering Surfaces for Heat Transfer Enhancement

While nanofluid enhancing CHF has been of great interest only in the past decade and a half, techniques that can enhance CHF have been investigated by researchers for a much longer time. One such technique is coating the heated surface with a porous coating layer. Nanofluids effectively deposit a porous coating layer on the heated surface and change the surface properties to help enhance CHF.

Porosity, introduced by porous surface layers or structures, has been shown to affect CHF. Several studies in the literature have shown that porous coatings enhanced both heat transfer coefficient and CHF. Recently, Palm [33] gave a review of porous surfaces' heat transfer enhancement and how they have been applied commercially. He concluded that the boiling heat transfer performance of a porous surface depends on the number nucleation sites, the ability to allow pumping of liquid by capillary force into the porous structure, and the number of large pores for easy escape of vapor. He also suggested that the ability of the porous structure to sustain larger bubble growth was an important factor for enhancing heat transfer coefficient. Palm [33] concluded that evaporation of menisci at three-phase line and evaporation of thin film liquid, are the two main mechanisms that can be affected by the porous structure. How the porous coating enhances heat transfer coefficient is relatively well understood, especially for well-defined surfaces. However, data on porous coating CHF is scarce compared to that for heat transfer coefficient and the effect of porous coating on CHF is still not clear, particularly in the sub-micron length scale.

Chang and You [34] coated a copper block with DOA particles (diamond, omegabond epoxy and isopropyl) of various diameters (2-75 μm). They defined the coating as micro-porous if the coating thickness was less than superheated liquid layer thickness, δ_{99}, which was estimated to be approximately 100 μm. If the thickness was larger than that, then the coating was defined simply as porous. They found the CHF values for porous surfaces could be up to 100% higher than that of plain surface. However, the CHF enhancement observed did not agree with models proposed by Tehver [35] and Polehaev [36].

Hwang and Kaviany [37] coated a copper heater with copper particles (40 to 200 μm) and measured CHF enhancement up to 96% for the porous surface. They postulated that CHF enhancement was due to either the increase in the fraction of area that could be safely covered by the vapor or the decrease in the Rayleigh-Taylor instability wavelength. They also found that the porous surfaces had smaller superheat compared to the plain one.

Kim et al. [38] coated a copper block with aluminum particles of different sizes (3-4.5, 4.5-10, 8-12, 10-14, and 17-30 μm) using Aluminum Devcon Brushable Ceramic (ABM) coating technique. They found highest CHF enhancement for coating of 8-12 μm particles in both FC-72 and R-123 refrigerant. However, there was no trend between CHF enhancement and particle diameter. They also found boiling curves for coated surfaces shifted to the left of that of plain surface, which means these porous surfaces also enhanced the heat transfer coefficient.

Arik et al. [39] coated silicon chip heater with diamond particle of 8-12 μm diameter. The coating thickness was 50-75 μm. They found the porous coating surface enhanced CHF at pressure of 1, 2 and 3 atmospheres, with the highest CHF enhancement up to 100%. Also, the superheated temperature for the coated surface was lower than that of the plain one.

Ferjancic and Golobic [40] modified stainless steel ribbons by etching and sanding. They found the rough surfaces had higher CHF compared to the smooth one, but only by very little. However, they also found the roughened surface, if further treated by acid etching, gave higher CHF enhancement. While the surface roughness of the modified surfaces is higher than that of the plain one, the authors concluded that surface roughness was not enough to explain the enhancement in CHF observed. However, no model or explanation of such conclusion was provided.

Yang et al. [41] coated a spherical downward facing test section with Alumina porous layer. They found local CHF of water using coated surface was higher than that of the plain one at all angular positions. However, for the coated surface, the minimum CHF did not happen at the bottom of the sphere. Also, the Aluminum porous coating layer was found very durable.

Vemuri and Kim [42] coated an Aluminum surface with Alumina nanoparticle (50 to 250 nm) at thickness of 70 μm and found the porous surface had reduction of 30% in incipient superheat. The CHF value was not determined for this surface. This is one of a few studies that used nanoparticle coatings.

Using hot-powder compaction method, Min et al. [43] coated copper substrates with 2D and 3D modulated layer of 45 to 200 μm-diameter copper particles. Using pentane as the fluid, the CHF of the modulated surface was found to be higher than that of the plain surface by as much as 3.3 times for the 3D coating, and 2.0 times for the 2D coating. The CHF was found to depend mostly on the modulated wavelength (distance between two peaks in the regular coating array) rather than the porosity of the layer or the diameter of the micro particles.

Recently, Cora et al. [44] manufactured micro-scale modulated coating of copper particle of 100 μm diameter, and found both heat transfer coefficient and CHF enhancement for pentane up to 300%. The coating layer formed by low compaction pressure had the highest CHF enhancement. The coating thickness in this study was as high as 500 μm.

Similarly, Melendez and Reyes [45] conducted a pool boiling heat transfer study using binary mixture of water and ethanol on smooth and porous coated surface. The heater was a cylindrical tube. Iron wool and stainless steel wool were wrapped around the heater to create the porous structure. The highest heat transfer rate of 220 W/m^2K for heat flux of 165 kW/m^2 for a binary mixture on the surface was obtained. The heat transfer rate enhancement was due to an increase in capillary pressure in the porous structure, which reduced the bubble size and helped pump cold liquid towards the heater surface. No CHF value was reported.

Li et al. [46] fabricated a modulated conical porous structure of copper microparticles (25 μm) on a plain copper surface. The modulated porous structure was found to enhance boiling heat transfer and the enhancement was postulated due to the capillary force in the pores, which helps supply liquid to the heated surface. In addition, Li and Peterson [47] measured CHF and heat transfer coefficient of surface coated with uniform and modulated coating of copper particles (250 μm diameter) with coating thickness up to 1200 μm. While the uniform porous coating

helped enhance CHF compared to the plain surface, the authors found that the modulated porous coating provided the highest CHF and heat transfer coefficient enhancement. The CHF enhancement in the modulated porous coating was attributed to the separated liquid/vapor flow paths and increase in both horizontal and vertical replenishment of liquid inside the porous structure. The enhancement in heat transfer coefficient was due to the increase in surface area and the higher density of nucleation site density due to the porous structure. This study also found that thick porous led to better CHF enhancement compared to the thinner one.

Porous coatings enhance CHF. However, most of these porous coatings used micron-size particles and the coating is relatively thick (order of 10s of micrometer). This effectively changed surface parameters including surface roughness, wettability and porosity, all at the same time. Therefore, the mechanism for how CHF is enhanced by a porous coating layer is still not well understood. Therefore, it is necessary to perform a study on separate effects of surface parameters on CHF.

1.3 Thesis Objectives and Motivations

The first objective of this work is to prove that the nanoparticle deposited layer on heaters is responsible for CHF enhancement in subcooled flow boiling. Many nanofluid researchers have suggested that the deposited layer of nanoparticle on the heater surface helps enhance CHF; however, no work has been done to provide a firm conclusion. In pool boiling, this has been confirmed by previous work of the author [3]. This work will focus on flow boiling and provide the most conclusive evidence that nanofluid enhanced CHF by nanoparticle deposition, not by changing properties of the fluid. Furthermore, it can also be shown that boiling-driven deposition is a possible technique to coat heater with layer of nanoparticle. This technique will provide insights for in-situ surface treatment using nanofluids.

The second objective is to study the parametric effect of surface parameters (roughness, wettability and porosity) on quenching heat transfer, focusing on quenching Leidenfrost point (LFP). In this section of the thesis, one by one, the main surface parameters including roughness, wettability and porosity are changed and then their effects on quenching LFP are studied. This will provide insights in understanding how nanoparticle coating layer in quenching experiments provide better quenching rate. The data here will be useful for the development of mechanistic models of quenching heat transfer phenomena in reactors.

The final objective of this work is to perform a separate surface effect study on pool boiling CHF. The results will help identify which surface parameter among wettability, roughness and porosity has the strongest effect on CHF. Analysis of data from this study and those from the literature will help understand better the mechanism of how porous coating layer enhances CHF. Comparison of the current existing models/correlations with the data will allow identification of areas that would require more investigation in both experimental and theoretical studies to provide a thorough understanding of surface effect on CHF. Ultimately, this will help for optimization of surface for CHF enhancement in nuclear reactors and other industrial applications. Similar to the quenching study, the data will be useful for better CHF mechanistic model development.

1.4 Thesis Outline

The rest of this thesis consists of five chapters. In Chapter 2, subcooled flow boiling CHF experimental data for nanoparticle coated test sections are presented. The results from these experiments will confirm the claim that nanoparticle deposited layer on surface is responsible for nanofluid flow boiling CHF enhancement.

In Chapter 3, single droplet quenching Leidenfrost point experiments with controlled surface parameters are presented. The experimental setup, procedure and data will be discussed. The analysis of the data will help explain which parameter has the strongest effect on this boiling phenomenon.

Chapter 4 is a study of surface effect on pool boiling CHF based on the results in Chapter 3. The selection process for the fluid and experimental setup are discussed first. Subsequently, the experimental CHF data for surface with only change in roughness or porosity are presented. The fluid in this study will be a refrigerant. The results help identify which surface properties are most important for CHF.

Chapter 5 begins with a review of existing CHF models. Then, an analysis of how surface roughness and porosity affect CHF will be discussed. This chapter ends with an analysis of the CHF data in this study and in the literature in order to illuminate how each surface parameter affects CHF.

The final chapter provides a summary of the findings of this study and recommendations for future work.

2 Pre-Coated Subcooled Flow Boiling CHF

2.1 Introduction to Flow Boiling CHF of Nanofluids

As discussed in Chapter 1, the data for pool boiling CHF of nanofluids seem to be abundant. However, there are limited data for flow CHF of nanofluids. One of the first data was obtained by Kim et al. [2], who measured CHF of Alumina , Zinc Oxide and Diamond nanofluid and found CHF enhancement up to 53%. There are several other studies measuring the flow boiling CHF of nanofluids, as discussed earlier in Chapter 1. One reason for fewer data in flow boiling than pool boiling of nanofluids is that the flow boiling experiment encounters more challenges, ranging from cost, setting up, procedure, safety to post test surface analyses. Nevertheless, flow boiling CHF is more relevant to reactor applications, from normal operations to accident conditions. Therefore, it is necessary to increase the nanofluid flow boiling CHF data to evaluate its potential for nuclear reactor applications.

This chapter describes the experimental study of flow boiling CHF of water using nanoparticle pre-coated test sections. This study will confirm that the nanofluid CHF enhancement in flow boiling is due to the nanoparticle deposited layer, not the particles in the fluids. The first part will describe the experimental setup and procedure. Then, the results and test section surface analyses will follow. The last part will summarize the key findings.

2.2 Flow CHF Experimental Facilities and Procedure

2.2.1 Experimental Loops

Two flow boiling loops were used to prepare the nanoparticle pre-coated test sections and measure the values of their subcooled flow boiling CHF. In this study, the test section is a stainless steel 316 (SS316) cylindrical tube of 6.35 mm (0.25") diameter, 0.4064 mm (0.016") thick and 100 mm heated length. The first loop, denoted as coating loop, was used to coat the test sections via flow boiling induced deposition. The second loop, denoted as two-phase loop, was used to measure subcooled flow boiling CHF of water using the pre-coated test sections. The test section was transferrable between the two loops. The reason the two loops approach was used

was to avoid putting nanofluids inside the two-phase loop, as flushing nanofluids out of that loop can take a long time and can still leave nanoparticle residues inside the loop.

2.2.1.1 Pre-coating Loop

The schematic of the pre-coating loop is shown in Figure 2-1. The loop is constructed of predominantly 0.25" OD stainless steel 316 tubes. This loop includes a gear pump (Model PQ-12 DC) to circulate the fluid, a flow meter (Omega FTB9504-251906) to measure the mass flow rate, and an accumulator for liquid inventory control. The flow direction is vertically upward through the heated test section. A copper coil heat exchanger is located inside the accumulator to remove heat from the loop. K-type thermocouples were used to measure inlet, outlet and outer wall temperature of the test section.

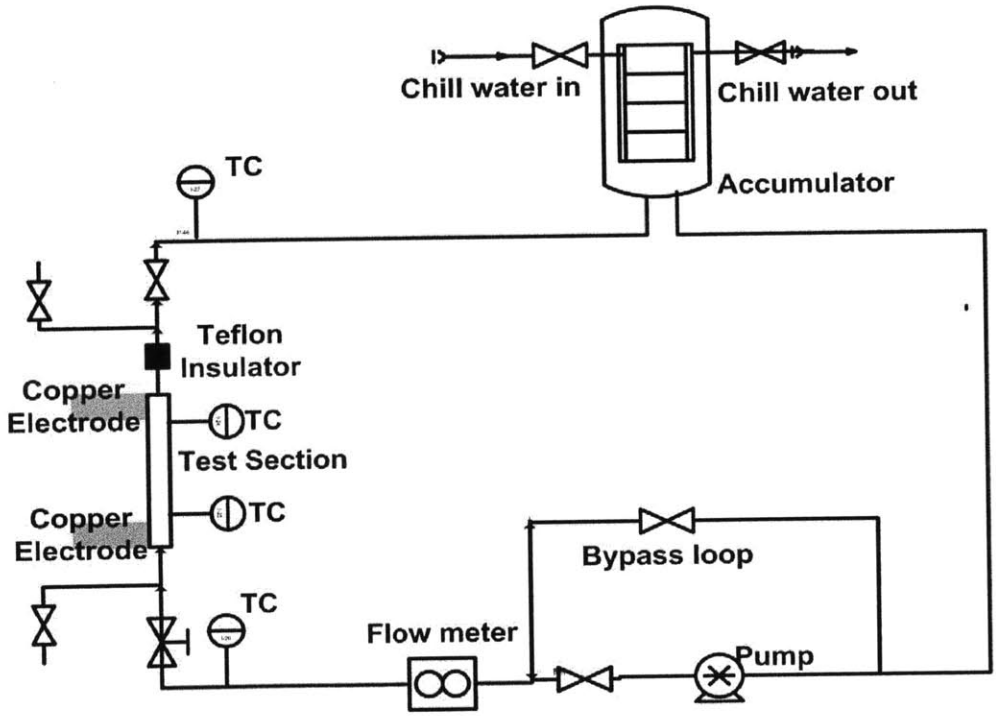

Figure 2-1: Schematic of the Pre-coating Loop

The test section for flow boiling experiments is a stainless steel 316 tube (purchased from All Stainless Inc., Shipment # 302850, ASME SA213-014 HEAT No 1471/0654 BA) with OD of 6.35 mm (0.25") and wall thickness of 0.41 mm (0.016"). The test section assembly is shown in Figure 2-2. The Teflon at the top of the test section is used to put an electrical isolation in the

loop. Heat is supplied to the test section via resistive heating using the two copper electrodes connected to a DC power supply (500A by 20 V) .

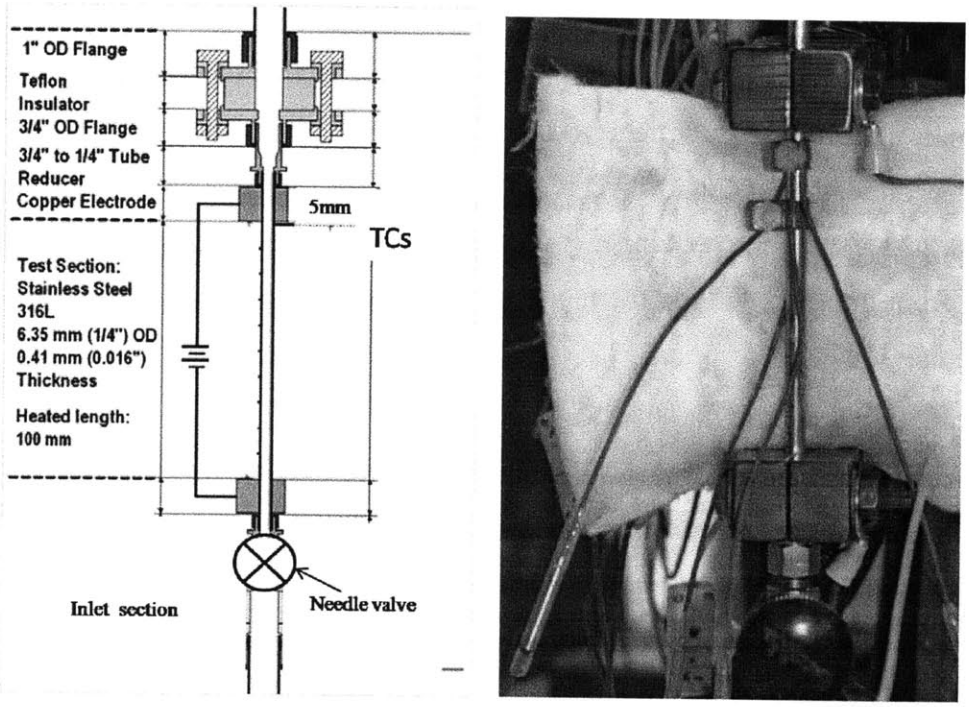

Figure 2-2: Schematic Test Section Assembly (left), Photo (right)

Using the coating loop, the test sections was coated with nanoparticle via nanofluid flow boiling induced deposition. Alumina nanofluid (Al_2O_3) 20% by weight (w%) was purchased from Nyacol. The dilutions of the nanofluid was done using the relation reported by Kim [2] in equation (2-1).

$$f = n\frac{\frac{1-y}{y} - \frac{1-x}{x}\cdot\frac{\rho_p}{\rho_w}}{1+\frac{1-x}{x}\cdot\frac{\rho_p}{\rho_w}} \qquad (2\text{-}1)$$

Here, x is the weight percent of the original nanofluid from the vendor, y is the volumetric fraction of the desired fluid, n is the amount of x w% nanofluid, f is the amount of water required for dilution, and ρ_p and ρ_w are the densities of the nanoparticle and water, respectively. The density of Alumina nanoparticles is assumed to be that of bulk Alumina (3.90 g/ml). Based

on equation (2-1), in order to make 100 ml of 0.1vol% Alumina, 96.39 ml of deionized water and 3.61 ml of 20 w% Alumina would be needed.

Besides using Alumina nanofluid to coat the test sections, Alumina+PAH ((Aldrich Poly(allylamine) hydrochloride) solution was also used. Polyallylamine hydrochloride (PAH) is a polymer, which has been used in layer-by-layer (LBL) deposition method to provide a durable super-hydrophilic coating layer of SiO_2 or TiO_2 nanoparticles [48]. Forrest et al. [49] used LBL technique to coat wire heater with thin film of PAH/nanoparticle and showed that such coating enhanced both heat transfer coefficient and CHF of water up to 100% in pool boiling. However, the layer-by-layer deposition technique requires an extensive chemical process and imposes limits on the size of the heater. This study intends to study if boiling induced deposition is a potential technique to deposit nanoparticle/PAH onto SS316 test section, and how that would affect CHF.

Alumina+PAH solution was prepared by first dissolving PAH in deionized water using a magnetic stirrer. This PAH solution was then used to dilute the concentrated Alumina nanofluids to make Alumina nanofluids with known amount of PAH (in quantity of 100 or 1000 ppm). The fluids were then used immediately in the coating loop right after they were prepared to pre-coat test sections. After the coating procedure, these fluids were discarded. Stability of the mixture was determined through visual observation for sedimentation right after preparation or after the coating procedure. All the solutions used in this study appeared stable after the coating procedure. The thermo physical properties of the different solutions were not measured in this study because the nanofluid solutions were only used for coating purpose.

The test sections were coated using the following procedure. First, approximately 3500 ml of nanofluid was added to the accumulator. The fluid was then circulated around the loop using the gear pump for about 10 minutes. The flow rate was controlled using a needle valve in the bypass loop. Once the flow rate ($G = 670$ kg/m^{2}s) was established, a desired heat flux was applied (by increasing in small steps with approximately one-minute wait between each step to a pre-determined value) to the test section via the copper electrodes using a DC power supply. The bulk fluid temperature was monitored and controlled (by adjusting chilled water flow rate) so

that the inlet temperature stayed relatively constant once it reached equilibrium. The coating process was done for 0.5 – 2.0 hours after equilibrium was established to allow particle deposition.

Table 2-1 lists the coating parameters for various test sections in this study. Each row in the table represents a batch of test sections. For each batch, usually four test sections were coated using the same reservoir of nanofluid. A new reservoir of nanofluid was used for a new batch of test sections. In addition, it must be noted here that for test section C1Al to C18Al, the pre-coated length was 100 mm; however, from there on, the pre-coated length was 110 mm (test section C19Al to C43Al). The heated length, when the test section is transferred to the two-phase loop, is still 100 mm, starting from the bottom electrode. The reason for such change is to ensure the coated length will cover the entire heated section in CHF tests.

For a typical coating process, the temperature of the fluid and the outer wall temperature stayed relatively constant (usually within ±2 °C) once equilibrium was established. An example of temperature as a function of time during the coating process is shown in Figure 2-3, while Figure 2-4 shows the heat flux profile of the same experiment. Also, the outer wall temperature was around 140 °C ensuring that there was boiling, which could also be detected by the rattling noise from bubbles collapsing.

Table 2-1: Coating Parameters for Flow Boiling Test Sections

Batch	Test section name	Coating Fluid	Coating Heat Flux (MW/m^2)	Coating time (hours)
1	C1Al, C2Al, C3Al	1.0 vol% Alumina	0.5	0.5
2	C4Al, C5Al, C6Al	1.0 vol% Alumina	1.0	0.75
3	C7Al, C8Al , C9Al, C10	0.1 vol% Alumina	1.0	1.5
4	C11Al, C12Al, C13AL, C14Al	1.0 vol% Alumina	1.0	2.0
5	C15Al, C16Al, C17Al, C18Al	1.0 vol% Alumina	1.0	2.0
6	C19Al, C20Al, C21Al, C22Al	1.0 vol% Alumina	1.5	2.0
7	C23Al, C24Al, C25Al, C26Al	1.0 vol% Alumina	1.5	2.0
8	C27AlPAH, C28AlPAH, C29AlPAH, C30AlPAH	1.0 vol% Alumina with 1000 ppm PAH	1.5	2.0
9	C31AlPAH, C32AlPAH, C33AlPAH	1.0 vol% Alumina with 1000 ppm PAH	1.5	2.0
10	C34AlPAH, C35AlPAH, C36AlPAH, C37AlPAH	1.0 vol% Alumina with 100 ppm PAH	1.5	2.0
11	C38PAH, C39PAH, C40PAH	Water with 1000 ppm PAH	1.5	2.0
12	C41Al, C42Al, C43Al	1.0 vol% Alumina	1.5	4.0

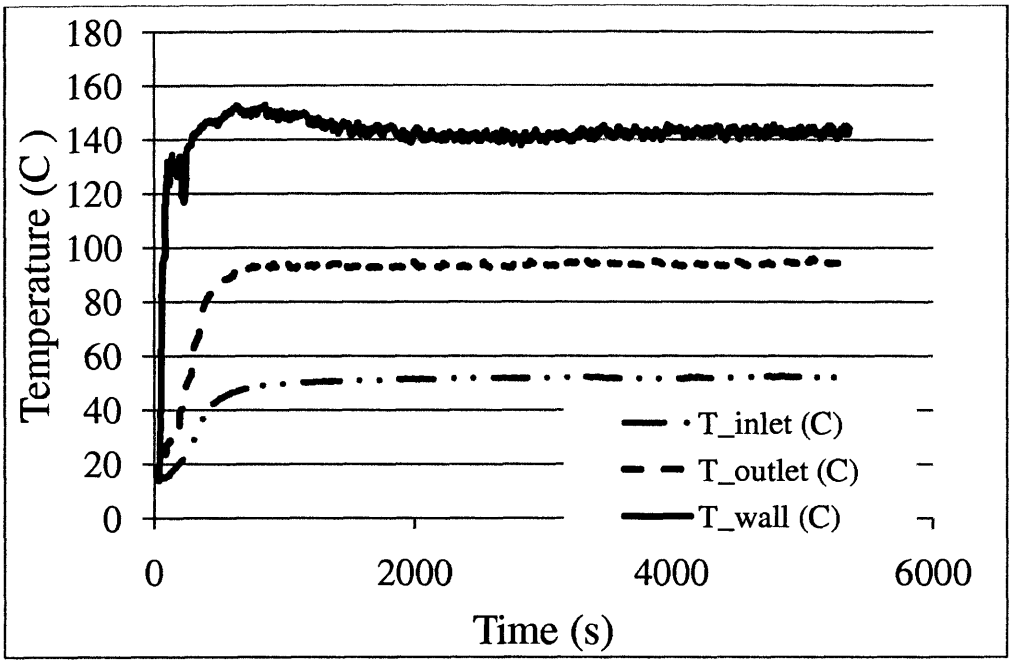

Figure 2-3: Representative Temperature Profiles during a Coating Process

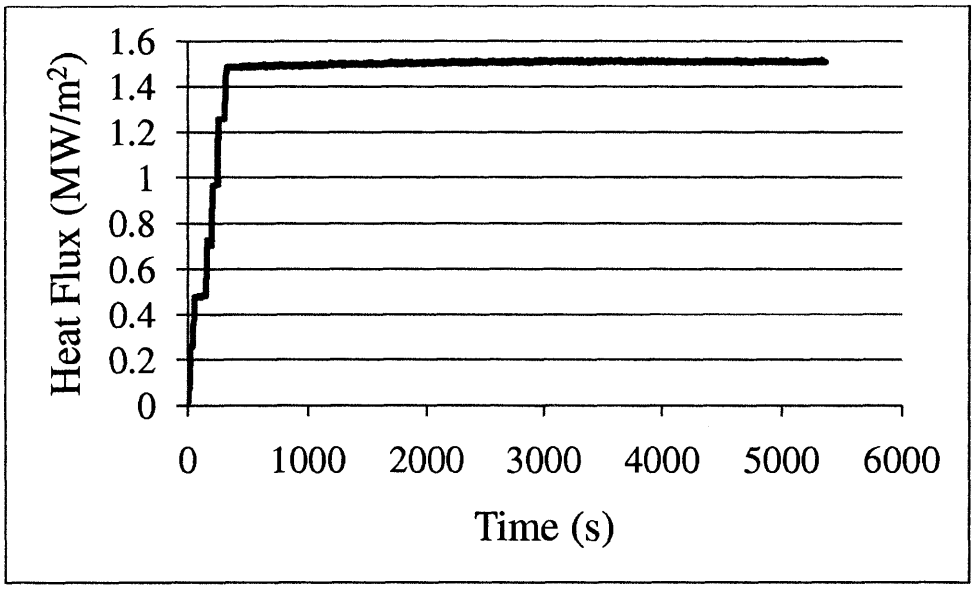

Figure 2-4: Representative Heat Flux Profile during a Coating Process

2.2.1.2 Two-Phase CHF Loop

Flow boiling CHF experiments were performed in a flow boiling loop, denoted as two-phase CHF loop here. The schematic diagram is shown in Figure 2-5. This loop was built and used by Kim et. al. [2] to measure CHF of nanofluids. Detailed descriptions of all components and loop

calibrations can be found in that reference. The loop contained a pre-heater, a heat exchanger, a pump and an accumulator. The pre-heater was used to control fluid inlet temperature during degassing. The accumulator was used to adjust the system pressure but all experiments were run at atmospheric pressure. The loop was constructed mostly with 25.4 mm OD (1") stainless steel tubing. The stainless steel 316 test section (again, purchased from All Stainless Steel Inc., SMLS ¼"x0.016", ASTM A213-014/A269-02, ASME SA213-014, HEAT No 1471/0654 BA), however, had OD of only 6.35 mm (0.25") with wall thickness of 0.41mm (0.016"). The heated length was 100 mm. The test section here was identical to that in the coating loop because they must fit in both loops.

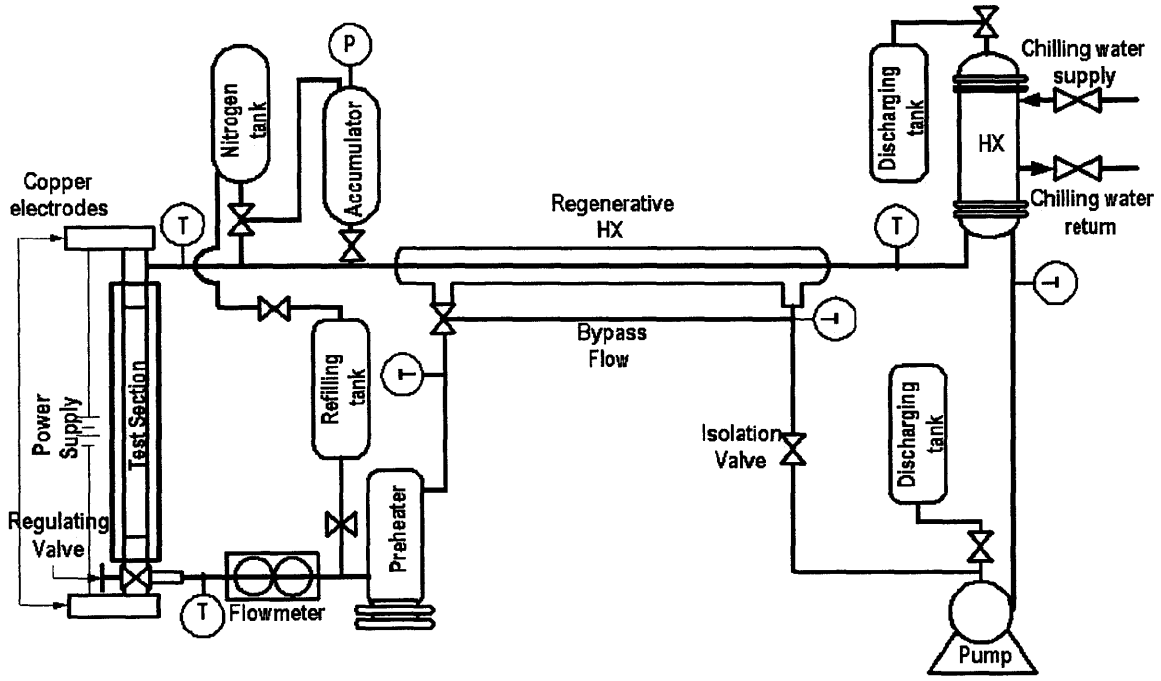

Figure 2-5: Flow Boiling Two-Phase CHF Loop – Schematic (adopted from Kim [2])

Power was supplied to the test section via copper electrodes, which were connected to two identical DC power supplies operating in parallel. The voltage and the current supplied to the test section were measured using calibrated voltmeter and inductive ammeter with uncertainty less than 2%. The heat flux on the inner tube surface is calculated as:

$$q'' = \frac{IV}{\pi D_i L} \tag{2-2}$$

where V and I are the voltage and current, respectively, and D_i and L are the inner diameter and the heated length of the test section, respectively. Assuming all variables are distributed normally and are independent from each other, the uncertainty in the measurement of the heat flux is determined as

$$\frac{U_{q''}}{q''} = \sqrt{\left(\frac{U_I}{I}\right)^2 + \left(\frac{U_V}{V}\right)^2 + \left(\frac{U_{D_i}}{D_i}\right)^2 + \left(\frac{U_L}{L}\right)^2 + \left(\frac{U_{F_{ax}}}{F_{ax}}\right)^2} \quad (2\text{-}3)$$

where U is uncertainty; q'', I, V, D_i, L and F_{ax} are the heat flux, current, voltage, inner diameter of the test section, and local axial peaking, respectively. Axial peaking is defined as the difference between the highest local axial heat flux compared to the average heat flux of the test section. This was measured by having 10 equivalent voltage taps along the test section and determined the heat flux in each segment at several heat flux levels based on the voltage drop across each axial segment [2]. With the uncertainty of I, V, D_i, L and F_{ax} of 1.5%, 1.5%, 0.1%, 3% and 5% [2], respectively, the uncertainty of the heat flux was determined to be less than $<\pm 6.3\%$. K-type thermocouples were used to measure the inlet and outlet temperature of the test section. Several K-type thermocouples were clamped onto the outer surface of the tubing at different azimuthally locations right below the top copper electrodes to measure the outer wall temperature. The heat loss (defined as the normalized difference between the electric power and the fluid thermal power) was estimated to be less than 10% at low heat flux ($q'' < 1.0$ MW/m^2) and less than 5% at high heat flux ($q'' < 4.5$ MW/m^2). The pressure could be controlled using the accumulator but all experiments were performed at atmospheric pressure. The accumulator was also used to purge non-condensable gas at the beginning of each run. The centrifugal pump was used to control mass flow rate in the loop, which was measured with a flow meter of $<\pm 5\%$ uncertainty.

2.2.2 Experimental Procedure

Bare test sections (un-coated) were first used to measure CHF of water to verify the operation of the flow boiling loop. The bare test section was cleaned with acetone and then rinsed with DI water to remove contaminants and was then dried in a 120 °C oven before it was attached to the loop. The flow boiling loop was then filled with deionized water. Using the pre-heater, the entire loop was heated up to 60 °C and the coolant was circulated for 1 hour to remove non-condensable gases. The non-condensable gases were purged by periodic opening drain valves at

the heat exchanger and the pre-heater. Further degassing was done by applying approximately 2.8 – 3.0 MW/m^2 heat flux to the tube for 30 minutes while the fluid temperature was still at 60°C with periodic opening of drain valves to release gases. After degassing was completed, the loop temperature was lowered to the chilled water temperature. The desired mass flow rate (1500 or 2500 kg/m^{2}s) was then established using the needle valve at the bottom of the test section. Power was supplied to the test section in constant current steps. A several-minute wait time allowed steady state to be achieved between each step. Flow rate, test-section current and voltage, inlet and outlet temperature and wall temperatures were recorded and monitored at each step simultaneously via the DAC system. The power was increased in constant current mode continued until CHF occurred, which was indicated by a temperature excursion and rupture of test section right below the top copper electrode. Figure 2-6 shows a typical heat flux history of a CHF experiment. The spike in heat flux at CHF was due to increase in resistance of the test section , which was caused by a spike in the temperature. Figure 2-7 shows pictures of quarters of test sections that were not used in CHF and those that were burnt out in CHF experiments. The discolored portion was due to burnout at the test section outlet.

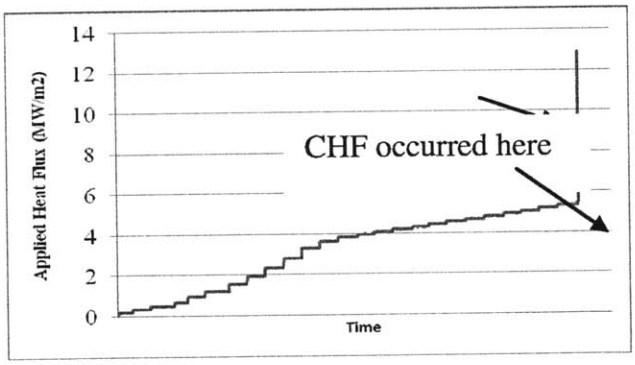

Figure 2-6: Typical Heat Flux Profile in a CHF Experiment

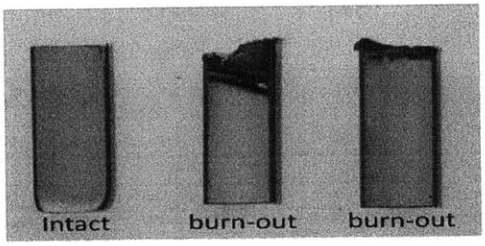

Figure 2-7: Picture of Burn-out and Intact Test Sections

The procedure to measure water CHF using a pre-coated test sections was similar to that of the bare tube except during the degassing phase. A bare tube was used in the first hour of degassing

at 60 °C. This bare test section was then replaced with a pre-coated test section. Isolation valves below and above test section in CHF loop were used to prevent air from entering into the loop during the change-out. This was done to minimize the possibility of the nanoparticles deposited on the coated test section being removed during the initial degassing process. Second degassing was done by applying approximately 2.8-3.0 MW/m^2 to the coated test section while the inlet water temperature was kept at 60 °C.

2.2.3 Flow Boiling Performance of Alumina and Alumina + PAH Coatings

2.2.3.1 CHF and Heat Transfer Coefficient for Bare Experiments

First, the CHF of deionized water was measured using bare (un-treated/uncoated) test sections to verify that the flow boiling loop operate as expected. Several tests were done under this condition. The results are shown in Table 2-2. Here, *xe* is the outlet equilibrium quality, and LUT is the value from the 1995 CHF look up table [50][1]. The CHF ratio is that between the measured value and the one from LUT 1995 at the same outlet equilibrium quality. The values for CHF measured here are within 5% of that predicted by the LUT 1995, which verified the operation of the flow loop. Notice also that the waiting time between each heat flux step in **Bare-1** and **Bare-2** experiments was 6 minutes (following experiences of Kim [2]) while it was 3 minutes for the other experiments. This was done to see if there was an effect on CHF due to the waiting time. There appeared to be no difference between 6-minute and 3-minute wait. From there on, all CHF experiments were done with 3-minute wait between each heat flux step.

Table 2-2: CHF Values of Water Measured Using Bare Test Sections (No Coating)

Experiment	Mass flux (kg/m^{2}s)	Step time (minute)	Measured CHF (MW/m^2)	*xe*	LUT (MW/m^2)	Measured / LUT
Bare-1	2500	6	5.35	-0.071	5.34	1.00
Bare-2	2500	6	5.41	-0.073	5.36	1.01
Bare-3	2500	3	5.40	-0.072	5.34	1.01
Bare-4	2500	3	5.51	-0.072	5.35	1.03
Bare-5	2500	3	5.32	-0.079	5.58	0.95

[1]The reason the 2006 LUT was not used here was that there was big discrepancies (up to 1.2 MW/m^2) between the 1995 and 2006 LUT at the outlet quality range for the bare test sections. The authors of the LUT were contacted several times via e-mail for explanation of such discrepancies but they never replied. The bare data here agreed with 1995 LUT tables and those data measured by Kim [2]. Therefore, it was decided that 1995 LUT will be used as the reference in this study.

The heat transfer coefficient at the test section outlet was calculated from the wall temperatures measured using K-type TCs distributed axially. The inner wall temperature, T_{wi} , was calculated using the radial heat conduction equation in the tube wall with adiabatic boundary conditions.

$$T_{wi} = T_{w,out} - q'' \frac{D_i}{2k_h}\left[\frac{D_o^2}{D_i^2 - D_o^2}\ln\frac{D_i}{D_o} - \frac{1}{2}\right] \tag{2-4}$$

D_o and D_i are the outer and inner diameters, respectively. $T_{w,out}$ is the outer wall temperature (measured by TCs). k_h is the thermal conductivity of stainless steel test section, whose temperature dependence is given as:

$$k_h = 13.00857 + 0.01687T_{w,out} - 2.08333\times10^{-6}T_{w,out}^2 \tag{2-5}$$

which represents a best fit of the SS316 thermal conductivity values reported in the ASME code [51]. The effective heat transfer coefficient, h, can be calculated using the measured heat flux, the bulk temperature and the inner wall temperature as:

$$h = \frac{q''}{T_{w,i} - T_b} \tag{2-6}$$

where T_b is the bulk temperature at the outlet of the test section. The uncertainty in the heat transfer coefficient can be determined as

$$\frac{U_h}{h} = \sqrt{\left(\frac{U_{q''}}{q''}\right)^2 + \left(\frac{U_{\Delta T}}{\Delta T}\right)^2} \tag{2-7}$$

With uncertainty of heat flux up to 6.3%, minimum ΔT of approximately 30°C and maximum uncertainty in ΔT of 2.2 °C, the uncertainty in heat transfer coefficient is less than ±9.6%. Figure 2-8 shows representative inner wall and bulk temperature. T_{chen} is the wall temperature calculated from the measured heat flux and the outlet bulk temperature using the well known traditional Chen correlation [52].

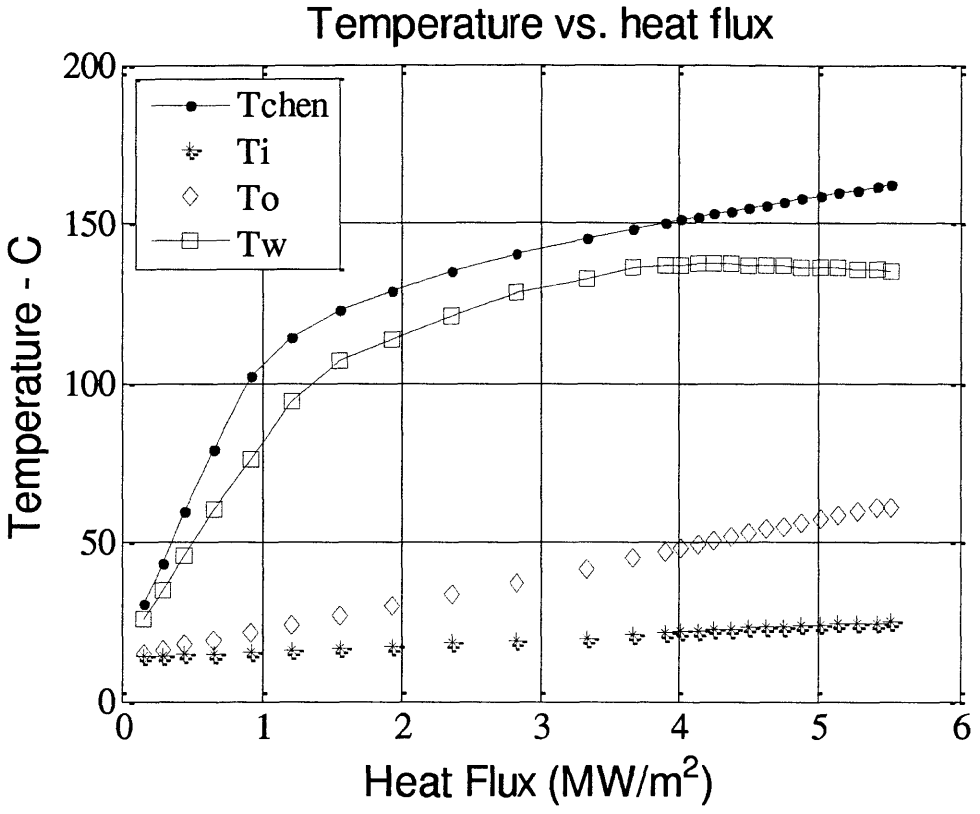

Figure 2-8 Temperature vs. Heat Flux for a Typical CHF Experiment with a Bare Test section

The Chen correlation for flow boiling, applicable for subcooled conditions, has the following relationship

$$q'' = h_{NB}(T_w - T_{sat}) + h_c(T_w - T_{bulk}) \tag{2-8}$$

where h_{NB} and h_c is the nucleate boiling and convective heat transfer coefficient, respectively. T_w, T_{sat} and T_{bulk} are the inner wall temperature, the water saturation temperature and the bulk temperature at the outlet of the test section, respectively. The nucleate boiling heat transfer coefficient, h_{NB} is calculated as

$$h_{NB} = 0.00122\left[\frac{k_f^{0.79} c_{p,f}^{0.45} \rho_f^{0.49}}{\sigma^{0.5} \mu_f^{0.29} h_{fg}^{0.24} \rho_g^{0.24}}\right] \times (T_w - T_{sat})^{0.24} [P_{sat}(T_w) - P]^{0.75} S \tag{2-9}$$

where $k_f, \mu_f, \rho_f, \rho_g, c_{p,f}$ and σ are respectively the thermal conductivity, viscosity, liquid and vapor density, specific heat, and surface tension of water at saturation. $P = 1\text{x}10^5$ Pa is the

operating pressure and P_{sat} (T_w) is the pressure at the wall temperature. S is the nucleate boiling suppression factor, which is defined as

$$S = \frac{1}{1+2.53\times10^{-6}\left(\frac{G(1-X)D_i}{\mu_l}\right)^{1.17}} \tag{2-10}$$

where μ_l is the liquid viscosity, G is the mass flux, X is the flow quality (=0) at subcooled condition. The convective heat transfer coefficient, h_c, is calculated as

$$h_c = \left(\frac{k_l}{D_i}\right)0.023\left(\frac{G(1-X)D_i}{\mu_l}\right)^{0.8}\left(\frac{\mu_l c_{p,l}}{k_l}\right)^{0.4} \tag{2-11}$$

where k_l, μ_l and $c_{p,f}$ are the thermal conductivity, viscosity and specific heat of water at the test section outlet bulk temperature. Using iterations in Matlab, the wall temperature was calculated. Subsequently, the heat transfer coefficient was calculated according to Eq. (2-6). Figure 2-9 shows the heat transfer coefficient (measured and predicted by Chen model) as a function of applied heat flux for all the bare test section experiments. The measured heat transfer coefficients for the all the experiments have similar trend and are within typical measurement uncertainty of ±10%. The heat transfer coefficients predicted by the Chen correlation are lower than the measured values, especially at higher heat flux. The results here agree with those measured by Kim [2], who used the same loop.

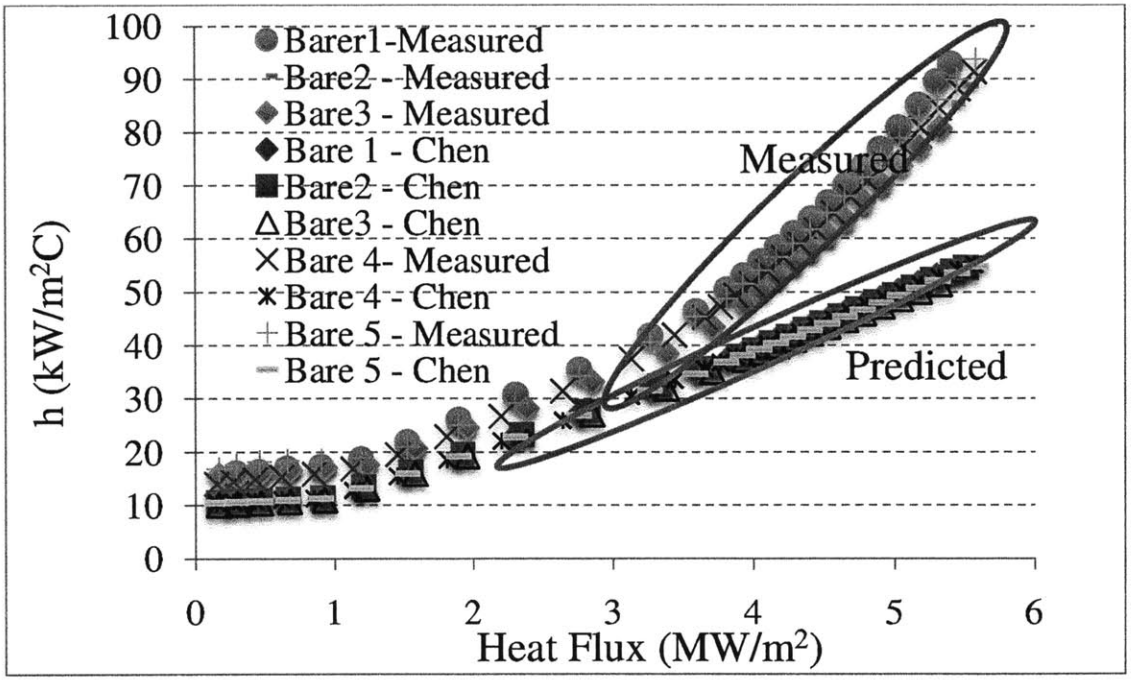

Figure 2-9: Heat Transfer Coefficient as a Function of Heat Flux for Bare Test Sections

2.2.3.2 CHF and Heat Transfer Coefficient for Coated Test Sections

2.2.3.2.1 CHF Results

With the CHF and heat transfer coefficient of water measured using bare test sections satisfactorily, the coated test sections were then used to see if they could enhance CHF and/or heat transfer coefficient of water. The water CHF results with nanoparticle pre-coated test sections are summarized in Table 2-3, Table 2-4 and Table 2-5. All the CHF experiments were done at 2500 kg/m^{2}s mass flux, except for test section C23Al to C25Al experiments, which were performed at a lower mass flux of 1500 kg/m^{2}s.

From Table 2-3 to Table 2-5, a batch number (same as in coating Table 2-1) represents the test sections that were coated using the same coating parameters and the same nanofluids. Usually, only two to three CHF experiments were performed for each batch. If two experiments from the same batch gave CHF values within 10% of each other, then a third experiment would not be run. The test sections that were not used to measure CHF are not listed here. No CHF experiment was done for batch number 9 because these test sections were only used to measure heat transfer coefficient at 1500 kg/m^{2}s and 2500 kg/m^{2}s up to heat flux of approximately 4MW/m^2. Results

for batch number 5 and 12 are not included here because there was problem with the coating. However, they are listed in the appendix and an explanation of the problem with the coating is also included. Moreover, test sections from C1Al to C6Al (batch 1 and 2) were used for SEM characterization of nanoparticle coating, and were not used in CHF tests. They were cut after the coating process for surface characterization.

Table 2-3: Water CHF with Alumina nanoparticle Pre-coated Test Sections at G = 2500 kg/m^{2}s

Batch	Experiment	Measured CHF (MW/m^2)	Outlet Quality (xe)	LUT	Meas./LUT Ratio
3	C7Al	6.20	-0.063	5.23	1.19
	C8Al	6.48	-0.059	5.19	1.25
	C9Al	6.51	-0.058	5.17	1.26
4	C11Al	7.15	-0.043	4.93	1.45
	C13Al	6.14	-0.059	5.19	1.18
	C14Al	6.27	-0.059	5.19	1.21
6	C19Al	6.88	-0.051	5.09	1.35
	C20Al	7.10	-0.053	5.11	1.39
	C21Al	6.88	-0.056	5.15	1.34

In Table 2-3, batch 3 has an average 23% CHF enhancement relative to the LUT value at the same outlet equilibrium quality and all three tests are close to each other. Batch 4 shows CHF enhancement up to 45% but two of the three tests have much lower enhancement, only around 20%. CHF enhancement of 36% on average was observed for batch 6. While this enhancement was not as high as that reported by Kim [2], who measured CHF of Alumina nanofluids using bare test sections, the results are still encouraging. A comparison of data in Table 2-3 and those by Kim [1] at G=2500kg/m^{2}s are shown in Figure 2-10.

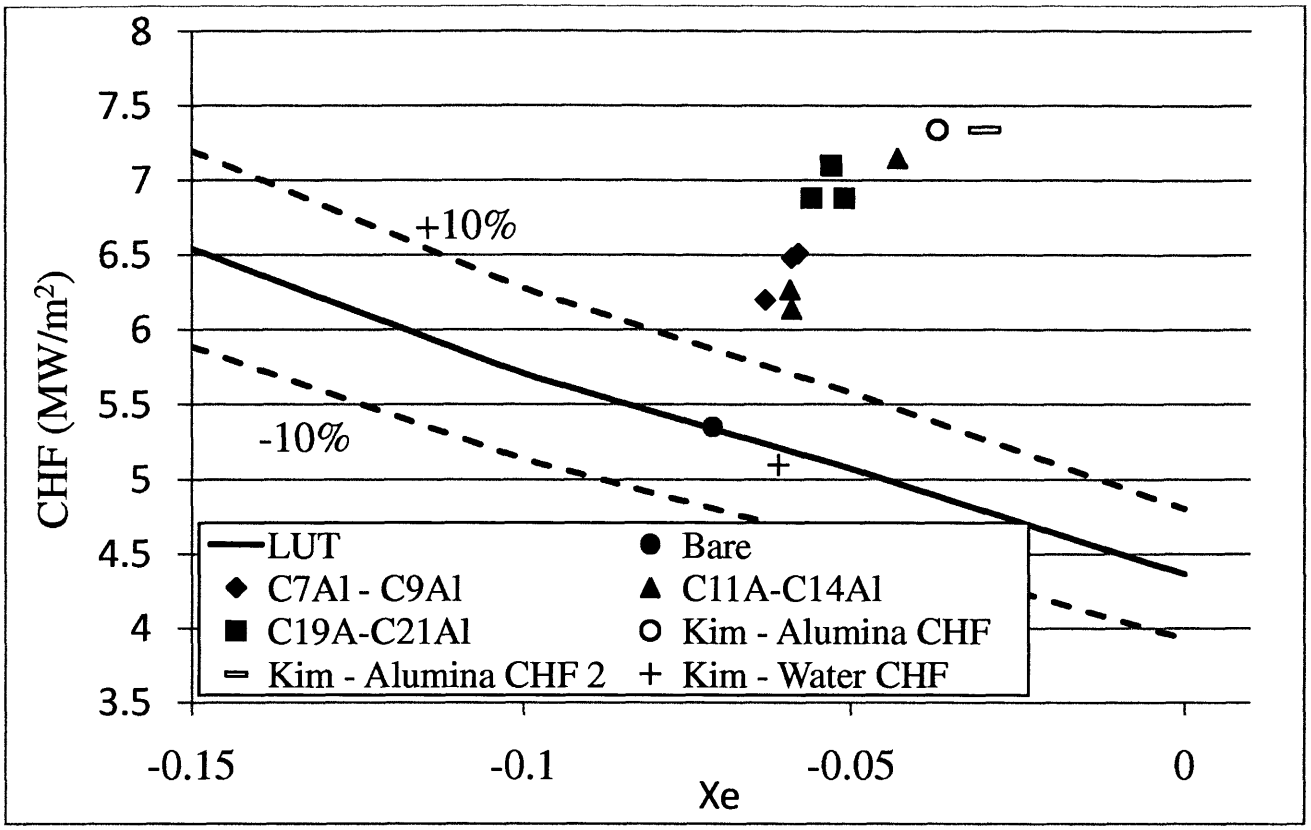

Figure 2-10: Comparison of Current Data to those of Kim [2] and Look Up Table Values [50].

However, at 1500 kg/m^{2}s mass flux, no CHF enhancement was observed for test section in batch 7, which was coated under the same conditions as those in batch 6. The results are shown in Table 2-4. These agree with the results reported by Kim [2], who observed no CHF enhancement of Alumina nanofluids at mass flux 1500 kg/m^{2}s. As of now, the effect of mass flux on CHF on nanoparticle coated test sections is still not clear.

Table 2-4: Water CHF with Alumina nanoparticle Pre-coated Test Sections at G = 1500 kg/m^{2}s

Batch	Experiment	Measured CHF (MW/m^2)	Outlet Quality (xe)	LUT	Meas./LUT Ratio
7	C23A1	5.01	-0.043	4.96	1.01
	C24A1	5.11	-0.042	4.95	1.03

As shown in Table 2-5, For test sections in batch 8, 10 and 11, which were coated using Alumina/PAH solutions, no CHF enhancement was observed regardless of the concentration of the PAH was used. The presence of PAH in the Alumina nanofluid appeared to prevent coating of Alumina nanoparticles such that no CHF enhancement could be observed for the coating layer having both PAH and Alumina nanoparticles.

Table 2-5: Water CHF with PAH/Alumina Particle Pre-coated Test Sections at G = 2500 kg/m^{2}s

Batch	Experiment	Measured CHF (MW/m^2)	Outlet Quality (xe)	LUT	Meas./LUT Ratio
8	C28AlPAH	5.86	-0.072	5.34	1.10
	C29AlPAH	5.47	-0.075	5.39	1.01
10	C34AlPAH	5.90	-0.068	5.30	1.11
	C35AlPAH	5.70	-0.066	5.28	1.08
11	C38PAH	5.40	-0.074	5.37	1.01
	C39PAH	5.41	-0.073	5.37	1.01

2.2.3.2.2 Heat Transfer Coefficient of Pre-coated Test Sections

The following figures (Figure 2-11 to Figure 2-15) show the heat transfer coefficient of the pre-coated test section at the outlet compared to that of the bare test sections. There appears to be no significant change in heat transfer coefficient between the coated test sections and the bare ones, within measurement uncertainty of <±10%. However, this can be only observed up to the CHF of the bare tube, as no HTC measurement is possible past CHF, which destroys the test section and ends the test. The results here are similar to those of Kim [2]. Notice that Figure 2-14 and Figure 2-15 show heat transfer coefficient measured using C31AlPAH and C32AlPAH test section at 1500 and 2500 kg/m^{2}s mass flux, respectively, up to 4MW/m^2 heat flux. The heat transfer coefficient here is not different from that of the bare tube case either. Overall, the heat transfer coefficient does not change with coated test sections. Figure 2-16, Figure 2-17 and Figure 2-18 show the heat transfer coefficient ratios of the pre-coated test sections to the bare test

section. For all three figures, the ratios stay within 20%, which shows more clearly that there was no change in the heat transfer coefficient in the pre-coated test sections.

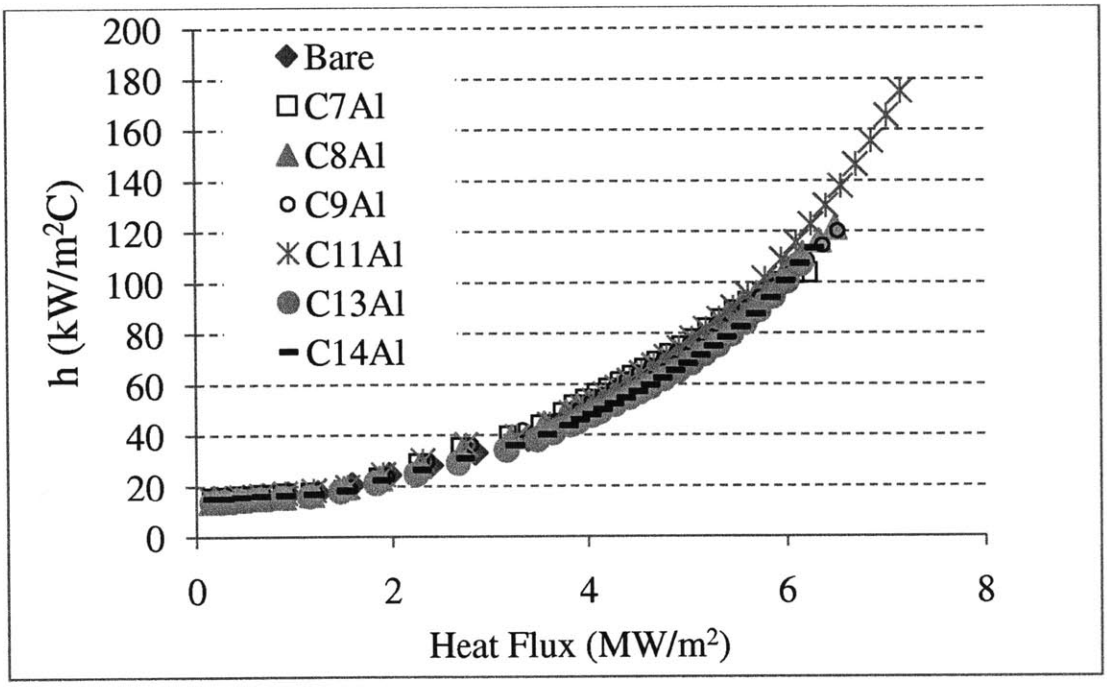

Figure 2-11: Measured Heat Transfer Coefficient of Test Section C7Al to C14Al

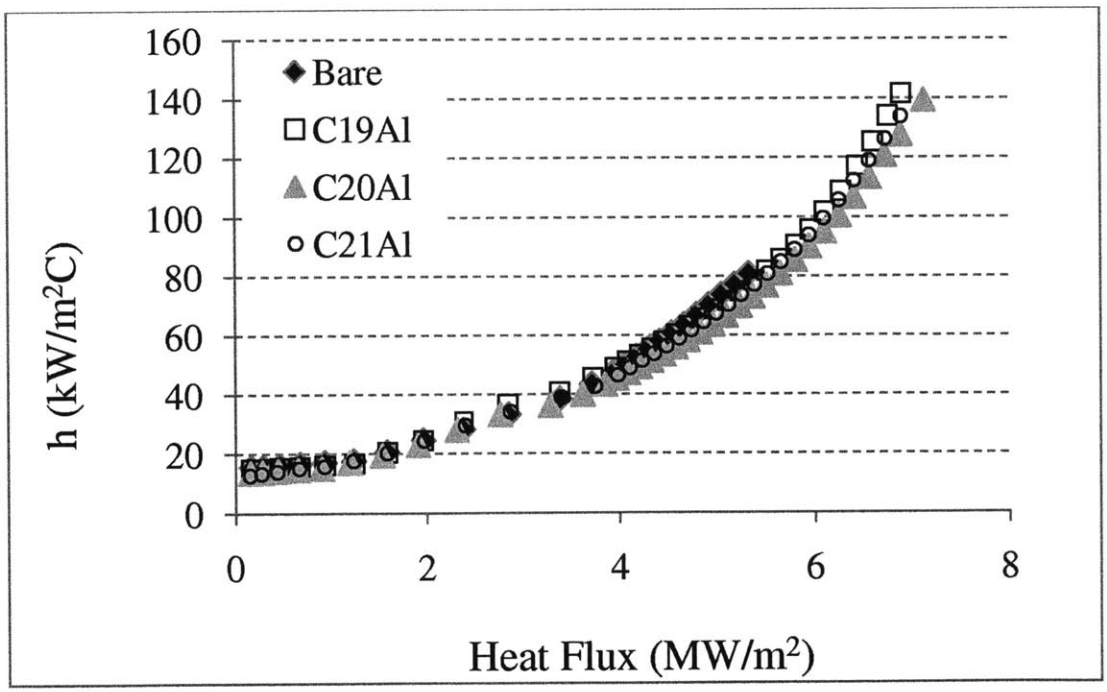

Figure 2-12: Measured Heat Transfer Coefficient of Test Sections C19Al to 21Al at G = 2500 kg/m²s

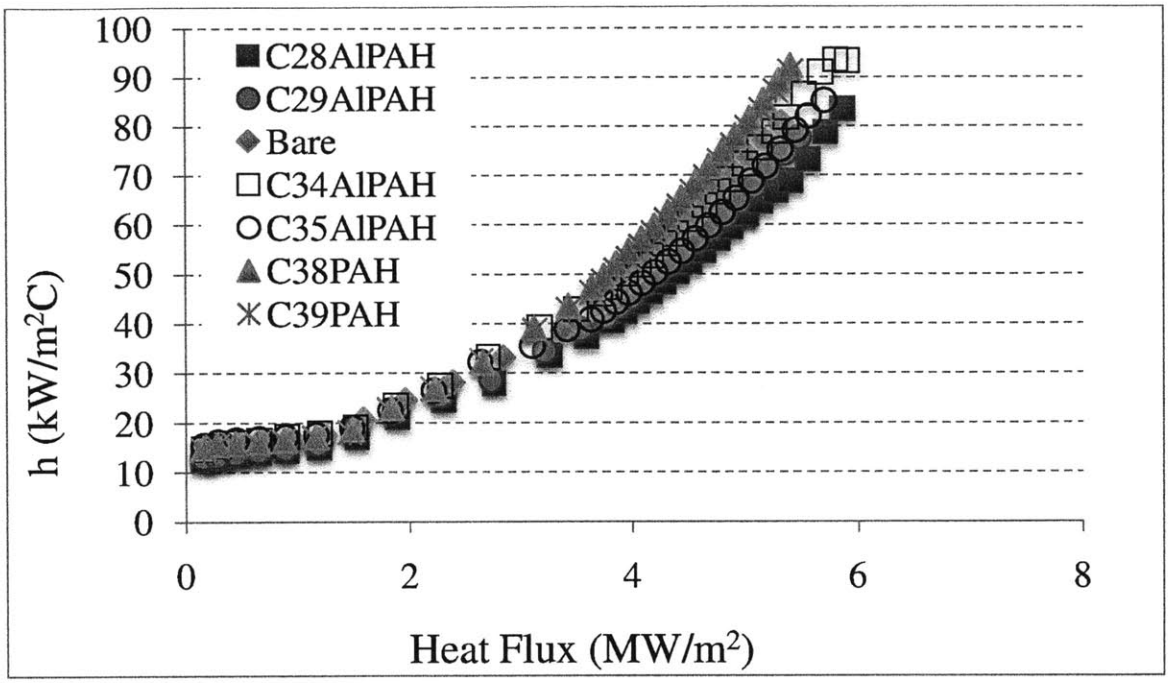

Figure 2-13:Measured Heat Transfer Coefficient of Test Sections Coated with Alumina/PAH at G = 2500 kg/m^{2}s

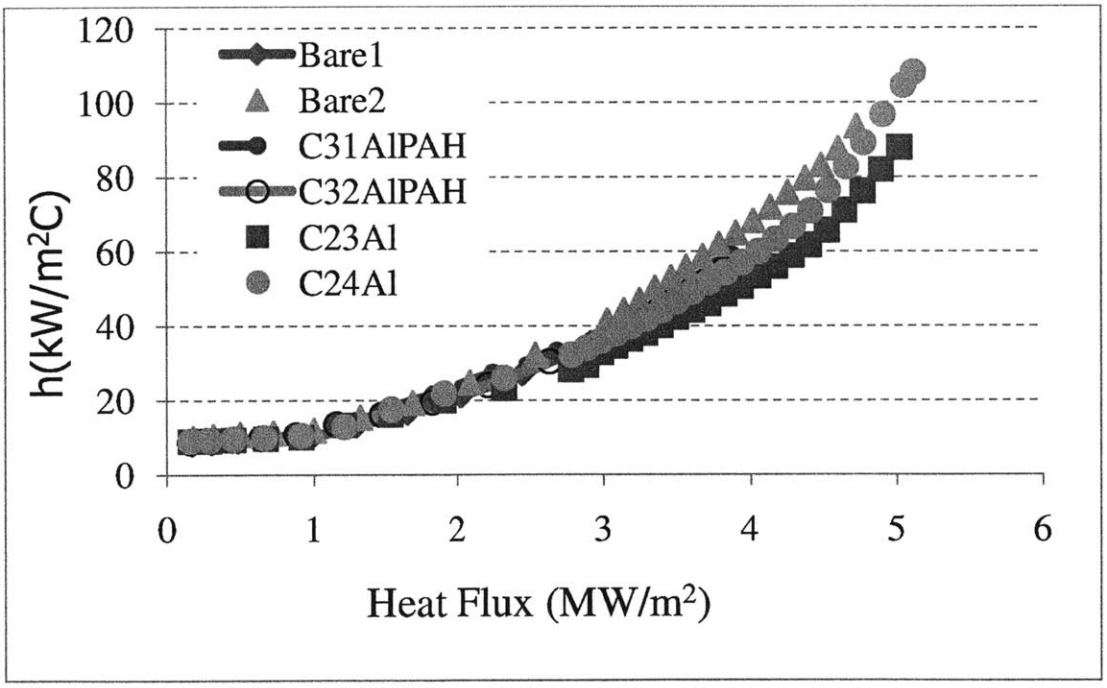

Figure 2-14: Measured Heat Transfer Coefficient of Test Sections at G = 1500 kg/m^{2}s (bare data is from S.J. Kim [2])

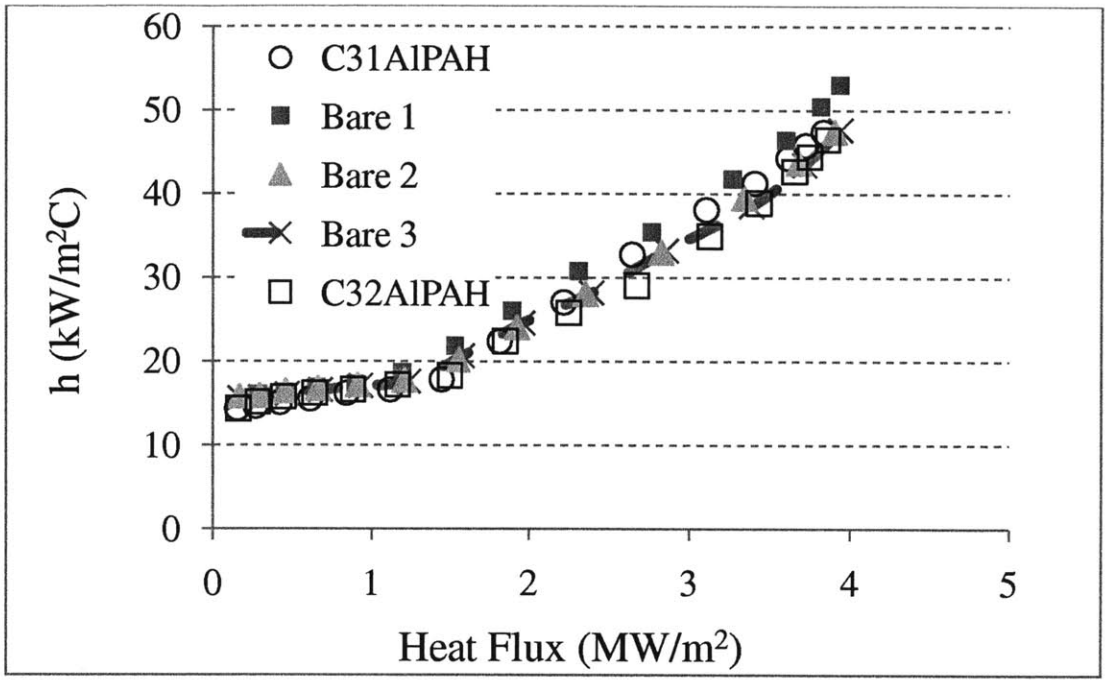

Figure 2-15:Measured Heat Transfer Coefficient of Test Sections C31AlPAH and C32AlPAH at G = 2500 kg/m^{2}s

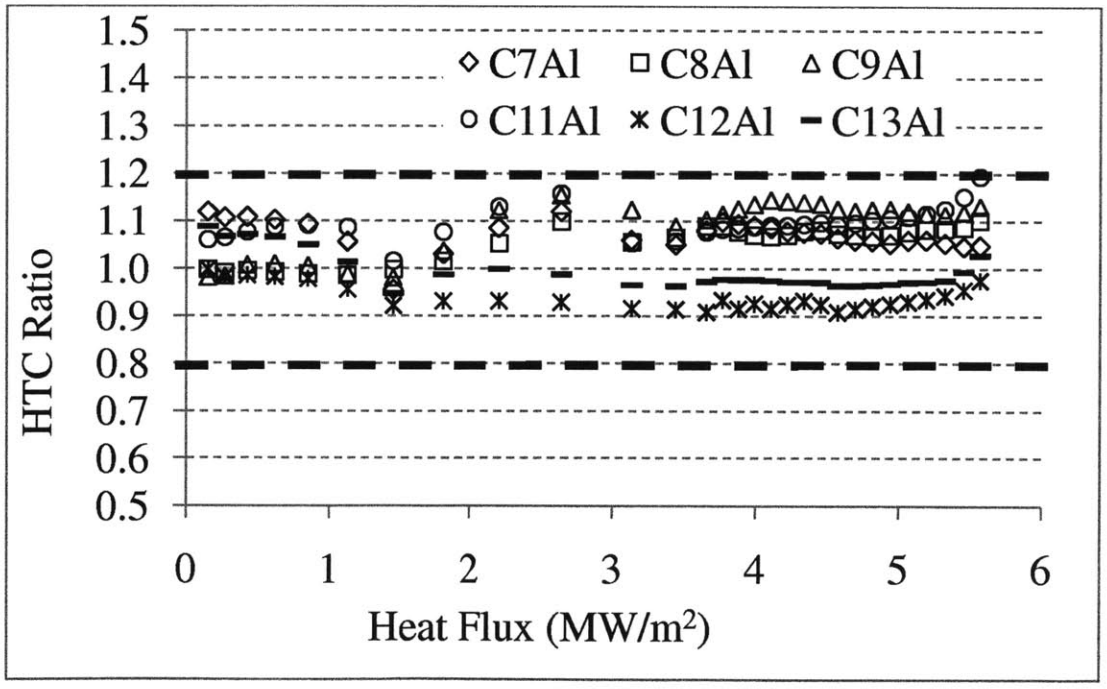

Figure 2-16: Heat Transfer Coefficient Ratio of Alumina Coated Test Section (C7Al to C13Al) to a Bare Test Section at G = 2500 kg/m^{2}s

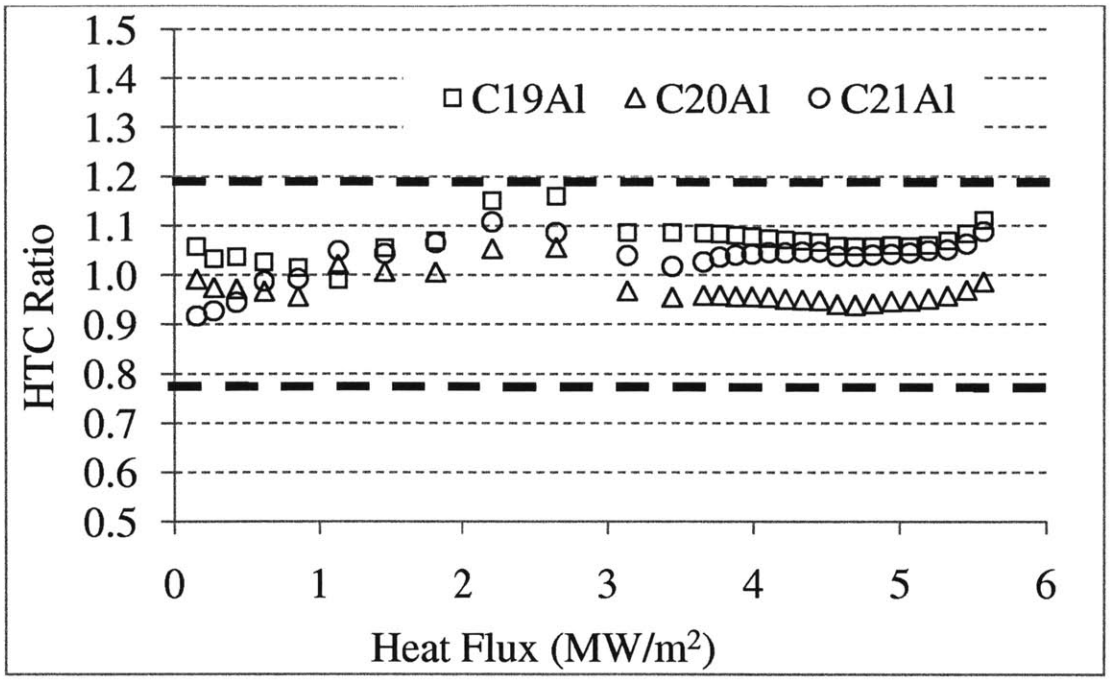

Figure 2-17: Heat Transfer Coefficient Ratio of Alumina Coated Test Section (C19Al to C21Al) to a Bare Test Section at G = 2500 kg/m^{2}s

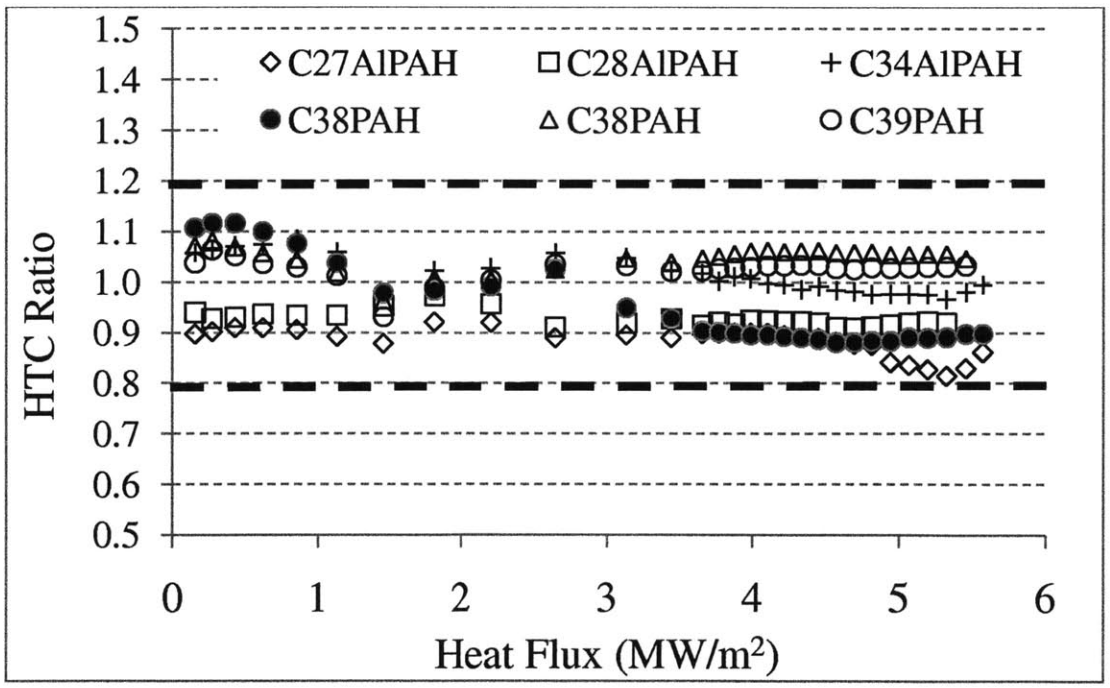

Figure 2-18: Heat Transfer Coefficient Ratio of Alumina/PAH Coated Test Section (C27AlPAH to C39PAH) to a Bare Test Section at G = 2500 kg/m^{2}s

2.3 Surface Characterization

After a CHF experiment, the test section was cut using Electrical Discharge Machine (EDM) into four quarters of length approximately 1.25 cm from the burn-out location. Scanning Electron Microscopy (SEM) and Energy Dispersive Spectroscopy (EDS) were then used to examine the cut test sections. Contact angle measurements and confocal microscopy were also performed to measure the wettability and the surface roughness of the test sections. In this section, SEM images will be discussed first, followed by confocal and contact angle measurements.

2.3.1 SEM Images

In Figure 2-19 , SEM images of the test sections C1Al to C6Al are shown. These were the test sections that were coated to verify that boiling-induced deposition would work. These SEM images show that there was some alumina particles deposition on the surface of the test sections; however, the coating layer was rather sporadic and there seemed to be little consistency between test sections coated under the same conditions. Therefore, subsequent coating was performed at higher heat flux and at a longer time interval to allow more boiling induced deposition.

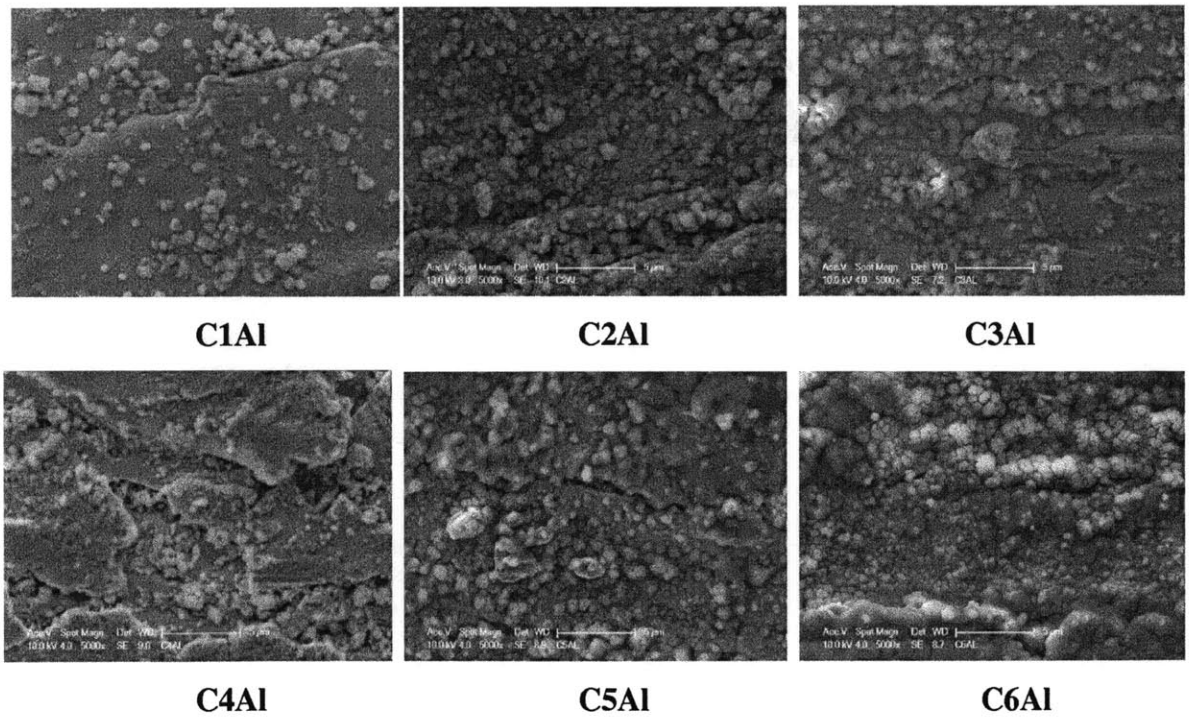

Figure 2-19: SEM Images (~5000X) of Test Section C1Al to C6Al

In Figure 2-20, SEM images of Alumina pre-coated test sections that were run in the two-phase loop are compared to those of the bare surfaces. Coating was present on all the test sections, but again, none of the coating was uniform. Nevertheless, there was enough coating at or near the CHF location such that CHF enhancement was observed in the test sections at 2500 kg/m^2s mass flux.

To verify that the coating layer was Alumina, EDS detector was used to identify the elemental composition on the surface. Some EDS spectra and their associated SEM are shown in Figure 2-21. Aluminum and oxygen were detected for all pre-coated test sections as expected. In addition, spherical features of the Alumina nanoparticle could be seen at this higher magnification. Similar observations could be said for test sections pre-coated with Alumina/PAH test sections. The coating was more sporadic here, and very different from test section to test sections. However, there seemed to be more coating in test section C34AlPAH to 36AlPAH compared to that on C27AlPAH to C29AlPAH. This could be due to the presence of 1000 ppm PAH in test section C27AlPAH to C29AlPAH. EDS spectra also confirmed the presence of Alumina nanoparticles. No CHF enhancement observed for these test sections, even though they had some coating. The coating for Alumina/PAH seemed much smoother (if there was coating) compared to the Alumina coating layer alone. Also, some Alumina/PAH coating seemed to have no particle at all on the bare surface. This could explain why there was no CHF enhancement for these Alumina/PAH test sections.

In Figure 2-23, SEM images of C38PAH and C39PAH test sections are shown. C38 and C39PAH test sections, which were coated using only 1000 ppm PAH water, look identical to that of **bare** surface, which was cut from the same long piece of tubes as all other test sections in this figure. This was probably the main reason there was no CHF enhancement at all for these test sections.

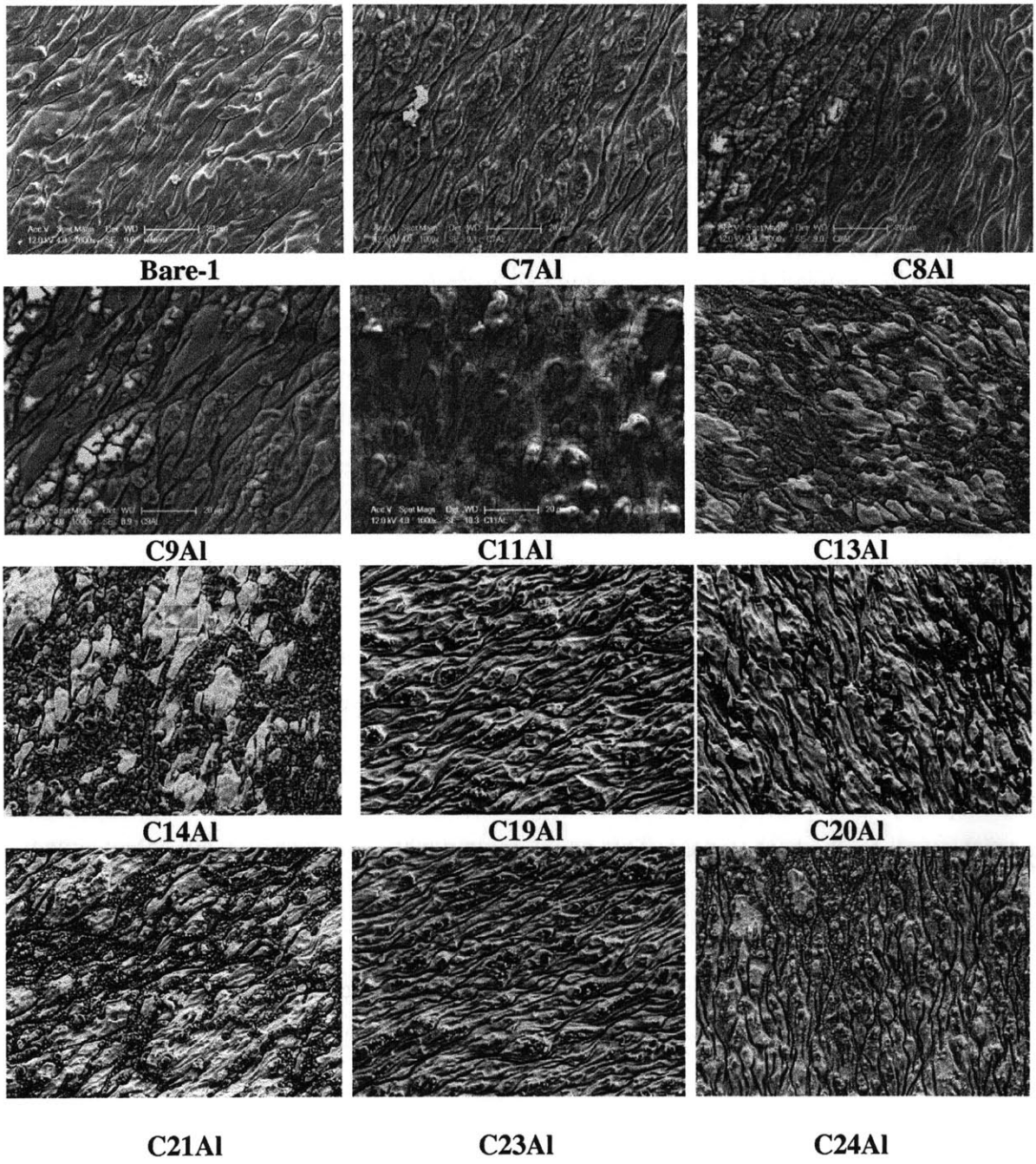

Figure 2-20: SEM Images (~1000x) of Alumina Coated Test Sections

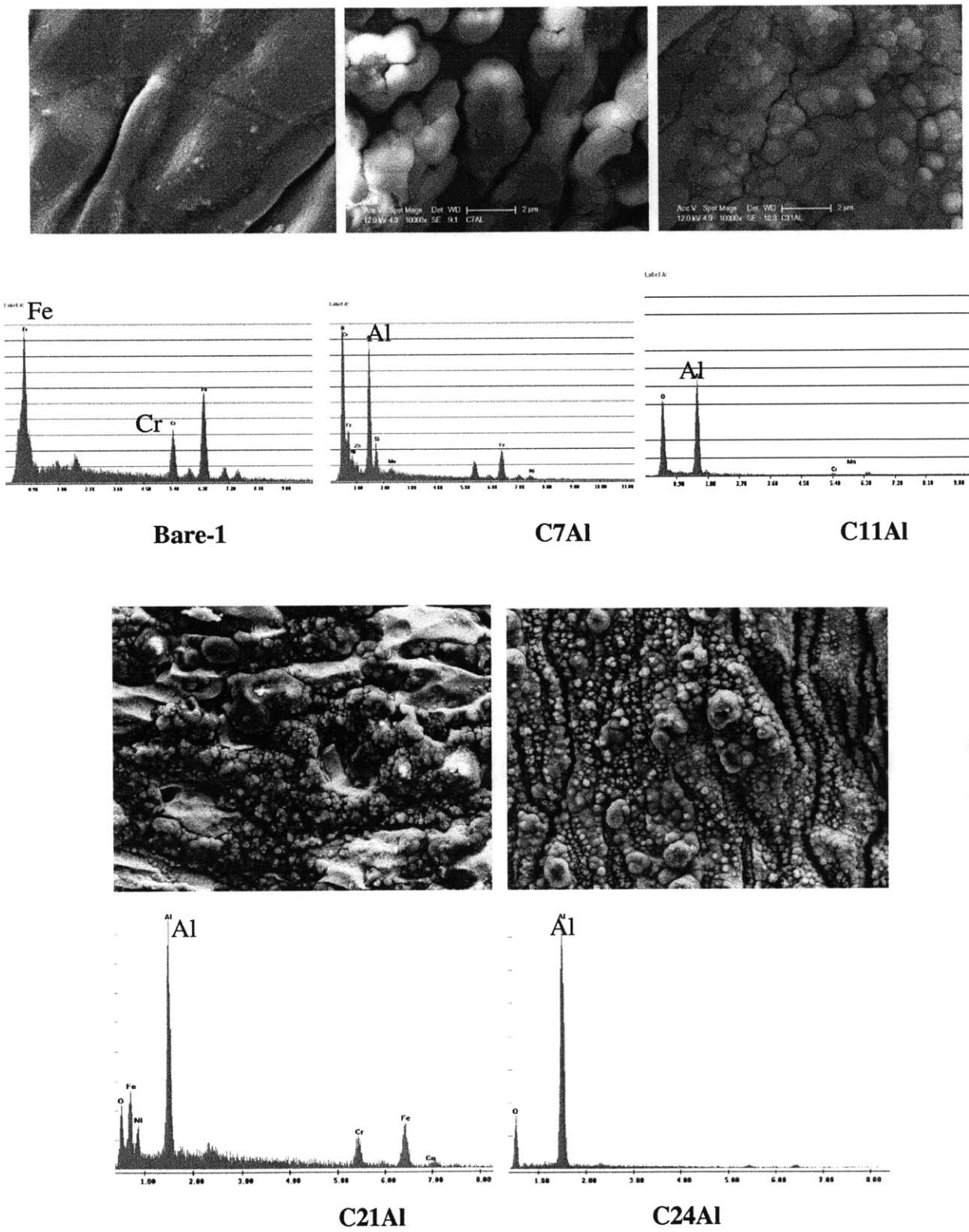

Figure 2-21:SEM images (~10000X) and their associate EDS spectrum

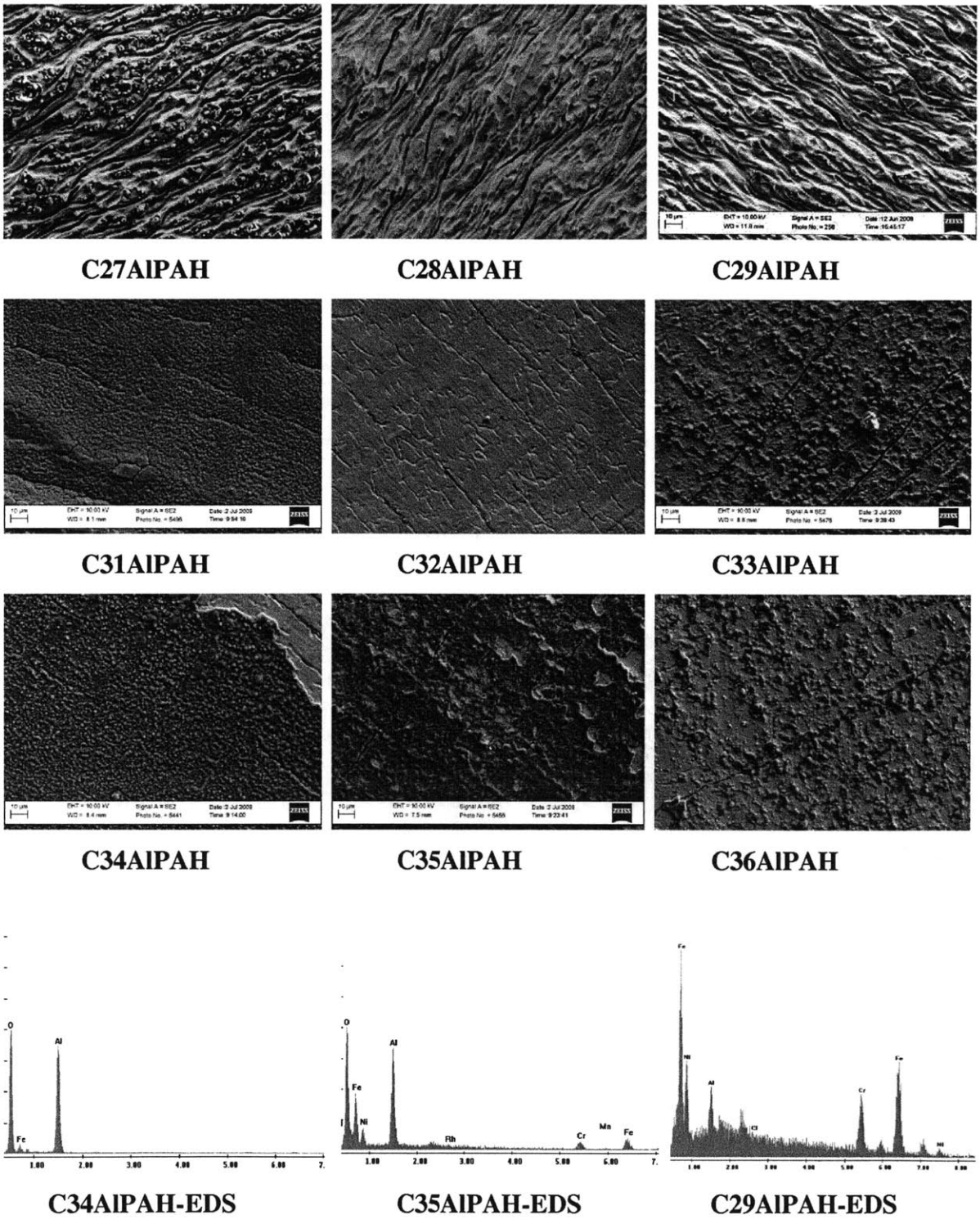

Figure 2-22: SEM images(~1000x) of Alumina/PAH Pre-coated Test Sections and Some of Their Associate EDS Spectra

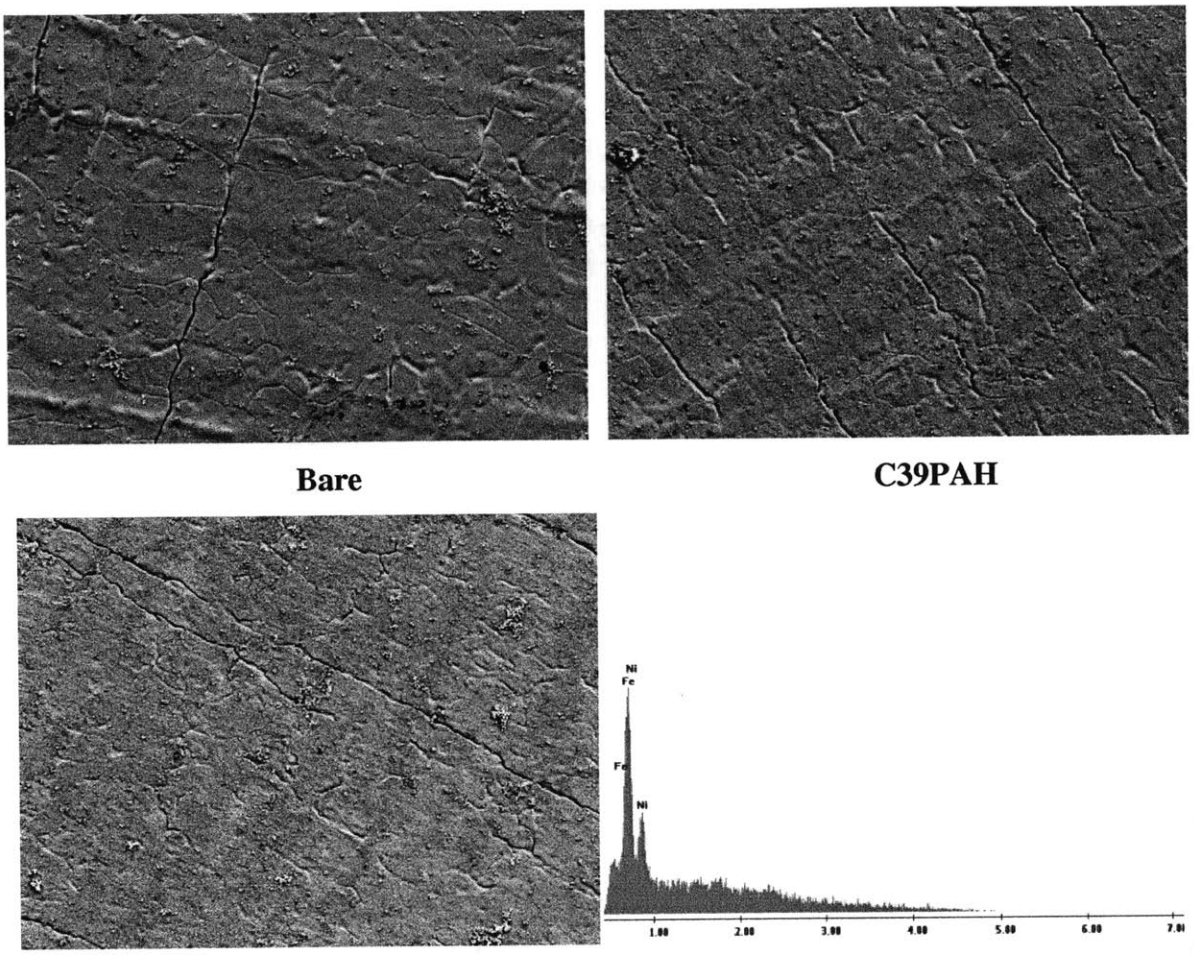

Figure 2-23: SEM images (~1000x) of PAH Pre-coated Test Sections and Some of Their Associate EDS Spectra

While SEM images and EDS spectra provide clear surface structures and composition, they do not adequately help explain why there was or was not a CHF enhancement with these pre-coated test sections. Therefore, contact angle measurement was performed to evaluate if there was enhanced wettability with the pre-coated layer. As mentioned previously, higher wettability generally allows higher CHF, at least in pool boiling. Table 2-6 lists the water static contact angle values measured for different test sections. The values listed are the average values of test sections in the same coating batch and their standard deviation. For each test section, the contact angle was measured at two to three different locations. The uncertainty for contact angle measurement was approximately ±5 degrees. As mentioned before, in order to do surface

characterization on the test sections, they needed to be EDM cut into four 0.5" long quarters from the burn-out point.

Table 2-6: Contact Angle Measurement (±5°) for Pre-coated Test Sections

Batch	Test Sections	Average (°)	Standard Deviation
1	Bare1, Bare 2	126.8	9.5
	C7Al to C11Al	113.3	17.2
2	Bare 3	68.9	1.7
	C13Al to C14Al	33.7	3.6
	C19Al to C22Al	38.1	8.0
	C28AlPAH to C30AlPAH	96.4	15.3
3	Bare 4	84.2	1.9
	C31AlPAH to C33AlPAH	50.3	12.5
	C34AlPAH to C36AlPAH	77.4	21.4
4	Bare 5	82.6	8.7
	C38PAH to C40PAH	75.1	13.8

In Table 2-6, the test sections were cut by EDM in four different batches. First of all, the contact angle for test section C7Al to C10Al in batch number one are relatively high even though they gave CHF enhancement. The contact angle value for bare surface was also much higher than the expected value of 70-90 degrees for contact angle of water on stainless steel. There might have been some contamination of the test sections during the EDM process for this batch, which was done by an outside vendor, such that the all contact angle values were higher than usual. For this reason, for each subsequent EDM cutting of batches pre-coated test sections, (which was done at MIT after finding an available EDM machine), a **bare** test piece of tube was also cut at the same time to be used as a reference.

For test section C13Al to C14Al and C19Al to C22Al, their contact angles were lower than those of the bare ones. For test section C28AlPAH to C30AlPAH, the contact angles were a little higher than that of the bare one. Both of these values are expected because C13Al, C14Al, and C19Al to C21Al gave CHF enhancement while the others did not. Lower contact angle means higher wettability, which usually means higher CHF. The average contact angle for test section C34AlPAH to C36AlPAH was a little bit lower than that for bare surface, even though they did not give any CHF enhancement. On the other hand, test section C38PAH to C40PAH had contact angle similar to than that of the bare surface, and their CHF values were identical to that of bare surface. This means that wettability may not be the only factor that affects flow boiling

CHF. Notice that some of the standard deviation of contact angle measurements are high due to scatter of the data. Representative contact angle images are shown in Figure 2-24.

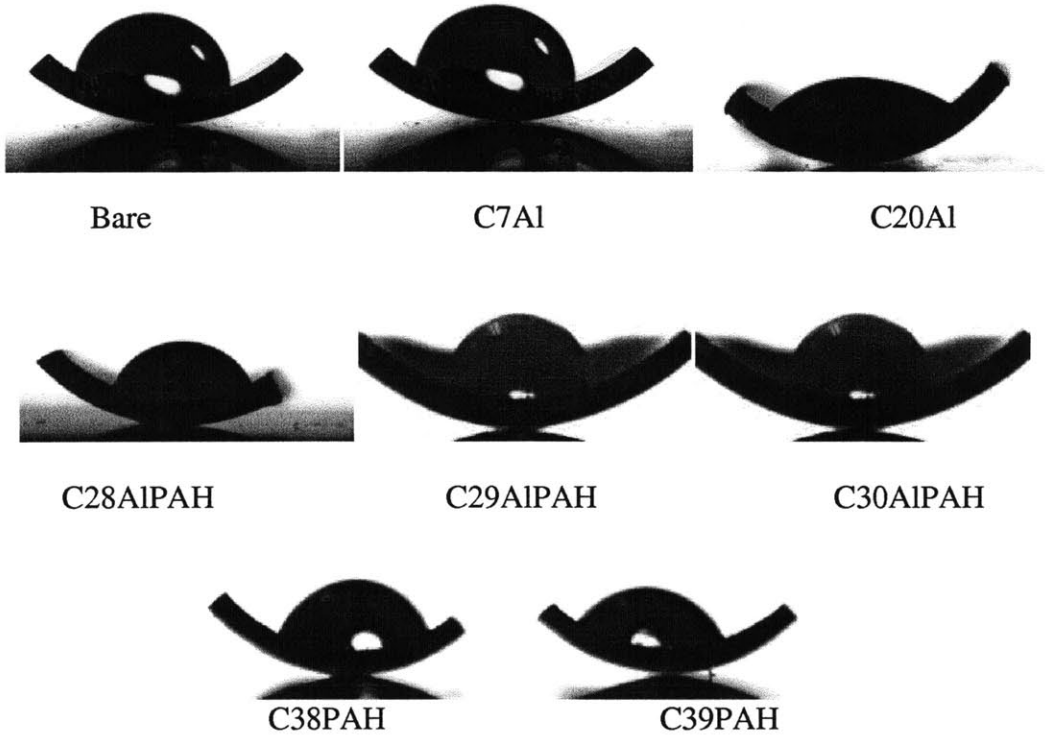

Figure 2-24: Representative Contact Angle of Water on Bare and Pre-coated Test Sections

It is also useful to look at the surface roughness of the test section to see how the coating can change the surface structure. This was done using confocal microscopy, the results of which are listed in Table 2-7. There was no significant change in *Ra*, which is defined as the arithmetic average of surface profile amplitude. There was no significant change in the surface roughness ratio either due to the coating layer. The surface roughness ratio is defined as the ratio between the actual surface area to the projected area. Also, there is no observable trend in terms of CHF enhancement and change in surface roughness ratio. This is another indication of the coating inconsistency from test section to test section. Figure 2-25 shows some representative Confocal images of the test sections. There is no significant change that can be observed from a bare surface to a pre-coated surface, as already indicated by the measured values.

Table 2-7: Confocal Microscopy Results (Average Values of Two Locations)

Tube ID	Ra (μm)	Projected Area (μm^2)	Actual Area (μm^2)	Roughness ratio
As-received	2.16	67748	87575	1.29
Bare	2.46	67881	90136	1.33
C7AlCHF	1.42	67947	83826	1.23
C8AlCHF	2.64	67880	84286	1.24
C9AlCHF	2.18	67947	84745	1.25
C10AlCHF	2.15	67947	90806	1.34
C11AlCHF	1.68	67747	84902	1.25
C13AlCHF	1.84	67947	84215	1.24
C14AlCHF	3.48	67880	126482	1.86
C19AlCHF	1.83	67880	86833	1.28
C20AlCHF	2.39	67814	88213	1.30
C21AlCHF	1.77	67880	86894	1.28
C22AlCHF	2.04	67880	85579	1.26
C23AlCHF	1.91	68013	92112	1.35
C24AlCHF	1.80	67677	82446	1.22
C25AlCHF	1.61	67474	88215	1.31
C27AlPAHCHF	2.46	67639	86627	1.28
C28AlPAHCHF	2.49	67814	88627	1.31
C29AlPAHCHF	2.41	67681	92831	1.37
C30AlPAH	2.20	67681	87739	1.30
C31AlPAH	2.07	67814	105308	1.55
C32AlPAH	3.34	67814	86794	1.28
C33AlPAH	1.61	67747	72933	1.08
C34AlPAHCHF	2.42	67791	93021	1.37
C35AlPAHCHF	0.75	67814	70751	1.04
C36AlPAH	2.24	67814	82464	1.22

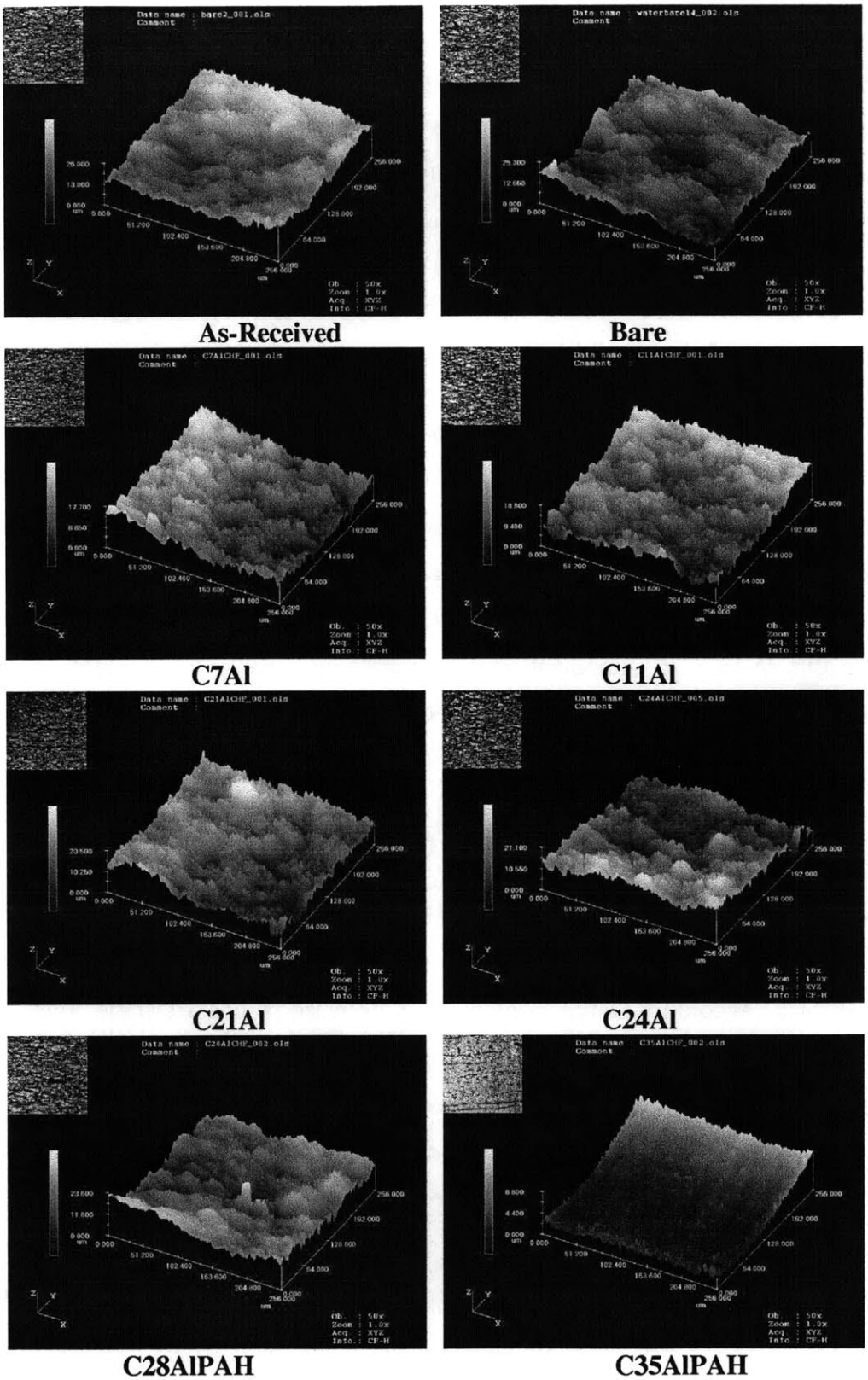

Figure 2-25: Representative Confocal Images of Flow Boiling Test Sections (256μm by 256 μm)

Another parameter that could affect CHF is the porosity of the surface. However, for the current test sections, it would be impossible to measure porosity with reasonable accuracy to draw any conclusion. However, the deposited nanoparticles created some porous structures on the surface, which could increase the surface's overall porosity. This increase in surface porosity could help enhance CHF by creating capillary wicking.

2.4 Analysis of Surface Parameters Affecting Flow Boiling CHF

The experimental results showed that the CHF enhancement, when present, was purely due to surface effects since only deionized water was used in the experiment. From the surface characterization done for pre-coated test section, it appeared that the nanoparticle deposition did not change the surface roughness of the test sections significantly. The Alumina nanoparticle coating did help enhance wettability. The nanoparticle coating layer also created a more porous structure compared to the bare surface. However, measurement of porosity of test sections was not possible due to lack of equipment and the uncertainty would be too high. The surface wettability and porosity affecting flow boiling CHF will be discussed next.

2.4.1 Effect of Wettability on Flow Boiling CHF

For pool boiling CHF, it is known that everything else being equal, an increase in surface wettability enhances CHF. Kandlikar [53] developed a model relating contact angle to pool boiling CHF based on the hydrodynamic behavior for the vapor liquid interface of the bubble at the heater surface. According to this correlation, a decrease of contact angle from 80° to 0° (super hydrophilic surface) enhances CHF by approximately 100%. Extending from this model for pool boiling CHF, Kandlikar [54] proposed a similar one for flow boiling CHF. In this model, CHF is defined when the advancing liquid front (upstream) cannot rewet the heater surface again after drying out during the flow boiling process. The force balance for the vapor-liquid interfacial forces including inertia force due to bulk flow, shear force and evaporation force, which causes a velocity difference between the approaching liquid and evaporating vapor front, is represented in Figure 2-26. Here, $F_M, F_I, F_{S,1}, F_{S,2}$ and F_τ are respectively the evaporation momentum force, the inertial force, surface tension forces and shear force. θ_r is the receding contact angle. CHF occurs when the evaporation force overcomes the sum of all other

forces. The expressions for these forces are in equation (2-12). The expression for CHF as a function of contact angle and other parameters is shown in equation (2-13) [53].

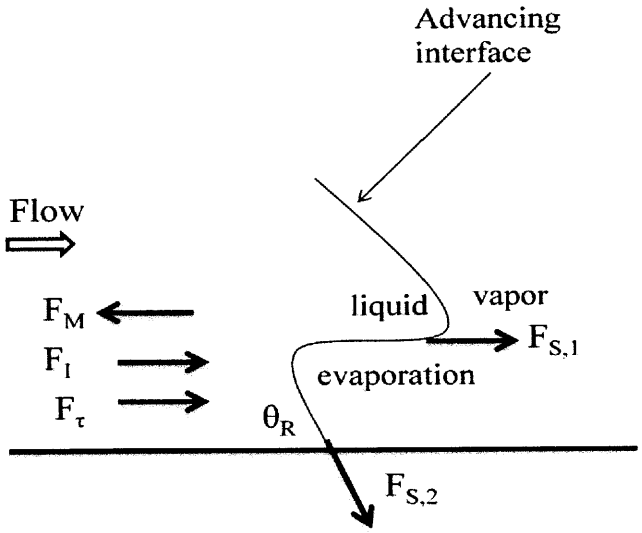

Figure 2-26: Force Balance for Liquid-Vapor Interface in Flow Boiling per Kandlikar's Model

$$
\begin{aligned}
F'_{S,1} &= \sigma \cos(\theta_R) \\
F'_{S,2} &= \sigma \\
F'_I &\sim \frac{(G^2 D(1-x))}{\rho_m} \\
F'_T &\sim \frac{(\mu_l G(1-x))}{\rho_L \sigma} \\
F'_M &= \left(\frac{q_{CHF}}{h_{fg}}\right)^2 \left(\frac{D}{\rho_v \sigma}\right)
\end{aligned}
\tag{2-12}
$$

$$
\left(\frac{q_{CHF}}{h_{fg}}\right)^2 \left(\frac{D}{\rho_v \sigma}\right) = a_1(1+\cos(\theta_r)) + a_2 \frac{(G^2 D(1-x))}{\rho_m \sigma} + a_3 \frac{(\mu_l G(1-x))}{\rho_L \sigma} \tag{2-13}
$$

where a_1, a_2 and a_3 are constants determined from experimental data, which are proposed to be 1.03E-4, 5.78E-5 and 0.783, respectively. *G, D, x* are the mass flux, the diameter of the test section, and the flow quality, respectively. Again, the first term on the right hand side represents the surface tension force, which involves contact angle. The second and third terms represent the

Weber number (ratio of inertia force over surface tension) and Capillary number (ratio of viscous force over surface tension). The ratio of flow boiling CHF as the surface wettability goes up (contact angle decreases) is shown in Figure 2-27. Here the flow quality was assumed to be 0. The surface wettability seems to have little effect on flow boiling CHF according to this model.

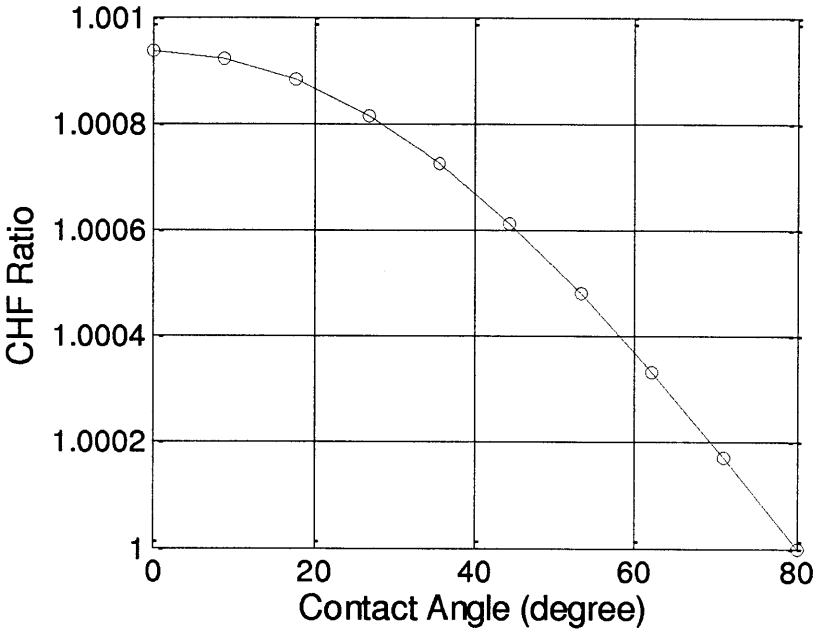

Figure 2-27: Flow Boiling CHF Dependence on Contact Angle

While this model only applies to saturated flow boiling CHF and for channel diameter less than 3.36 mm, the trend suggests that the capillary and viscous force have dominant effect on CHF in flow boiling compared to that of wettability. This is consistent with an earlier model proposed by Kuan and Kandlikar [55]. Note also that data reported for benchmarking of this model did not mention measurement for contact angles. These two models are different from the pool boiling model since there is strong inertia force in flow boiling, which is absent in pool boiling. Wettability, which links to surface tension force, has a much stronger effect in pool boiling CHF. In this study, the Alumina nanoparticle layer helped enhance wettability, which seemed to have an effect on CHF enhancement. A controlled surface wettability of flow boiling CHF study should be performed in the future.

2.4.2 Effect of Porosity on Flow Boiling CHF

The nanoparticle deposition created a porous layer on the test sections as confirmed by SEM images. For a wettable liquid/surface combination (contact angle less than 90 degrees), porous structures enhance capillary wicking, which is the ability of the surface pores to draw liquid into the surface via capillary force. As mentioned before, quantitative measurement for porosity for the test sections would be challenging and have very high uncertainty. A more qualitative discussion of how porosity can help enhance CHF is presented instead.

In the literature, data for flow boiling CHF with porous coating is scarce compared to that in pool boiling. For example, Schroeder-Richter et al. [56] sintered Inconel-600 tube test section with Inconel-600 particle of 80-100 μm with thickness of approximately 180 μm and measured CHF at low mass flux (0-200 kg/m^{2}s) and different pressures (1-8.0 bars). At atmospheric pressure, they found small enhancement of CHF of the coated tube at low mass flux but deterioration of CHF at mass flux of 200 kg/m^{2}s. At pressure of 7 bars, they found little change between the plain tube and the coated tube. Overall, there was no clear trend that porous coating enhancing CHF. On the other hand, Sarwar et al. [57] found up to 25% CHF enhancement for test section coated with porous Alumina coating layer at mass fluxes between 100 and 300 kg/m^{2}s. They suggested that the enhanced wettability helped increase CHF but agreed that how surface coating affected flow boiling CHF needed to be explored further. Rainey et al. [58] coated copper squares with Aluminum particle using ABM technique, and using FC-72 as the coolant, measured flow boiling heat transfer coefficient and CHF of these surfaces. They found overall enhancement in CHF for the porous surface at different flow velocity (0.5 - 4 m/s) and sub-cooling conditions (20, 10, 4K). They noticed that the CHF enhancement of the porous surface from the plain surface decreased with increasing fluid velocity. Vafaei and Wen [59] measured CHF of Alumina nanofluid in a horizontal micro channel and found CHF enhancement at all concentration (0.001 vol% to 0.1 vol%) for mass flux from 600 to 1600 kg/m^{2}s. The maximum CHF enhancement was up to 51%. Similar to other nanofluid studies, the CHF enhancement was due to the deposited layer of the nanoparticle in the micro channel. However, none of the study above suggested a CHF enhancement mechanism due to the characteristics of the porous coating layer.

There exists virtually no CHF model and/or correlation for porous coating in flow boiling CHF. In pool boiling CHF, the hot/dry spot theory states that when a surface is subjected to high heat flux, hot/dry spots are formed at the bases of the bubbles at the nucleation sites. When the hot/dry spots can be rewetted upon departure of the bubbles, they are considered reversible. However, when the rewetting does not occur due to poor wettability of the surface, the hot/dry spot is irreversible, which can lead to a rapid increase in the surface temperature and cause burn-out. The capillary wicking from the porous structure can help supply liquid to these hot/dry spots at a faster rate, which can help dissipate heat quickly, and hence delay CHF.

For pool boiling CHF models including the effect of capillary wicking, the viscous-drag liquid-choking limit model for fluid flowing through a porous stack by Liter and Kaviany [60] seems most appropriate. In this model, it is assumed that there is separate liquid and vapor flow. The fluid flows through the porous coating stack while the vapor escapes through channels between stacks, as shown in Figure 2-28.

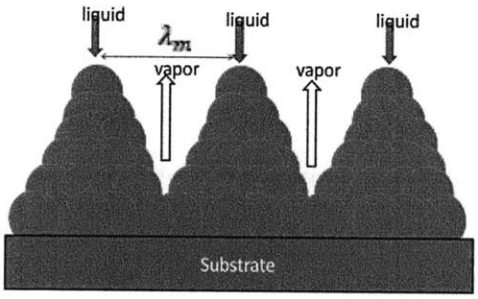

Figure 2-28: Liquid and vapor flow path in viscous-drag choking limit model

Capillary wicking and gravity are the driving forces for liquid down flow while buoyancy drives vapor flow. Evaporation of fluid is assumed to be along the side of the coated stack. In order to cool down the substrate, an adequate amount of fluid is required to flow through the stack. As the heat flux increases, more liquid is evaporated, which means a higher flow rate of liquid is required. This corresponds to higher pressure loss from the top of the stack to the substrate. At some point, the flow rate of resupplying liquid required is high enough such that the pressure drop exceeds that of the capillary and gravity force combined. This prevents liquid from being resupplied any further. This point is defined as CHF.

An analytical approximation, by making further assumptions, such as cylindrical tube instead of conical stack, and that gravity is negligible, provides an expression for CHF [60] as

$$\frac{(q''_{CHF,v})_{\theta=0}}{\epsilon_s C_J \frac{\rho_l \sigma h_{fg}}{\mu_l} \frac{(\kappa\epsilon)^{0.5}}{\delta_s}} = 1 - \frac{C_E}{C_J} \frac{\delta_s}{\epsilon_s^2 \epsilon^{0.5}} \frac{(q''_{CHF,v})^2_{\theta=0}}{\rho_l \sigma h_{fg}} \quad (2\text{-}14)$$

where $\kappa, \epsilon, \epsilon_s$ are the permeability, porosity and base to surface area ratio, respectively. $C_j = 53$; C_E: Ergun coefficient; δ_s is the coating thickness of the stack after the first base layer. For contact angle θ larger than 0, there is a $0 \leq C(\theta) \leq 1$ factor that can be multiplied for the CHF value. This $C(\theta)$ varies from 1.0 to 0.3 as contact angle increases from 0 to 30 degrees. Using this model, the authors estimated CHF value of up to 4.7 MW/m^2 for pentane with surface coated with particle diameter of 200 micrometers, and thickness of 6 times the particle diameter. This is an extremely high value for CHF of pentane. Examining the model further, it seems that CHF increases with decreasing particle diameter, as shown in Figure 2-29, where the reference particle diameter (d_0) is 100 μm.

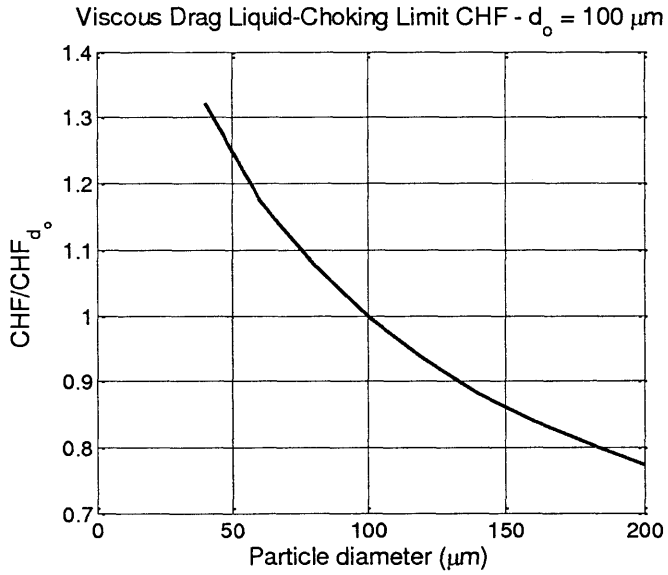

Figure 2-29: CHF as Function of Particle Diameter Based on Liter and Kaviany model

The parameters in the model by Liter and Kaviany [60] include many characteristics of the porous coating layer of the nanoparticles that cannot be determined accurately in this study due to the sporadic/random coating structure of the nanoparticles. Therefore, applying such model for the test sections here is impractical. Furthermore, this model is only applicable for pool boiling. Nevertheless, the model suggests that porosity/capillary wicking plays an important role in CHF.

2.5 Summary of Pre-coated CHF Experiments

Flow boiling induced deposition of Alumina nanoparticles on the test section surface, which helped enhance subcooled flow boiling CHF of water up to 40% at 2500 kg/m^{2}s mass flux. This verified that nanofluids flow boiling CHF enhancement is due to the nanoparticle deposited on the surfaces. Surface changes due to nanoparticle deposition including wettability and porosity could contribute to the CHF enhancement. While the enhancement in wettability seemed to help enhance CHF, it did not seem to be the only factor. Porous structure from the nanoparticle deposited layer could increase the porosity of the surface, which can enhance CHF. Thus, existing models fail to predict the CHF enhancement due to the nanoparticle coating layer. There is a need for a study of effects of individual surface parameter on flow boiling CHF.

3 Surface Effects on Quenching Leidenfrost Point

3.1 Introduction

Quenching heat transfer is the process of rapid cooling of a hot object by submersion in cooler liquid. The process starts in a film boiling regime, where a layer of vapor encapsulates the hot surface, preventing liquid coming in contact with the surface. During film boiling, conduction/convection through the vapor and radiation are the main heat transfer mechanisms. These modes of heat transfer are not as effective as nucleate boiling, thus resulting in long evaporation time of the liquid. As the temperature of the hot surface approaches the Leidenfrost point (LFP), the minimum temperature to sustain stable film boiling, liquid-solid interface can be formed again due to short intermittent interaction of the liquid and solid. Below the Leidenfrost point, transition boiling takes place with intermittent solid-liquid contact which affords a much higher heat transfer rate than film boiling. As the hot object cools down further, the boiling regime changes to nucleate boiling, which is the most effective heat transfer mechanism.

In the nanofluid quenching works described in Chapter 1, the deposited nanoparticle layers changed several surface parameters at the same time, thus making it difficult to quantify the importance of each surface effect. While it is challenging (in terms of surface preparation and experimental execution) to perform an experimental parametric study on surface effects in flow boiling CHF, an experimental setup can be designed to study separate surface effects on quenching, focusing on single droplet quenching. In the literature, single droplet quenching experimental and numerical studies have been reported previously; however, none has performed a separate surface effect study. Some examples of single droplet quenching work are summarized below.

Shen et al. [61] studied dynamic behavior of a single droplet (We =25, Re~1700, d ~1.2 mm) of water and carbon nanotube nanofluids (0.2% by weight) using high speed video (HSV) and infrared (IR) cameras. The surfaces included polished silicon, gold-coated silicon and nano-structured porous silicon. Surface temperature of the heater was varied from 68.9 to 185 °C. The first parameter of interest was maximum spreading diameter. The Prewitt method of edge detection was used for image analyses. The spreading of the droplet diameter stopped earlier in

the boiling case compared to the non-boiling case. The maximum diameter was not much different for different surface temperatures. Between the different surface finishes, initial spreading for non-heating and heating surface is about the same. The droplet had largest equilibrium diameter on non-heating polished surface while water on nano-structured surface had largest equilibrium diameter for the case of heating and boiling surface. For the case of nanofluid, similar behaviors were observed as those of water droplet. Four models were used to predict the dissipation terms for maximum spreading diameter (Chandra, P-F, Mao and Liu). Nanofluids spread much further compared to water. The evaporation time was found to be shorter for nanofluid on polished surface and water on nano-structured surface compared to that of water on polished surface. This was thought to be due to the increased spreading diameter of nanofluid and nano-structured surfaces. The M-K model was used to predict the dynamic contact angle. The results agree with experimental data at low impact velocity.

Moreira et al. [62] provide a comprehensive review of single droplet and spray impingement on dry, non-heated and heated surface as well as on liquid film. When a droplet impacts on a solid non-heated surface, it can be characterized by impact energy (base on height of droplet) or by time scale (contact duration). The different interactions include stick, spread, splash, fingering, partial rebound and rebound. For droplet impacting on heated surface, there are four main different heat transfer regimes: single phase/film-evaporation, film boiling/Leidenfrost regime, transition boiling, and nucleate boiling. Many defined Leidenfrost as a dynamic property, the point at which a droplet rebounds from the vapor layer. Various relationships between thermal characteristics and droplet/surface parameter have been presented in the literature. For example, Leidenfrost temperature increases with surface roughness for the impacting droplet, while T_{CHF} is not very sensitive to impact conditions. In each of these heat transfer regime, all the possible impact mechanisms as on cold surface are possible. This makes the phenomena of droplet impacting heated surface rather complex. Moreira et al. [62] also reviewed correlation for heat transfer for spray impact scenarios. The Nusselt number seems to depend on the Reynolds, Prandtl, Weber and Jacob number.

Yarin [63] reviewed hydrodynamics (experimental and modeling) of single droplet impacting liquid thin film and solid dry surface. For droplet impacting dry surface, six different interactions

were classified: deposition, prompt splash, corona splash, receding breakup, partial rebound and complete rebound. The occurrence of the stage depends on the impact velocity and solid surface's properties (wettability, surfaced roughness). Therefore, traditional dimensionless groups (e.g. Weber, Reynolds and Bond numbers) are not sufficient to quantify each state since they do not involve surface roughness and wettability, the two very important characteristics of a dry surface. For modeling of droplet impacting on dry surface, maximum spreading diameter can be predicted using semi-empirical analytical models by Chandra and Avedisian [64], Mao et al. [65], Pasansideh-Farf et al. [66]). Lubrication theory is traditionally used to approximate equations for studying spreading of the drop. Model of drop rebound has also been investigated by many researchers.

Finally, Manzello and Yang [67] used HSV to study dynamics on water droplet impinged on wax at different temperature and droplet velocity. They observed liquid film recoiled faster with increasing wax surface temperature at lower We number (We=27). However at higher We number (We=150), Rayleigh instability caused rise of an unstable liquid column above the surface. Upon the wax reached its melting point of 75°C, water droplet impinging liquid wax behaved differently from that on solid wax. No separate droplet was observed from the jet formed in the wax.

The above examples are selected examples of a plethora of research done on single droplet hydrodynamic behavior and quenching heat transfer. The work here will contribute further to this library of single droplet quenching data. More importantly, the results for this work can be used for potential applications in nuclear reactors. Quenching heat transfer plays an important role in light water reactor (LWR) safety, especially during accident scenarios, where the hot solid fuel pins are quenched by the cold water from the emergency core cooling systems to prevent fuel failure. Since LFP is the minimum temperature to have stable film boiling, the higher LFP, the faster the temperature of the hot fuel drops to transition boiling regime. This regime has much better heat transfer characteristic compared to film boiling, which helps promote cooling of the hot fuel rods faster. Therefore, enhancing LFP is desirable. In this study, the effect of individual surface parameters including roughness, wettability and nano-porosity on single droplet quenching LFP, will be determined. The results here can be used to optimize surface parameters

for quenching application, and to provide data for models of quenching heat transfer in nuclear reactors.

3.2 Experiments

3.2.1 Surface Preparation

Surface roughness height was controlled in the range from 0 μm to 15 μm (with 5 μm increment) by fabricating cylindrical posts of ~5 μm diameter on a nano-smooth silicon wafer (thickness 380 μm). The posts were fabricated using photo-lithography with deep reactive-ion etching process, and were arranged on a square array of large pitch (500 μm), to prevent secondary effects, such as capillarity. The deep reactive-ion etching process (shows in Figure 3-1) to create the posts on silicon wafer was as follows. First, a layer of Hexamethyldisilazane (HMDS) primer was deposited on a silicon wafer via a vapor deposition at 150 °C. Then, a layer of negative photo-resist, NR71-1000P, was coated on the wafer using a spin coater spinning at 3000 rpm for 30 seconds. The HMDS helped adhesion of the negative photo-resist to the wafer. Post baking on hot plate at 150°C for two minutes helped dry the negative photo resist. Next, the wafer was exposed under ultraviolet (UV) light of wavelength 365 nm to 400 nm for 20 seconds. A mask was inserted between the UV light source and the wafer to imprint the pattern of square array of 5μm circles at 500 μm pitch, where the UV light interacted with the negative photo resist. After exposure to UV, the wafer was dried again on a hot plate at 100 °C for two minutes. The wafer was then developed in RD6 developer for 20 seconds. All the negative photo resist on the wafer, except for those that had been exposed to UV light underneath the mask, was washed away by the RD6 developer. The remaining patterned negative photo-resist protected the wafer underneath during reactive-ion etching, which created a square array of 5 μm diameter posts at 500 μm pitch. Subsequently, the wafer was cleaned with piranha solution (25% hydrogen peroxide, 75% sulfuric acid) to remove all negative photo-resist. Figure 3-2 are SEM images of surfaces with micron-size posts.

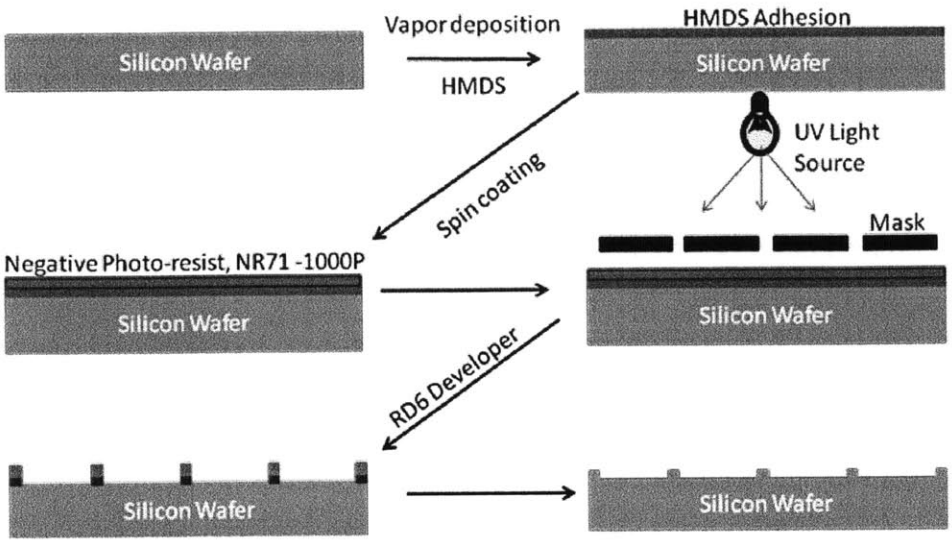

Figure 3-1: Photolithography - Deep Reactive Ion Etching Process

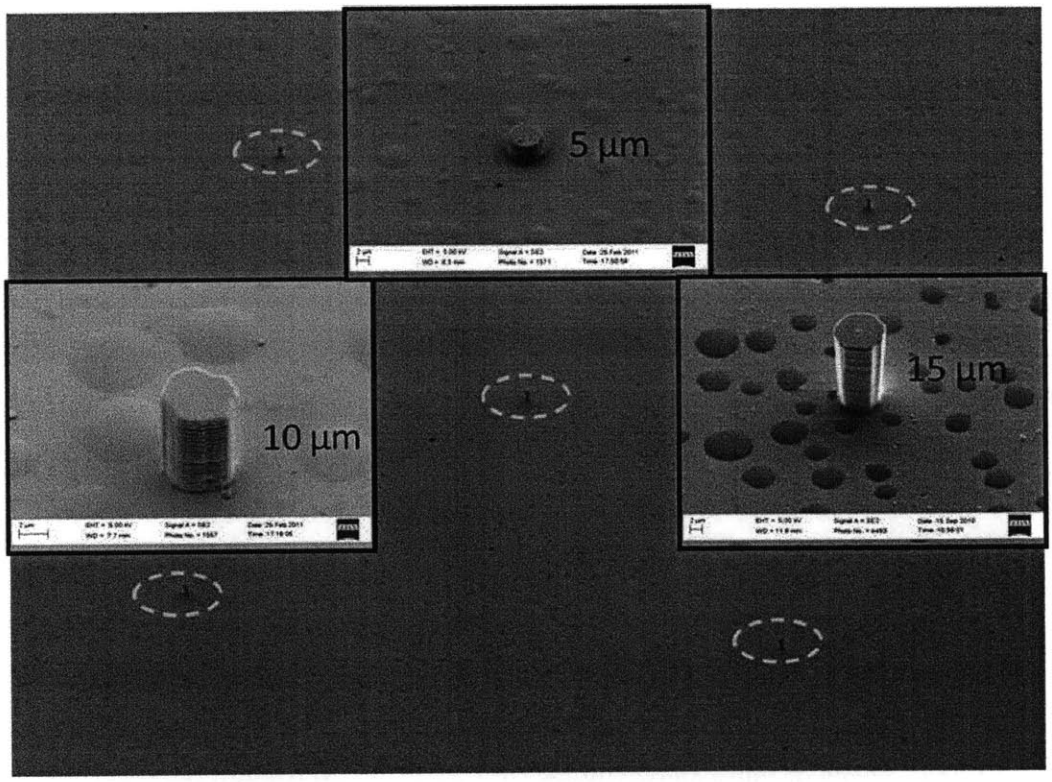

Figure 3-2: SEM Images of Surface With Micron-Size Posts

The surface's intrinsic wettability was controlled by depositing a nano-smooth thin layer of gold (100 nm thick) or silicon oxide (20 nm thick) with a sputtering technique; the resulting contact angles for de-ionized water droplets were found to be 83° on the gold surface and 19° on the

silicon oxide surface. Note that the presence of the micro-posts does not affect wettability (compare insets of Figure 3-3 a, b), which was expected given the large pitch of the post array. Finally, to explore the effect of nano-porosity, a thin nano-porous layer (about 600 nm thick) made of silicon oxide nanoparticles (20 nm and 50 nm) was deposited using the layer-by-layer (LBL) coating process described by Lee et al. [68]. This surface with nanoporous silicon oxide particles is denoted here as LBL. The nano-porous layer caused a further enhancement in the wettability (the apparent contact angle decreases to ~0°, as shown in Figure 3-3d) with respect to the smooth silicon oxide surface (19°). This is due to the well-known Wenzel effect [69]. On the other hand, the roughness height change due to the nano-porous layer was negligible (≤ 0.016 μm). In summary, surface roughness (post height), wettability and nano-porosity were controlled independently using a combination of spaced-out micro-posts, and smooth and nano-porous layers.

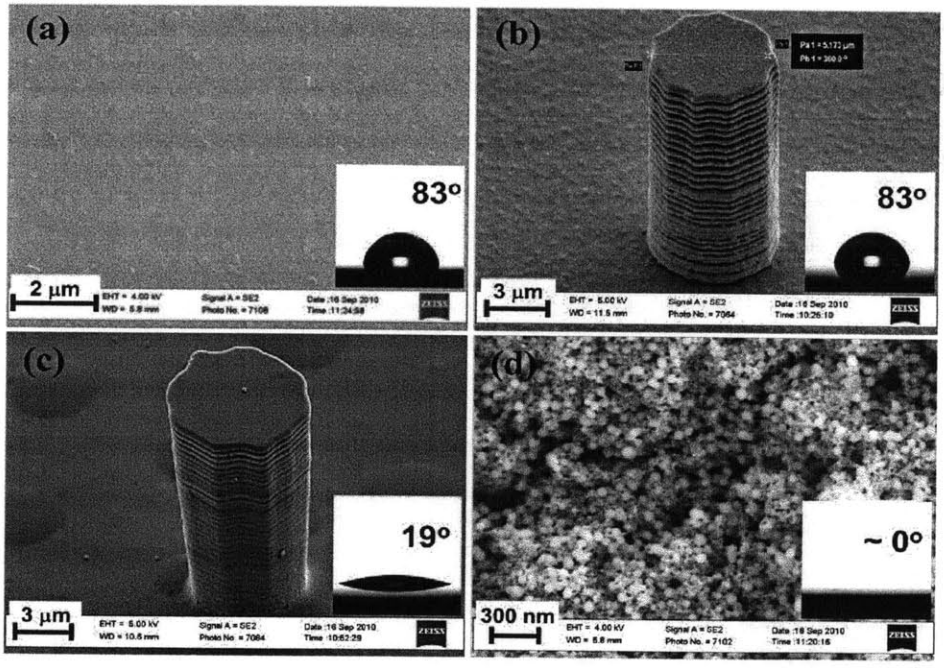

Figure 3-3: SEM images of fabricated samples for LFP tests: (a) smooth Au layer; (b) 15 μm posts on smooth Au layer; (c) 15 μm posts on smooth SiO_2 layer; (d) layer-by-layer (LBL) SiO_2 layer. Insets show static contact angle on the fabricated samples for 10-μL water droplets on (a) smooth Au (83°), (b) Au with micro-posts (83°), (c) SiO_2 layer (19°), (d) nanoporous SiO_2 layer (~0°).

3.2.2 Measurement of LFP

A technique to determine LFP is to measure evaporation time of a liquid droplet over a heated surface. The temperature with longest evaporation time is LFP. The schematic of the experimental facility is shown in Figure 3-4. The silicon wafer was sandwiched between two copper heater blocks (5cmx5cmx1.5cm dimensions). Four cartridge heaters were embedded in each copper heater block. The power to the cartridge heaters were supplied using a variable DC power supply. The upper block had a through-hole in the shape of an inverted cone to place a droplet on the silicon wafer and keep the evaporating droplet on the silicon wafer. The temperature difference between the two blocks was controlled to be within 1 °C difference during the experiments. A water droplet of ~2.9 mm in diameter was released on the test surface from a height of 1.5 mm using a syringe, and the evaporation time was measured with a stopwatch. The uncertainty in the evaporation time measurement was found to be ~0.4 sec from a set of tests at representative conditions. The temperature measurement uncertainty was within ±1 °C during evaporation of a droplet.

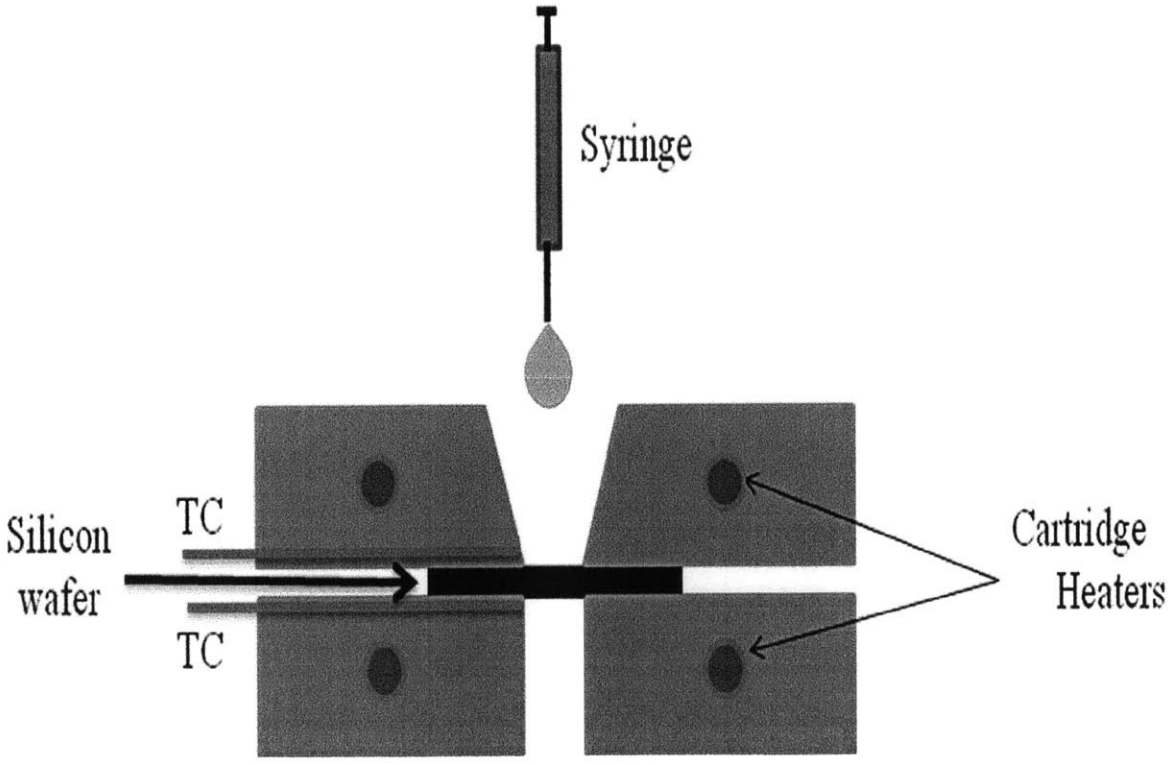

Figure 3-4: Schematic of Quenching Facility to Measure LFP

3.3 Results

Figure 3-5 shows the evaporation time versus temperature for smooth surfaces (no post) and those with 15 μm high posts. The surface finishes include gold, SiO_2 and LBL coating layers. The point with longest evaporation time is the LFP. The LFP of a smooth gold surface was approximately 264 °C, which is similar to what has been reported in the literature [70]. With the presence of the 15 μm high posts on the smooth gold surface, the LFP went up to 290°C. The smooth surface with a SiO_2 layer, which enhanced wettability, had LFP around 274 °C. Finally, the LBL on the smooth surface helped to enhance LFP most significantly, by almost 100°C. While 15 μm-high posts with SiO_2 layer had LFP similar to the smooth SiO_2 layer, the presence of 15 μm posts with the LBL layer enhanced the LFP even further than the smooth LBL surface. In short, increase in surface roughness, wettability and presence of nano-porosity all helped raise the LFP. However, the existence of the 15 μm posts helped intensify the effect on LFP for only the surface with LBL coating.

Figure 3-6, Figure 3-7 and Figure 3-8 show the effect of the surface roughness (micro post height) on LFP for the gold, SiO_2 coating layer and porous silicon oxide surfaces, respectively. Everything else being equal, the presence of the posts enhanced the LFP for all three surfaces. The magnitude of enhancement was largest for the LBL nanoporous surface. The combination of micron size post and nanoporous layer seemed to be the optimal surface for enhancing the LFP, with value as high as 453°C. Note that the reported nominal temperature here is that of the test surface. The local temperature at the liquid-solid contact must be less than the critical point of 374 °C for water. Table 3-1 lists the summary of LFP results for all surfaces.

Table 3-1: Summary of LFP of Water for Tested Surfaces (°C)

Micro post height	Au (°C)	SiO_2 (°C)	Nano-porous SiO_2 (°C)
0 μm	264±5	274±5	359±5
5 μm	295±5	330±5	410±5
10 μm	295±5	330±5	440±5
15 μm	290±5	325±5	453±5

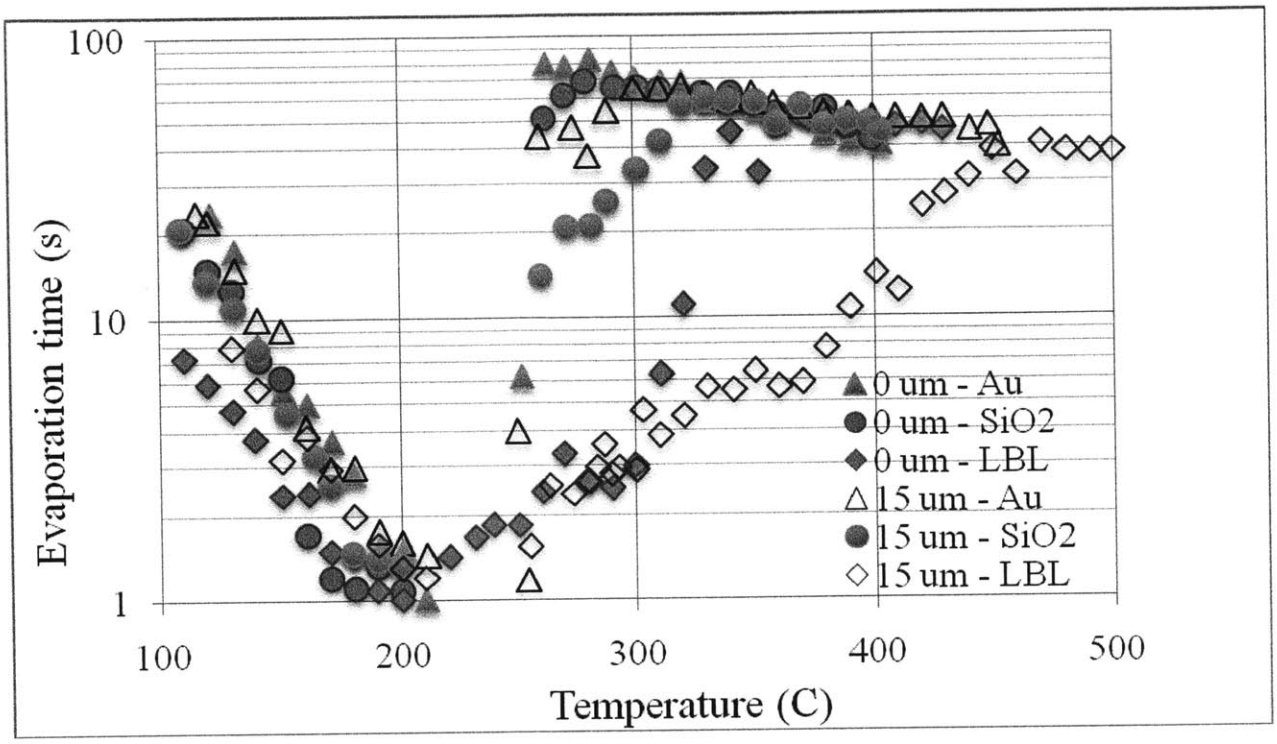

Figure 3-5: Water droplet evaporation time vs. surface temperature. The nominal uncertainty in the measurement of the LFP temperature was found to be less than ±5°C.

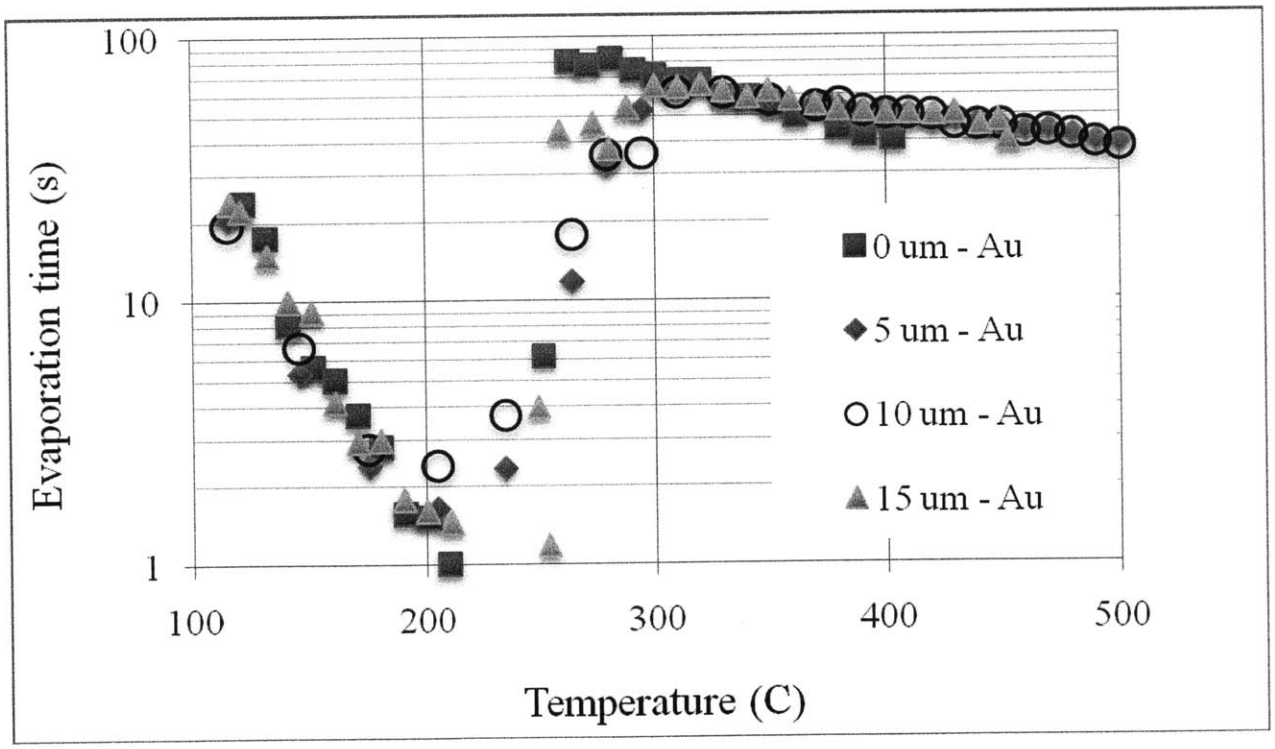

Figure 3-6: Effect of Surface Roughness on LFP of Au Coated Surfaces.

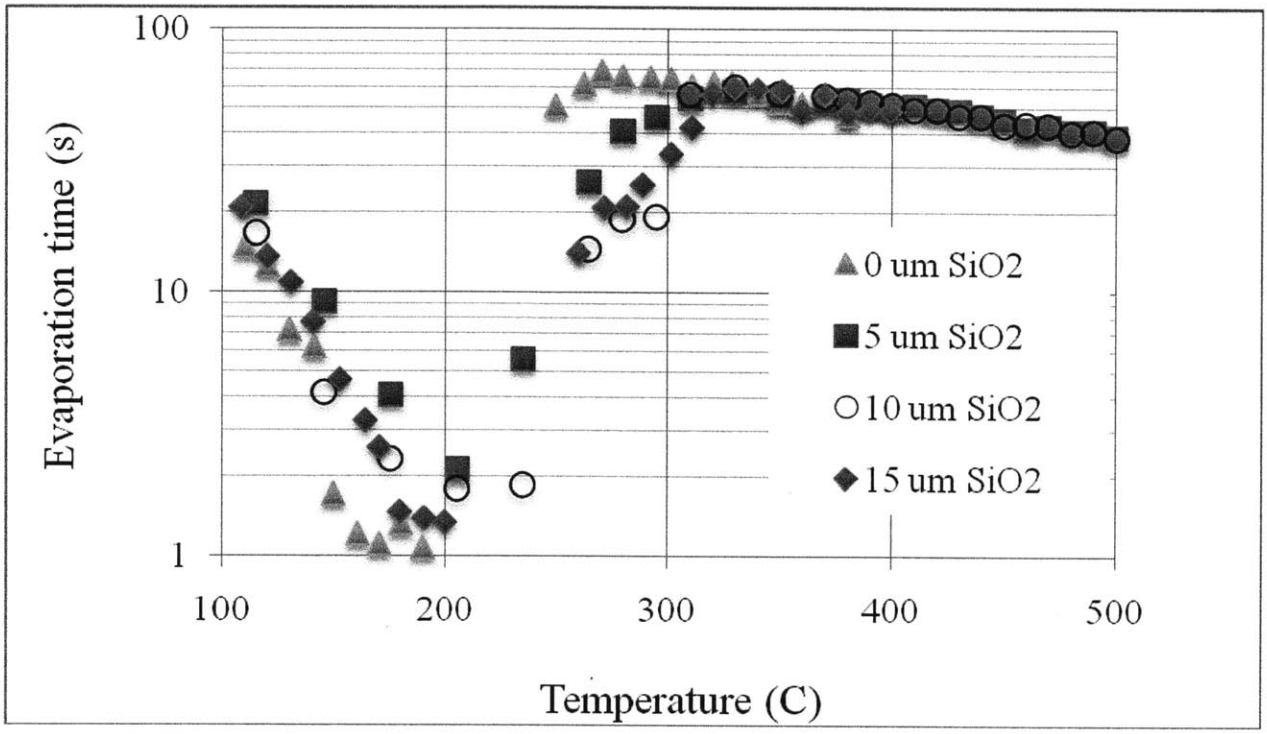

Figure 3-7: Effect of Roughness on LFP of Smooth SiO_2 Coated Surfaces.

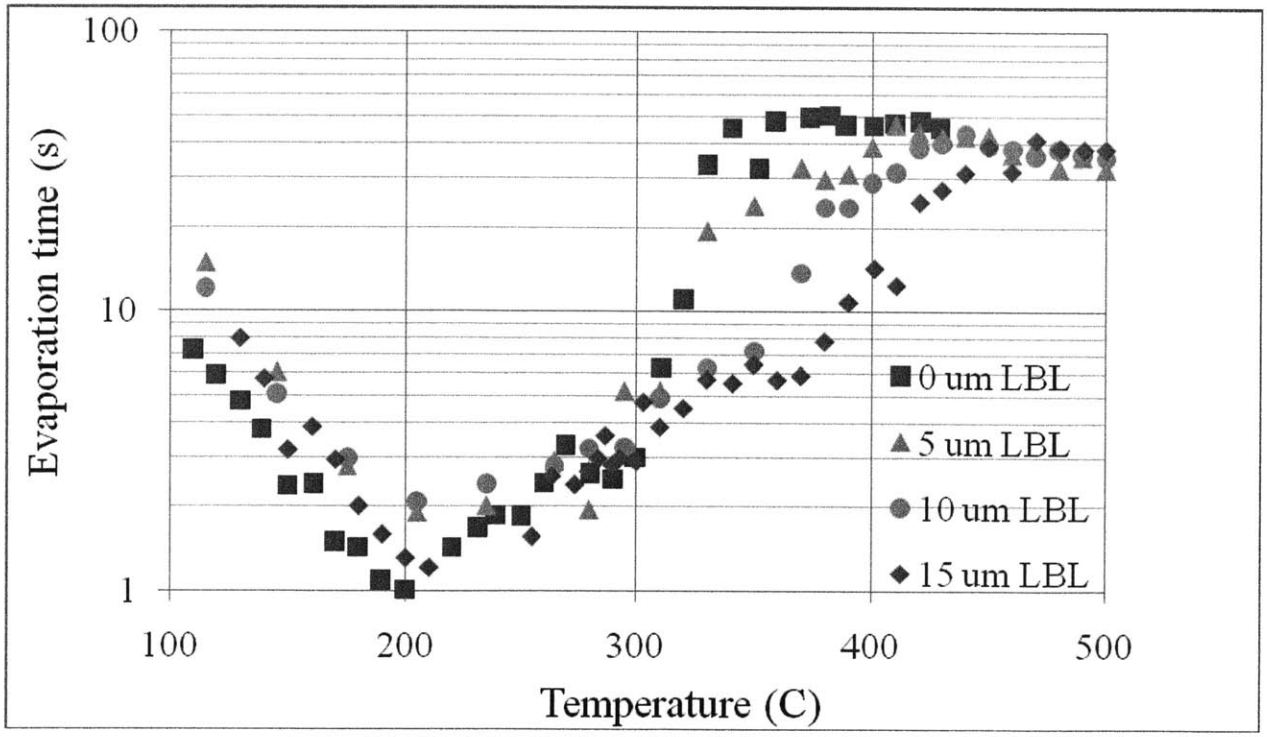

Figure 3-8: Effect of Roughness on Surface with Nanoporous SiO_2 (LBL) Coating.

3.4 Data Interpretation

Why do nano-porosity and micro-posts result in such a high LFP (Table 3-1)? As suggested by previous researchers [71], high-speed imaging of the evaporating droplets, shed light on the mechanisms, when it is focused on the intermittent solid-liquid contacts in film boiling. Thin liquid filaments intermittently connecting the droplet to the solid surface on the samples with micro-posts were observed (Figure 3-9b), whereas the filaments were not observed on the surfaces without micro-posts (Figure 3-9a). However, even in the presence of liquid filaments, the evaporation process was quite different depending on whether the surface was nanoporous or not. The gold and silicon oxide surfaces without nano-porosity stably sustained the liquid filaments, typically for a few milliseconds, without triggering any perturbation (Figure 3-9b and c). By contrast, the nano-porous surfaces instantaneously reacted to the filament contacts with violent splashes of tiny droplets around the large evaporating droplet (Figure 3-9d). This splashing severely disturbed the liquid-vapor interface and prevented the establishment of a stable vapor film at nominal surface temperatures as high as ~453°C.

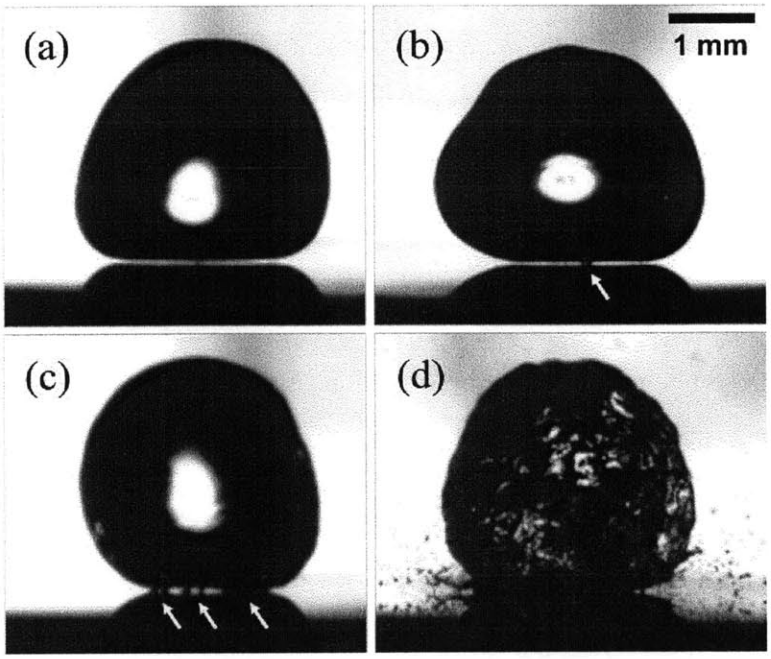

Figure 3-9: Photographs of evaporating water droplets on test surfaces held at 400°C: (a) Au without posts; (b) Au with 15 μm posts; (c) SiO_2 with 15 μm posts; (d) nanoporous SiO_2 layer with 15 μm posts. Arrows show location of droplet-to-surface bridging by liquid filaments.

Biance et al. [72] derived an analytical solution for the film thickness of a stationary evaporating droplet of radius, R, smaller than the capillary length, ($R<a=\sqrt{\frac{\sigma}{(\rho_l-\rho_v)g}}$), for a given surface superheat, ΔT,

$$e = C\left(\frac{k\Delta T\mu\rho g}{h_{fg}\rho_v\sigma^2}\right)^{1/3} \tag{3-1}$$

where C, σ, k, μ, ρ, ρ_v, and h_{fg} are, respectively, an adjustable coefficient, surface tension, thermal conductivity, dynamic viscosity, density of liquid, density of vapor, and latent heat of evaporation. For an evaporating water droplet of 2R ~ 2.9 mm on a surface of 400 °C (ΔT=300 °C), the initial film thickness is estimated to be approximately 36 μm and then decreases monotonically as $R^{4/3}$. Thus, at 15-μm height, the micro-posts can initiate solid-liquid contacts, as shown in Figure 3-9.

Once the liquid filaments are established, heterogeneous nucleation of bubbles can occur at the contact points, if there are cavities available for nucleation. Bernardin and Mudawar [73]'s heterogeneous nucleation model of the LFP focuses on the surface superheat temperature required to initiate the growth of hemispherical vapor bubbles from the pre-existing surface cavities. The nano-sized pores act as cavities for heterogeneous nucleation of bubbles. The pressure drop across a spherical bubble interface of radius r can be estimated using Young-Laplace equation as

$$P_g - P_f = 2\sigma/r \tag{3-2}$$

In combination with the Clausius-Clapeyron equation, Eq. (3-2) gives the following expression for the temperature required to initiate the nucleation of a hemispherical vapor bubble [74],

$$T_{nucl} = T_{sat}\exp\left(\frac{2\sigma v_{fg}}{rh_{fg}}\right) \tag{3-3}$$

There exists a large difference in temperature for heterogeneous nucleation of bubbles between the nano-porous and non-porous surfaces, i.e. $T_{nano\text{-}porous}$ ~ 218 °C vs $T_{non\text{-}porous}$ ~ 336 °C, where nucleation diameter of 23 nm and 1 nm were assumed, respectively. Therefore, bubbles more easily nucleate on the nano-porous surface and very rapidly grow in the highly superheated liquid. Note that these values of nucleation superheat are much higher than those normally

encountered on engineering surfaces where micro-cavities are present. The calculated value of the heterogeneous nucleation temperature at d = 1 nm is higher than the homogeneous nucleation temperature (~300 °C for water at atmospheric pressure) because the size of the vapor embryos responsible for homogeneous nucleation is on the order of a few nm. Therefore, the fluid nucleates homogeneously before it does so heterogeneously.

Starting from the Rayleigh equation for the inertia-controlled phase of bubble growth, it can be shown that $\Delta P \sim \rho V^2$, where V is the velocity of the expanding vapor interface and ΔP is the value of the pressure difference across the interface at the point of nucleation. For a bubble with a diameter of 23 nm, the estimated velocity, V, is on the order of 10 m/sec. When the vapor phase velocity is greater than the critical velocity of Kelvin-Helmholtz instability, the liquid-vapor interface can be disrupted. For the steam and water at atmospheric pressure, the critical velocity is approximately 8 m/sec [74]. Therefore, the velocity of the expanding vapor interface for the 23 nm-diameter bubble is fast enough to generate the splashes shown in Figure 3-9d.

3.5 Conclusions

Water-droplet Leidenfrost Point (LFP) was determined using custom-fabricated surfaces that separate the effects of surface roughness, wettability and porosity. The results show that increase in surface roughness, wettability and nano-porosity consistently enhances Leidenfrost point of water. Nanoporous structure is an essential feature (not solely high wettability) to enhance Leidenfrost point via destabilization of vapor film, which is caused by heterogeneous nucleation of bubbles. The presence of micron-size posts intensified the effect of nanoporous layer on Leidenfrost point by promoting intermittent liquid-surface contacts. The results here can be used as data for mechanistic modeling of quenching heat transfer phenomena in reactors.

4 Separate Surface Effects on Critical Heat Flux

4.1 Introduction

Results in Chapter 2 and Chapter 3 suggest that surface parameters play an important role in enhancing boiling heat transfer phenomena, especially CHF and quenching Leidenfrost point. The results in Chapter 3 are unique in that separate effect of each surface parameter on quenching LFP is obtained experimentally. While there have been studies of surface parameters in pool boiling CHF, the surface characteristics are not quantified and there has been no study on separate effects of surface parameters on CHF. Usually, when one surface parameter is changed, another property is also altered. For example, when the surface roughness is increased, the contact angle can be affected depending on the intrinsic contact angle. In addition, porous coating can affect both the roughness and/or the wettability of a surface.

As mentioned in Chapter 1, porous coating enhances CHF. However, most of these porous coating used micron-size particles and the coating is relatively thick (order of 10s to 100s of micrometers). This effectively changes all surface parameters including surface roughness, wettability and porosity at the same time. The mechanism for how such thick porous coating layer enhances CHF is still not well understood. Therefore, it is necessary to perform a study on separate effects of surface parameters on CHF.

4.2 Experiments

4.2.1 CHF Experimental Matrix and Facility Design Considerations

The objective for this series of experiments is to study the parametric effects of surface parameters on CHF in pool boiling condition. The parameters of interest include porosity and surface roughness. A comparison of different choices for fluids, and description for CHF experimental facility design for the most simple and effective experimental program are presented below. The heater used here will be silicon wafer and the technique to modify the surface is similar to that in the quenching experiments. Silicon wafers have nano-smooth surface finish, which makes it convenient to characterize any additional structure added to the surface. Also, the technique to create micro/nano features on a silicon wafer is well known.

4.2.1.1 Experimental Matrix

The CHF experimental matrix is listed in Table 4-1. Batch 1 experiments is the base case. The objective here is to measure CHF of a nano smooth surface (average roughness less than 0.1 μm). The contact angle of this base surface should be as close to 0° as possible so the wettability remains same in all tests and is independent of porosity and surface roughness. This can be achieved by either modifying the surface with a smooth super hydrophilic coating or using a well-wetting liquid such as a refrigerant. The average CHF value of three tests will be used in the data comparison and analysis, providing they are within the experimental error bound.

The next batch of experiments (batch 2) will focus on the effect of nanoporosity. In batch 2, mono-dispersed SiO_2 nanoparticles is used in the layer-by-layer coating to create a nano-porous layer on the silicon wafer. Batches 3 and 4 are used to study the effect of roughness. The surface roughness is controlled by creating micro-posts of different heights on the base surface. The contact angle of water should not change if the posts are spaced far enough apart as shown in Chapter 3. For well wetting fluid, the posts should not affect the wettability. Finally, batches 5 and 6 are aimed to test the combined effect of roughness and nano-porosity.

Table 4-1 : Desired CHF Experimental Matrix

Parameter	Batch	Contact Angle (°)	Roughness -Rz - Ra (μm)	Layers of SiO_2 LBL coating
Base case	1	<20	Rz <0.1, Ra <0.1	0
Porosity	2	<20	Rz<1.0, Ra <0.1	25
Surface Roughness	3	<20	Rz >1, Ra < 1	0
	4	<20	Rz >1, Ra > 1	0
Porosity and Roughness	5	<20	Rz >1, Ra < 1	25
	6	<20	Rz >1, Ra > 1	25

Note: Contact angle and roughness values are desired. Surface characterizations will provide the actual values.

4.2.1.2 Test Fluid

The two types of fluid considered for the pool boiling CHF tests are water and refrigerant. Table 4-2 compares the different properties for water and two selected refrigerants. From the CHF matrix and the properties of the fluids, it seems that refrigerants are better candidates due to the following reasons: 1) the heat flux required for refrigerants will be much less because of the low

heat of evaporation, 2) lower saturation temperature will reduce heat-up time for each experiment; 3) the low surface tension of refrigerant should lead to small intrinsic contact angle on silicon and hence the effect of porosity and roughness on wettability will be negligible. It could be hard to increase contact angle of refrigerant on any surface if the study of wettability effect on CHF is desired at a later stage. However, in this study, it has been decided that wettability will not be considered since its effect on CHF is well known. This is because it is hard to change the surface wettability alone for FC-72, a well wetting fluid, without changing other surface parameters at the same time. Surfaces, known as superoleophobic surface, can increase contact angle of well-wetting fluids. However, these surfaces usually are not smooth since the superoleophobic surfaces require change in both surface chemistry, porosity and roughness [75, 76, 77].

Table 4-2 : Comparison of Water and Refrigerants for CHF Experiments

Parameter	**Water**	**R-113**	**FC-72***
Availability	Yes	Limited	3M
Latent heat of Evaporation (kJ/kg)	2256.51	144.28	94.9
Surface Tension (N/m)	0.0589	0.01471	0.0081
Saturation Temperature (C)	100	47.48	56.4
Liquid Density (kg/m^3)	958.4	1508.4	1602
Vapor density (kg/m^3)	0.5982	7.4021	13.24
Liquid thermal conductivity (W/m-C)	0.679	0.0637	0.054
Heat capacity (J/kg)	4215.7	940.03	1103
Liquid viscosity (kg/m-s)	281.74E-6	490.97E-6	425E-6
Contact angle on silicon	High (~80 °)	Low(<20°)	Low(<20°)
Estimated CHF by Zuber Corr. [74] (MW/m^2)	1.11	0.20	0.15
Power need - kW (assuming 50% heat loss and maximum 150% CHF enhancement) - 1" diameter disk	2.41	0.54	0.38
T_w at CHF using Roshenow Corr. [74] (C)	128.6	69.3	72.43

* Properties data from El-Genk and Parker [78]

4.2.1.3 Heater Assembly Design Consideration:

For pool boiling CHF, two main types of heating methods were adopted in other studies: resistive (Joule) heating and conductive heating. Each set up has its own advantages and disadvantages as shown in Table 4-3.

Table 4-3: Comparison of Resistive and Conductive Heating Set Up

Parameter	Resistive Heating	Conductive Heating
Heater Surface Material	Metal or conductive coating on non-metal surface	Metal and/or Silicon Wafer
Heater Burn-out	Usually happens, can cause loss of fluid	Does not usually happen since it is temperature controlled
Insulation	Needs bottom insulation if heater is submerged in liquid	Only needs side insulation
Bottom/side insulation	Seal between heater assembly and bath outer structure is usually not needed since heater is completely submerged in pool	Need to have sealing between heater assembly and liquid bath in outer structure
Heat Loss	Low	Can be high
Heater Temp. Measurement	Not accurate (depending on temperature resistivity coefficient)	Accurate
Heater geometry	Usually strip	Can be square or circle
Heater surface modification and characterization	Harder and less accurate to do on metal.	Silicon wafer can be fabricated easily in micro/nano scale
Construction	Initial construction is easy but good insulation at heater bottom can be hard for every experiment. Attaching heater to electrodes are straight forward for metal heaters. For non-conductive heater with metal thin film, attachment to electrode can be problematic	Initial design/construction requires more time but insulation is fixed once it is built. Attaching heater to heater block may require thermal glue but no bottom insulation is needed.
Equilibrium Time	Fast	Slow due to heat capacity of heater block
Experimental Repeatability	Can fluctuate due to inconsistent bottom insulation and/or electrodes attachment.	Usually stable since attachment of surface to heater block only requires thermal glue.

4.2.1.4 Summary

From the comparisons presented above, it was decided that the conductive heater design and refrigerant would be better candidates for this work. The choice for refrigerant is due to lower heat capacity and well-wetting property. This requires much less power for a CHF test. Also, the surface tension of refrigerant is so low that the contact angle will always be small, which makes wettability control not an issue for the study of the effects of porosity and roughness on CHF.

Because the primary focus of this work is to study the surface parameter effects, the surface must be manipulated and controlled easily. This means that silicon wafer as the heater surface is a much better choice than metal. Previous experience in making posts on silicon wafer and putting LBL of Silicon dioxide nanoparticles on silicon wafer can be adopted from the quenching tests. Learning how to do this on a metal surface requires entirely different techniques and equipments, which may not be available. The conduction heater is a better choice for this work. With resistive heater, the silicon wafer will have to be coated with an electrically conductive layer (such as gold). Attaching the electrodes to the gold layer will vary from experiment to experiment, which can cause inconsistent results. The burn-out of the heater every test can cause a hazard (hot liquid pouring out upon burn-out of silicon wafer) during the test. The amount of voltage required to push the current through the layer of gold can be too high. Conduction heater will take slightly more time to design and build initially. Once the facility is built, attachment of the silicon wafer to the heat block can be achieved easily with thermally conductive glue.

4.2.2 Experimental Facility, Procedure and Uncertainty Analysis

4.2.2.1 Facility

The pool boiling CHF is shown in Figure 4-1. The facility consists of a cylindrical GE Type 214 LD Quartz Tubing (6" long, 115 mm ID, 127.7 mm OD, National Scientific Company) sandwiched between two Teflon bases (6" by 6" by 1"). Viton gaskets were inserted between the glass tube and Teflon base as sealing. Compression sealing was achieved by four threaded rods at the corners of the Teflon bases. Two immersion cartridge heaters were inserted through the bottom Teflon base such that they located inside the glass tubing to provide an additional heat source to raise the bulk liquid temperature to saturation before each test and kept it there during the test. An Aluminum coil with cold liquid circulation was used as a condenser to reduce evaporation loss during the test and maintaining a constant liquid inventory. Two K-type thermocouples were used to measure the bulk liquid temperature to ensure saturation condition. The heater assembly was attached to the bottom Teflon base using a window frame.

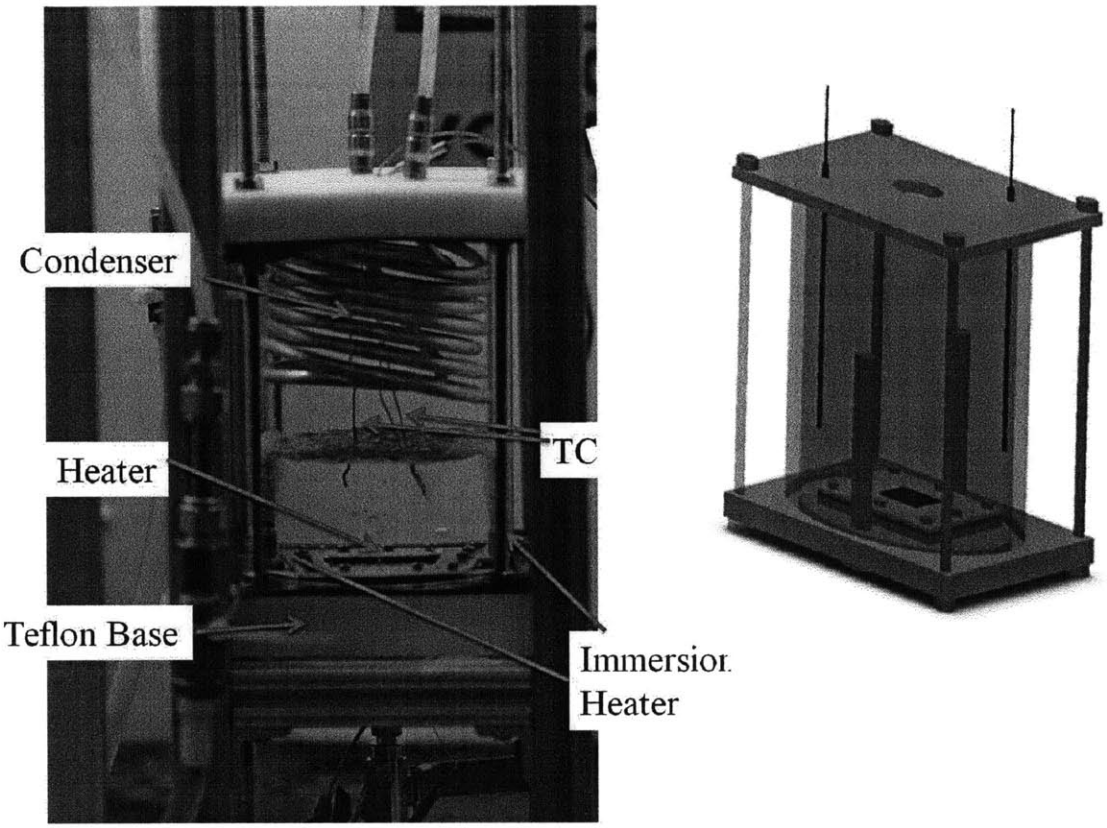

Figure 4-1: Pool Boiling CHF Facility- Left: Photograph of Entire Facility; Right: Schematic

The heater assembly, shown in Figure 4-2, consists of the silicon wafer heater surface of approximately 5 cm x 5 cm, 0.50 mm thick. The silicon was attached to extrusion part of the top copper block using thermal epoxy (Duracol 128) on an area of 2 cm by 2 cm. This was also the heated area since the rest of the top copper block was not in contact with the wafer due to a step of 1.00 mm. To measure surface temperature of the silicon wafer, a K-type thermocouple (0.5mm ID) was inserted in a small groove on the extrusion part of the top copper block. The thermocouple was also held by the same thermally conductive epoxy. Heat was supplied to the wafer using a strip heater (Watlow, WS-CER-1-01-00097), which is rated up to 200W and maximum temperature of 400°C. A K-type thermocouple was also embedded inside the heater to monitor its temperature. The strip heater was sandwiched between the two copper blocks using screws to tighten and ensure good thermal contact. A layer of silver filled paste was applied between the top copper block and the strip heater for good thermal conductivity . The strip heater was positioned such that it located right underneath the heated area. This was done using a groove on the bottom copper lock. A layer of ceramic insulation was added between the strip

heater and the bottom copper block to prevent heat loss. Another thick layer of ceramic insulator (~0.5" thick) was added to the bottom side of the bottom copper block to prevent further heat loss. The viton foam underneath the wafer acted as a seal to prevent liquid leaking out between the wafer and the Teflon base.

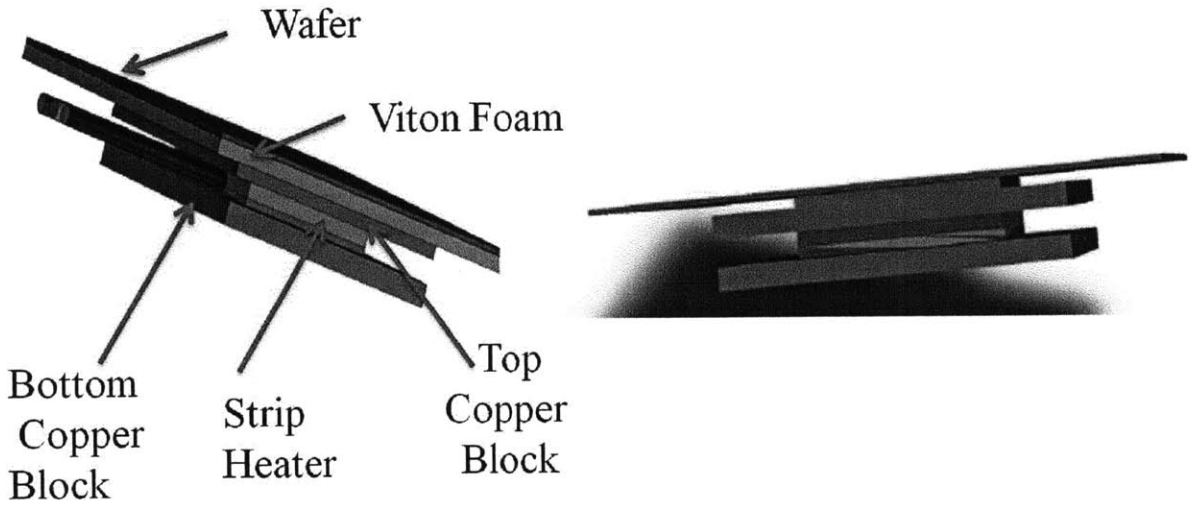

Figure 4-2: Schematic of Heater Assembly - Left: Isometric view; Right: Front View

Power was supplied to the strip heater using a DC power supply (Agilent Technology, N5770A). Voltage measurement was performed at the leads of the strip heaters and current was measured using a shunt resistor (30 A by 100 mV) connected in series with the strip heater. All data were recorded using Agilent Bench Link Data Logger at frequency of 1Hz.

4.2.2.2 CHF Procedure and Uncertainty Analysis

The CHF measurement procedure for FC-72 fluid is described as follows. First, the facility was assembled and leak tested. Subsequently, FC-72 was added to the cell until the liquid covered the immersion cartridge heaters. The liquid was then heated up to saturation using the immersion cartridge heaters with chilled water circulated in the Aluminum coil condenser to reduce FC-72 evaporation loss. After 30 minutes at saturation, a small amount of power was added to the strip heater such that the surface temperature of the silicon was barely above saturation (~ 1 to 2 °C) and stayed relatively constant. This was considered the first steady state point. Subsequently, power was then supplied to the strip heater in constant current steps until CHF occurred, which

was identified by an excursion of the silicon wafer temperature. The wait time between each power step was between 5 and 7 minutes before onset of nucleate boiling (ONB) and about two minutes per each power step after ONB. This was the approximate time for the heater surface temperature to reach steady state conditions (the temperature of the heater surface stayed constant). Typical surface temperature and heat flux histories for a CHF experiment are shown in Figure 4-3. The onset of nucleate boiling (ONB) can be identified by a sharp drop in heater surface temperature. CHF is identified by a sharp increase in heater's surface temperature.

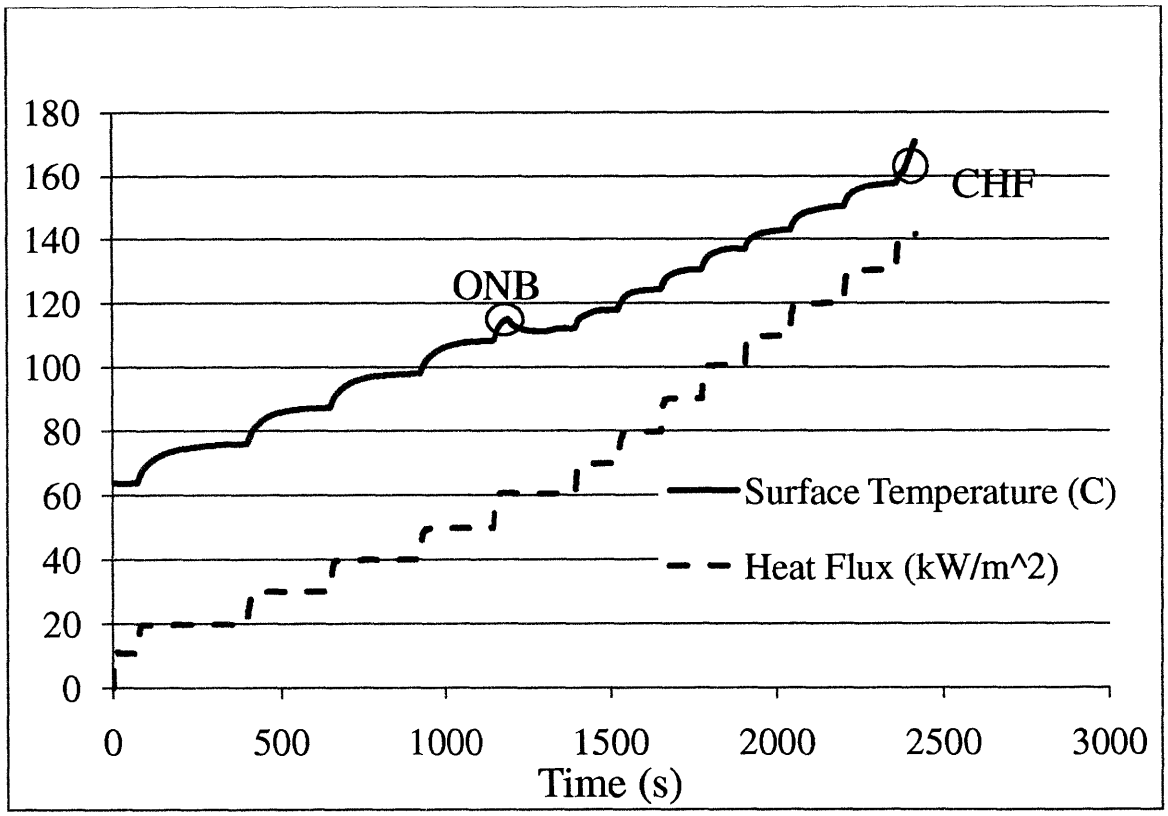

Figure 4-3: Typical Surface Temperature and Heat Flux Profile in CHF Experiment

The heat flux on the surface is calculated as

$$q'' = \frac{IV}{s^2} \tag{4-1}$$

where V and I are the voltage and current, respectively, and s is the side dimension of the square heated surface. The uncertainty in the heat flux is derived from the surface area as well as the measurements for current and voltage. This uncertainty is determined as

$$\frac{U_{q''}}{q''} = \sqrt{\left(\frac{U_I}{I}\right)^2 + \left(\frac{U_V}{V}\right)^2 + \left(\frac{U_s}{s}\right)^2 + \left(\frac{U_s}{s}\right)^2} \quad (4\text{-}2)$$

where U is uncertainty; q'', I, V, D_i, and s are the heat flux, current, voltage, and side of surface, respectively. With the uncertainty of I, V, and area of maximum 1.5%, 1.5%, 5%, respectively, the heat flux uncertainty is of maximum 7.5%.

To calculate the heat transfer to the air (heat loss) for the strip heater, one can use the McAdams [79] correlation for heated horizontal plate facing downward to find the heat transfer coefficient.

$$Nu = 0.82 Ra_L^{\frac{1}{5}} \quad (4\text{-}3)$$

where Nu is the Nusselt number and Ra_L is the Raleigh number. The strip heater temperature was kept below 300 °C to ensure an adequate margin to its temperature limit of 400 °C. This gives the heat transfer coefficient of air from the bottom of the strip heater of approximately 117 W/m^2°C. This is small compared to boiling heat transfer coefficient on order of 20,000 W/m^2°C. The heat loss is less than 1% and can be assumed negligible. Another source of heat loss is due side conduction from the heated part of the silicon wafer to the non-heated part. This non-heated part is exposed to saturated FC-72 on top and air on the bottom. The total area of the four sides for conduction heat loss is about 1/10th of the boiling surface. The boiling heat transfer coefficient is higher than the conduction heat transfer rate. Therefore, the total heat loss due to conduction is small relative to the heat applied to the boiling surface.

The heater surface temperature measurement was done using a K-type thermocouple (0.5 mm diameter) embedded in a small groove on the copper block. The thickness of this groove was 1±.05 mm. The thermocouple was held in place by using conductive ceramic epoxy (Duralco 128), which has thermal conductivity of 4.32 W/m·K. The same thermal epoxy was used to attach the silicon wafer to the top of the copper, and the thickness of the epoxy varied between 100 and 200 μm. Therefore, the thickness of the epoxy layer from the thermocouple to the bottom of the silicon wafer was between 400 and 700 μm, depending on where the thermocouple is located within the groove. The surface temperature of the silicon wafer can be determined as

$$T_s = T_{TC} - k_{epoxy} * t_{epoxy} * q'' - k_{si} * t_{si} * q'' \quad (4\text{-}4)$$

where $T_s, T_{TC}, k_{epoxy}, k_{si} t_{epoxy}$, and t_{si} are the surface temperature, thermocouple temperature, thermal conductivity of epoxy and silicon, and thickness of the epoxy and silicon wafer, respectively. The thermocouple has maximum measurement uncertainty of ±1.1°C. The uncertainty for surface temperature measurement as a function of heat flux is shown in Figure 4-4. Notice that this is the uncertainty from test to test and somewhat conservative. The temperature shift from one test to another is so high due to the fact that the thermal conductivity of the thermal epoxy is low. A difference in thickness of 200 μm (relatively hard to control manually) at heat flux of 150 kW/m^2 can cause a change in temperature drop of about 7°C. Within each CHF test, the thermocouple did not move, which means that the uncertainty of temperature between each heat flux step was the accuracy of the thermocouple of ±1.1°C

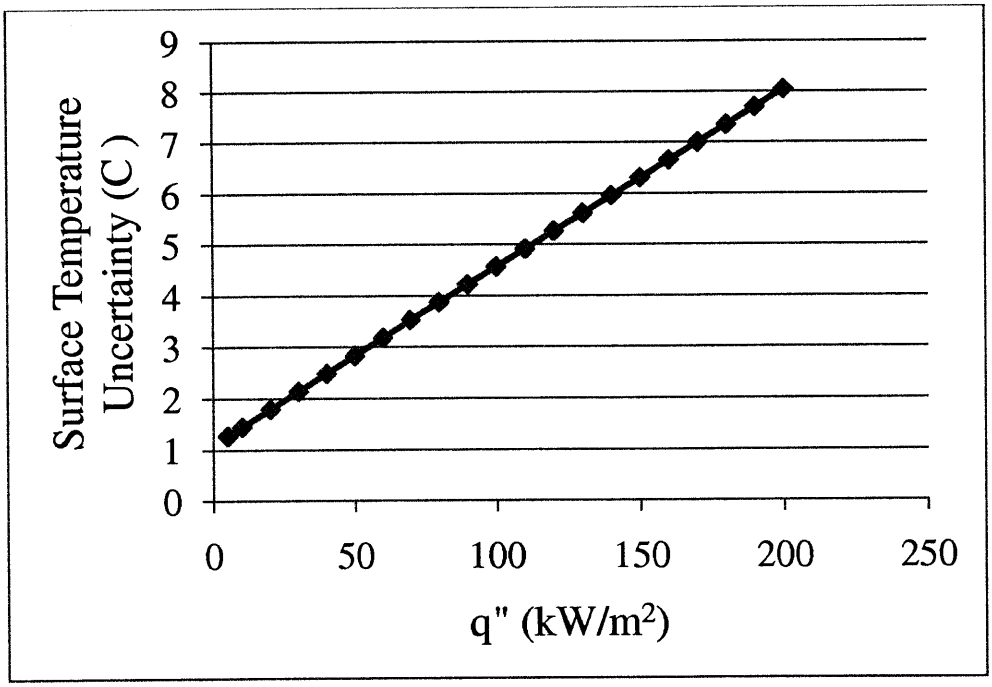

Figure 4-4: Uncertainty in Surface Heater Temperature Measurement From Experiment to Experiment

4.3 CHF Results and Surface Characterization

4.3.1 CHF Results

All experiments were done at FC-72 saturation temperature at atmospheric pressure. The CHF values of FC-72 measured with nano smooth silicon wafers are listed in Table 4-4. Six tests were performed but only two tests had thermocouples embedded underneath the surface for

temperature measurement. All these CHF values were close to each other and the average CHF value for all tests was 150.5 kW/m^2 with standard deviation of 10.8 kW/m^2 . The expected value using the Zuber [80] correlation for a plate, shown in equation (4-5), is approximately 151.5 (kW/m^2). These results verified that the experimental facility performance was consistent with design.

$$q''_{CHF} = 0.131\rho_g^{1/2} h_{fg} \left[g(\rho_f - \rho_g)\sigma \right]^{\frac{1}{4}} \tag{4-5}$$

Table 4-4: Critical Heat Flux of FC-72 for Plain Surface

Test	CHF (kW/m^2) ±7.5%	Note
Plain 1	164.7	New Heater
Plain 2	161.7	Same as test 1
Plain 3	139.8	New Heater
Plain 4	140.4	New Heater
Plain 5	150.4	New Heater
Plain 6	157.3	New Heater
Average	**150.5**	
Standard deviation	**10.8**	

Using the CHF of smooth surface as a comparison baseline, the effect of surface roughness and nanoporosity on CHF can be determined. The surface roughness, which includes *Rz* (maximum height of feature on surface) and *Ra* (RMS average roughness of the surface), was modified by creating an array of posts of 5μm or 200μm in diameter, and approximately 15 μm in height, with pitch of 500μm. The array of posts of 5μm diameter only changed the *Rz*, while the array of posts of 200μm changed both *Rz* and *Ra*. The same photolithography/Reaction Ion Etching technique, used in creating the posts in quenching experiments, was used to create the posts here. To create nanoporosity on the silicon wafer surface, 25 bilayer of SiO_2 nanoparticles (50nm diameter) was applied to the surface using layer-by-layer technique.

The CHF values for FC-72 for surfaces with LBL coating and surfaces with posts are summarized in

Table 4-5 to Table 4-7. Neither increase in surface roughness nor addition of nanoporosity alone seemed to have an effect on FC-72 CHF. The combination of both increase in surface roughness and addition of nanoporosity did not have an effect on CHF of FC-72 either, as shown in Table

4-7. The only surface that showed a minute CHF enhancement is one with 200 μm posts and LBL layers on top. The CHF enhancement here was 17% compared to the plain surfaces. However, taking into account the measurement uncertainty of 7.5% and standard deviation of 5.4% among the three tests, the CHF enhancement could not be determined conclusively.

The value of *Ra*, can be calculated as follows.

$$Ra = \frac{\left(\pi * \frac{D_P^2}{4} * N_P * H_p + Ra_{si} * \left(s^2 - \pi * \frac{D_P^2}{4} * N_P\right)\right)}{s^2} \quad (4\text{-}6)$$

where D_P, N_P, H_P, Ra_{si} and s are respectively the post diameter, the number of posts , the post height, the surface roughness of the smooth silicon and the size of the square heated area. The distance between the posts are 500 μm as expected. There are approximately 1681 posts at pitch of 500 μm in a 2cm by 2 cm heated surface. This gives the average surface roughness, *Ra,* of approximately 2 μm. For the 5 μm posts, the *Ra* value is essentially the same as the smooth silicon wafer surface.

The results here are not surprising, since it has been demonstrated in previous studies that surface wettability is a dominant parameter for pool boiling CHF enhancement. Because FC-72 is a well wetting fluid (small contact angle), the liquid-solid pair is already optimized for CHF. The increased surface roughness and introduction of nanoporosity do not affect contact angle. The results here are important in that they prove the effect of surface roughness and/or nanoporosity alone is negligible on CHF. Table 4-8 summarizes and compares the average CHF values of all the surfaces along with their properties.

Table 4-5 : CHF Values of Surface with 25 LBL layers of SiO_2 nanoparticle

Test	CHF (kW/m^2) ±7.5%
LBL 1	149.6
LBL 2	158.9
LBL 3	139.4
Average	**149.7**
Standard Deviation	**10.0**

Table 4-6: CHF Values of Surface with Posts (500 μm pitch)

Test	CHF (kW/m^2) ±7.5%
5 μm post - Test 1	169.4
5 μm post - Test 2	164.0
5 μm post - Test 3	147.2
Average	**160.2**
Standard Deviation	**11.6**
200 μm post - Test 1	151.4
200 μm post - Test 2	149.9
200 μm post - Test 3	163.3
Average	**154.8**
Standard Deviation	**7.3**

Table 4-7 : Surface with Posts and 25 LBL layers of SiO_2 nanoparticles

Test	CHF (kW/m^2)
5 μm post - LBL 1	174.6
5 μm post - LBL 2	159.0
5 μm post - LBL 3	159.9
Average	**164.5**
Standard Deviation	**8.8**
200 μm post - LBL 1	177.2
200 μm post - LBL 2	176.5
200μm post - LBL 3	160.7
Average	**171.5**
Standard Deviation	**9.3**

Table 4-8 : Summary of Average CHF of FC-72 and surface roughness for All Surfaces

Surface	Rz (μm)	Ra (μm)	LBL (layer)	CHF(kW/m^2) ±7.5%	Standard Deviation (kW/m^2)
Plain	<0.1	<0.1	0	150.5	10.8
LBL	<1.0	<0.1	25	149.7	10.0
5 μm post	~15	<0.1	0	160.2	11.6
200 μm post	~15	~2.0	0	154.8	7.3
5 μm post - LBL	~15	<0.1	25	164.5	8.8
200 μm post - LBL	~15	~2.0	25	171.5	9.3
Note: *Ra* and *Rz* values are expected. The actual measurements will be shown shortly.					

4.3.2 Boiling Curves

Figure 4-5 to Figure 4-9 show the boiling curves of surface with posts and/or LBL coating are compared with those of plain (bare) surfaces. Noticed that the uncertainty in the surface temperature can be as high as 6 to 7 °C at CHF of 150 to 170 kW/m^2 from test to test. Also, the ONB of all surfaces can be identified readily from these boiling curves when there is a large drop in surface temperature at the same heat flux. Overall, the boiling curves are similar among all the tests (within the temperature measurement uncertainty). This means that there was no distinguishable change in the heat transfer coefficient of the different surfaces. Everything else being the same, the heat transfer coefficient usually depends on the number of nucleation sites, which relates to the number of micro cavities. The addition of the posts and/or LBL nanoparticles layers are not expected to create micro cavities, which suggests that there should not be much change in the heat transfer coefficient as observed here.

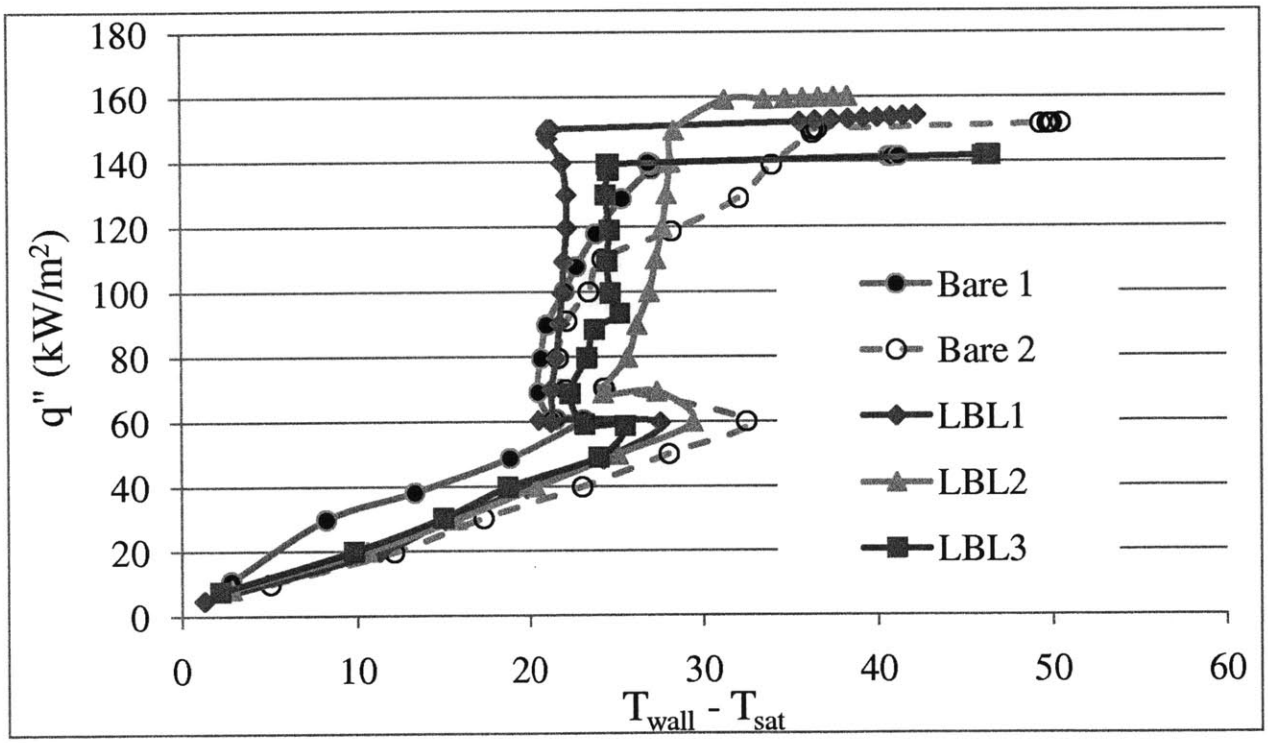

Figure 4-5: Boiling Curves of LBL Coated Surfaces Compared to Plain (Bare) Surfaces

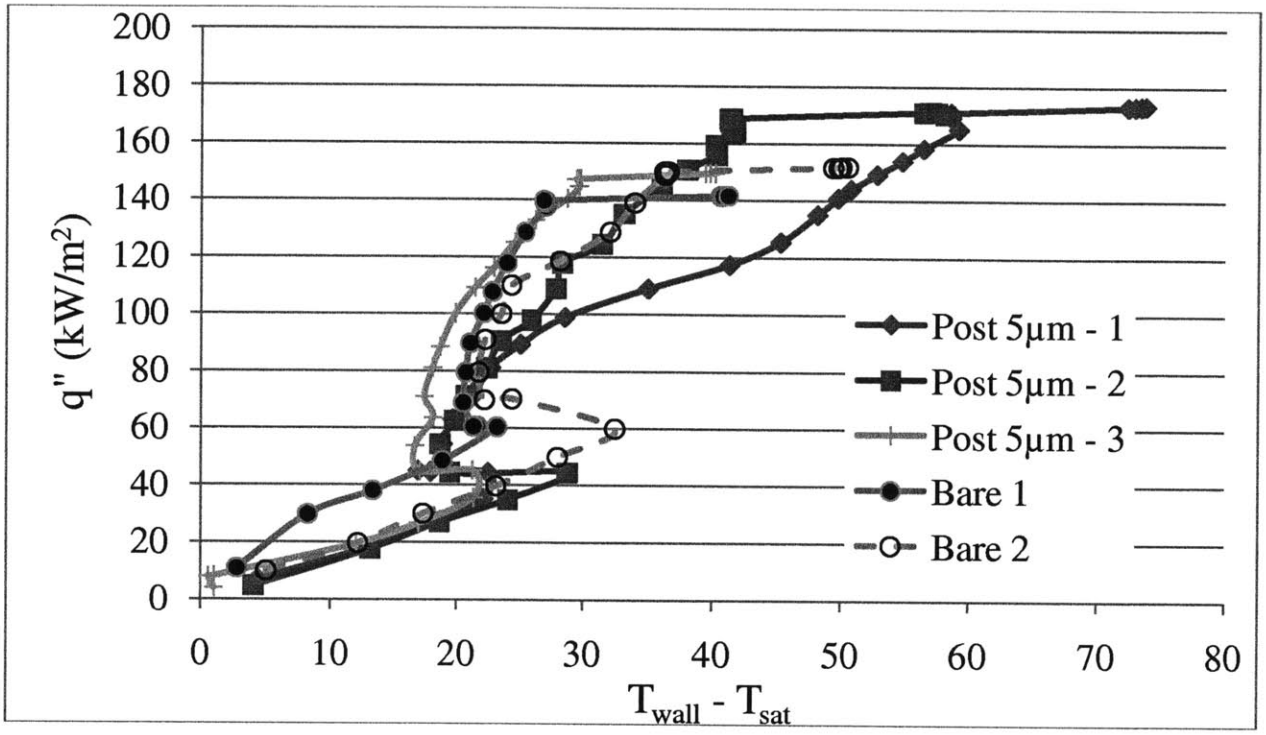

Figure 4-6: Boiling Curves of Surfaces with 5 μm Posts Compared to Plain (Bare) Surfaces

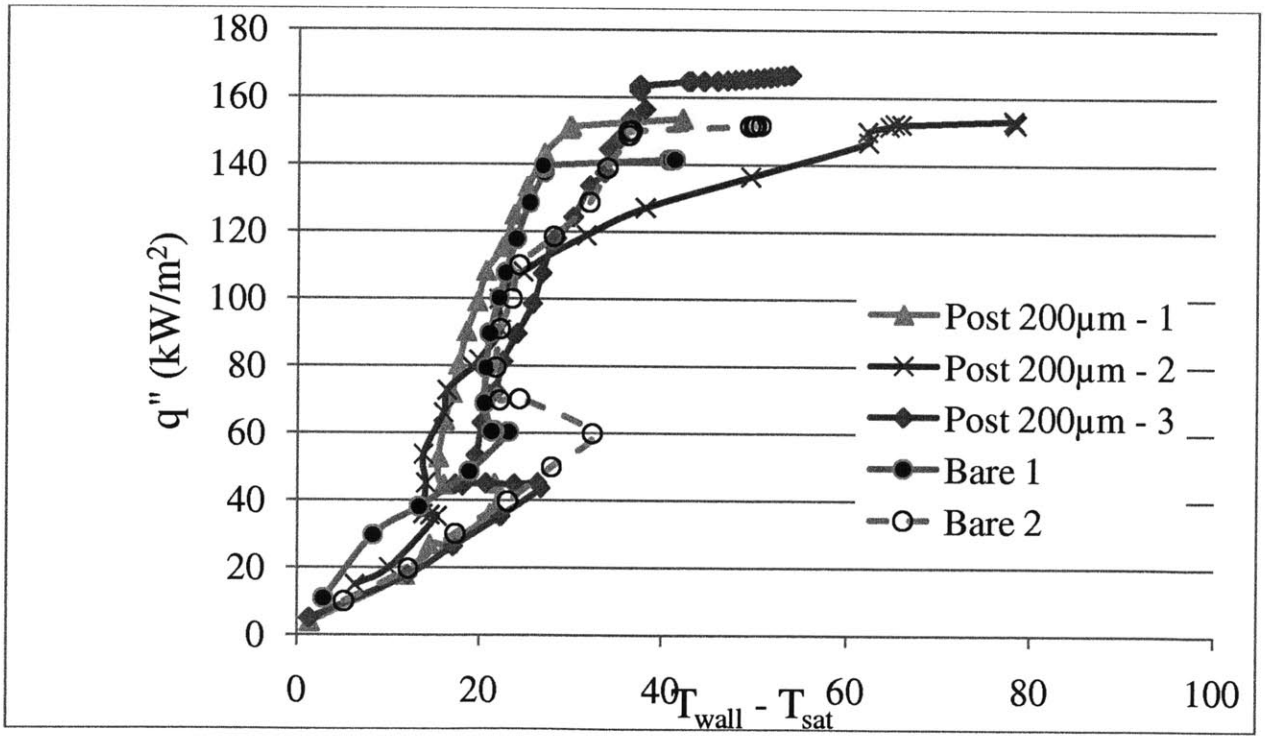

Figure 4-7: Boiling Curves of Surfaces with 200 μm Posts Compared to Plain (Bare) Surfaces

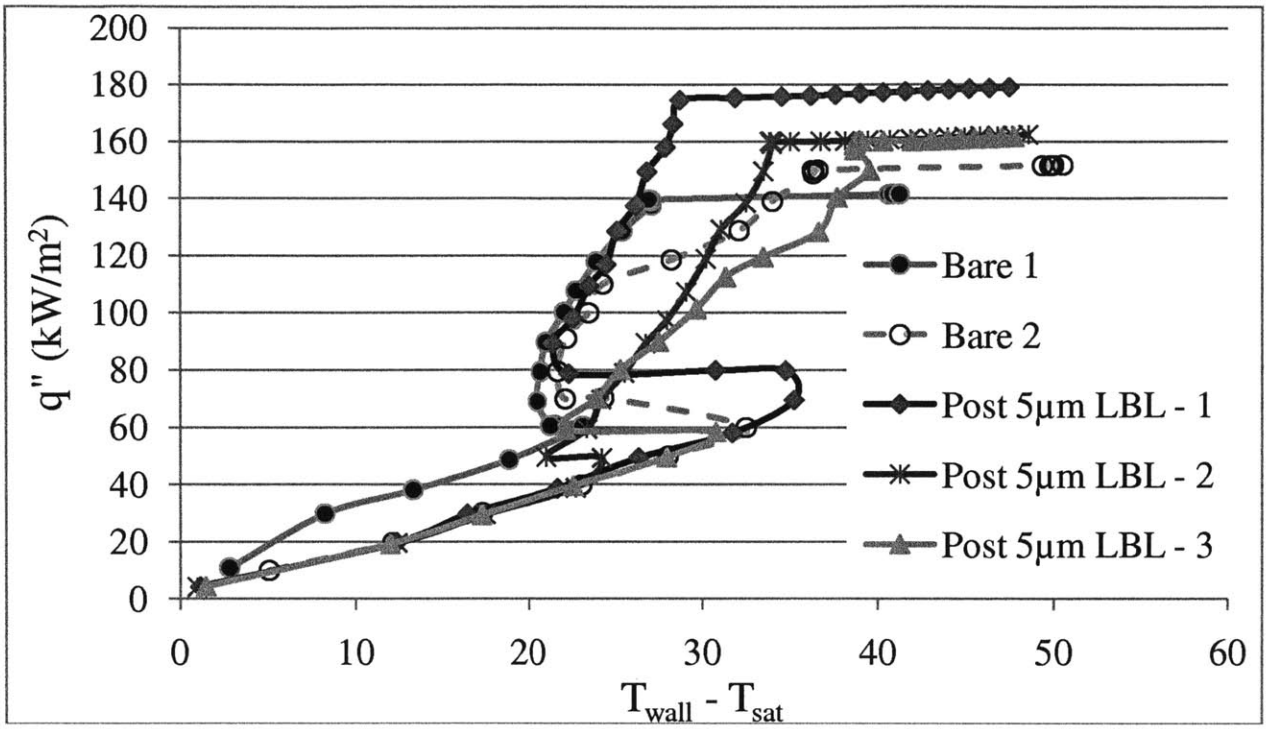

Figure 4-8: Boiling Curves of Surfaces with 5µm Posts and LBL Compared to Plain (Bare) Surfaces

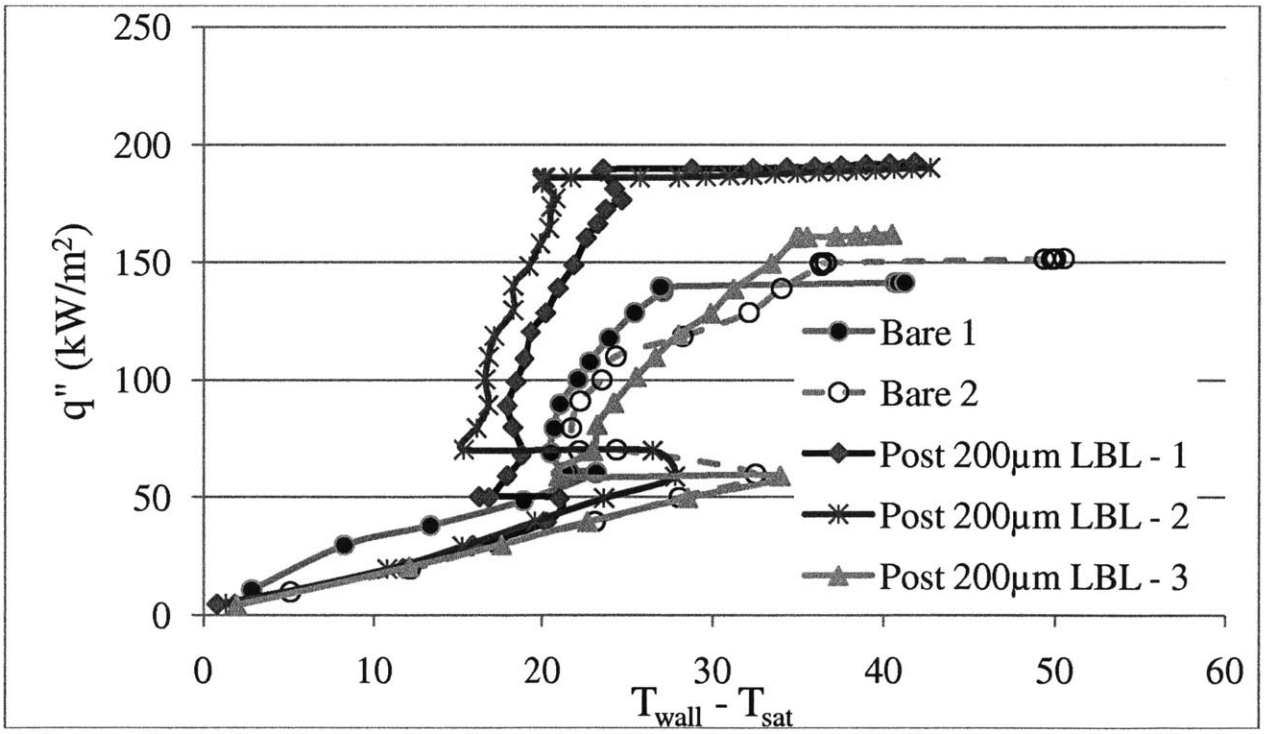

Figure 4-9: Boiling Curves of Surfaces with 200µm Posts and LBL Compared to Plain (Bare) Surfaces

4.4 Surface Characterization

Scanning Electron Microscopy (SEM), contact angle and confocal microscopy were used to characterize the surface. The representative SEM images of surfaces with posts and/or LBL coating are shown in Figure 4-10. The 5μm diameter posts are not perfectly cylindrical due to the imperfection in the mask. However, since the small posts only contribute the *Rz*, the shape of the post is not as important. The 200 μm diameter posts look perfectly circular, which allows calculation of the surface roughness (*Ra*) as already shown in equation (4-5). The SEM images overall confirm that the structures on the tested surfaces are as desired. The LBL on top of the posts can be seen very clearly too. Figure 4-11 shows SEM images of a smooth wafer and one coated with LBL SiO_2 layer at approximately 70K magnification. Their associated EDS spectra are also shown. The nanoparticles layer can be seen clearly and the EDS spectrum confirms the presence of Oxygen and Silicon – main components of the particle materials. For the smooth wafer, no feature can be seen and the EDS spectrum only has one peak for Silicon.

Static contact angle of FC-72 on different surface was also measured and there was no significant change in contact angle from different types of surface. For each surface, contact angle was measured at two different spots. The values are reported in Table 4-9. For all surfaces, the contact angle did not seem to change at all, which confirmed that adding roughness and/or LBL coating did not alter the wettability of FC-72 on the surface. Representative images of contact angle are shown in Figure 4-12 and they all show that FC-72 is indeed a well wetting fluid. The receding contact angle, which is considered important for CHF, is expected to be smaller than static contact angle. Measuring receding contact angle for well wetting fluid is challenging due to high evaporation rate, and also has fairly larger uncertainty. A change in contact angle from less than 15° to 0° is not expected to change CHF at all. The contact angle results here confirm that wettability stayed constant for all tested surfaces.

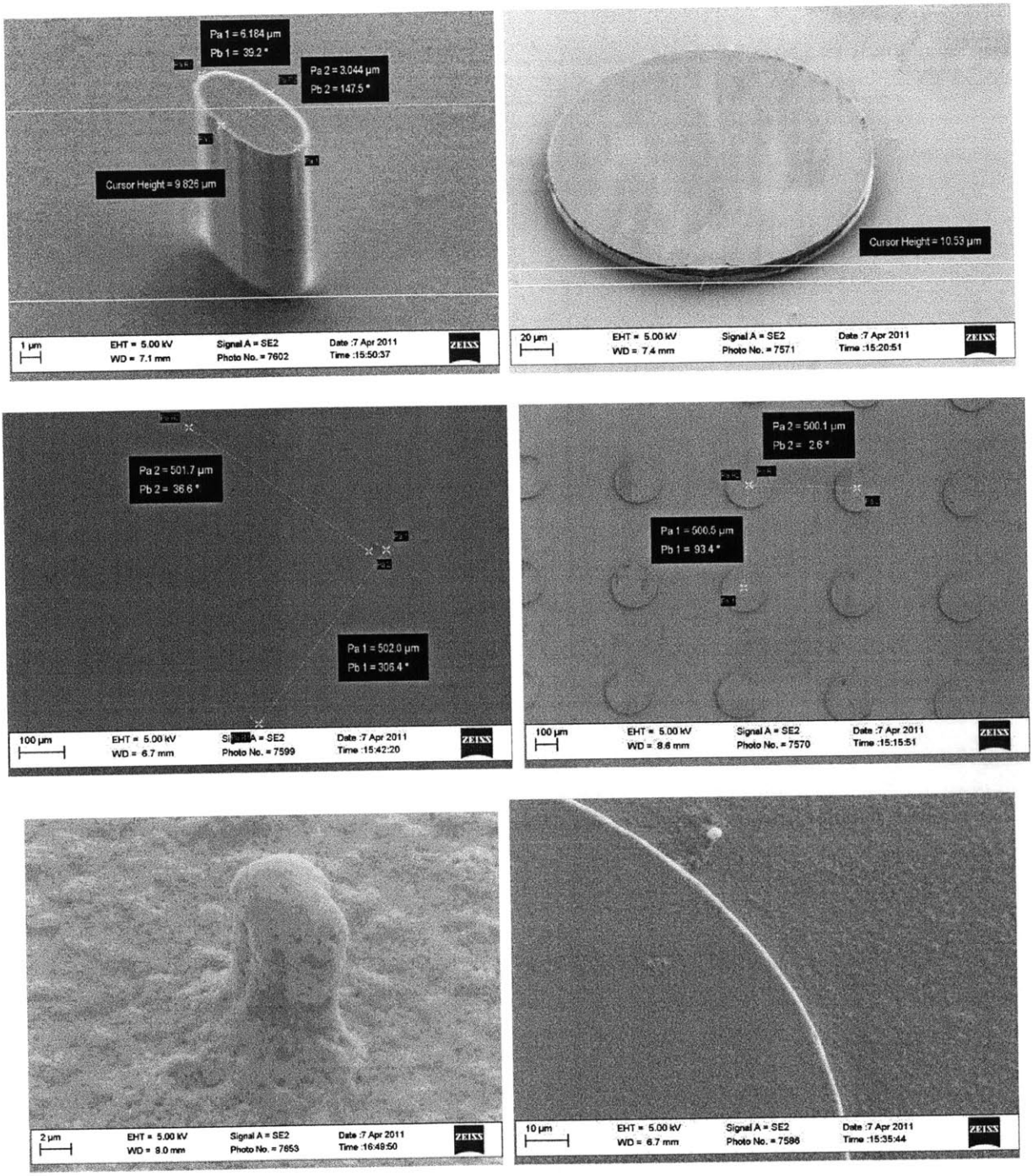

Figure 4-10 : SEM Images of Surface with Posts and LBLB - Left (5 µm); Right (200 µm). Top: Single post (LBL). Center: Array of Posts; Bottom: Single posts with LBL

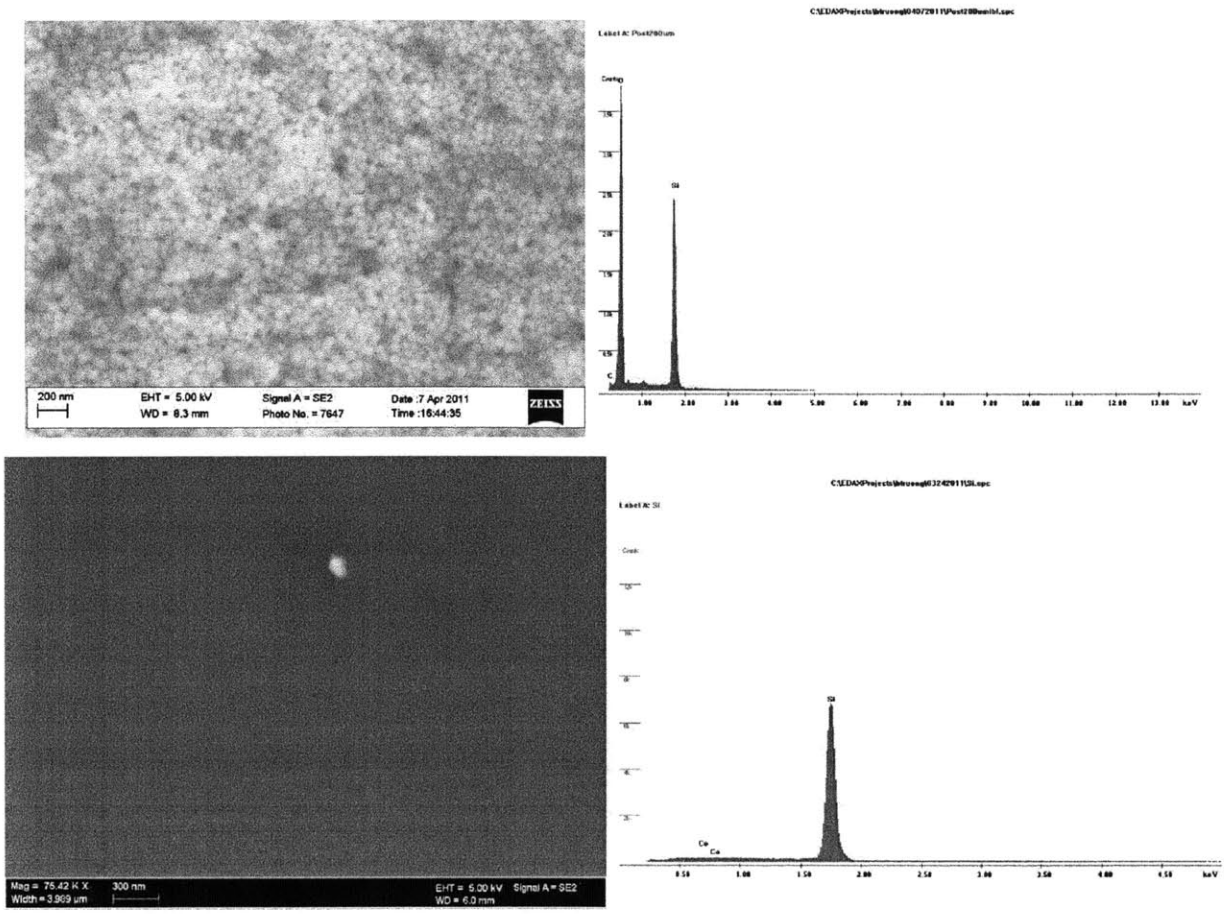

Figure 4-11: SEM of a Smooth Wafer (bottom) and LBL Coated Wafer (top)

Table 4-9: Summary of Contact Angle of FC-72 on Different Surfaces (Uncertainty: ±3°)

Surface	Spot 1 (°)		Spot 2 (°)		Average	Stdev
	Left	Right	Left	Right		
Plain Wafer	15.5	14.1	14.2	13.9	**14.4**	0.7
200 µm post - LBL	14.0	11.3	10.5	12.7	**12.1**	1.5
5 µm post - LBL	11.2	10.7	13.2	13.2	**12.1**	1.3
200 µm post	11.0	12.9	12.0	14.8	**12.7**	1.6
5 µm post	14.4	14.4	13.4	13.4	**13.9**	0.6
25 LBL	10.3	11.2	15.4	16.7	**13.4**	3.1

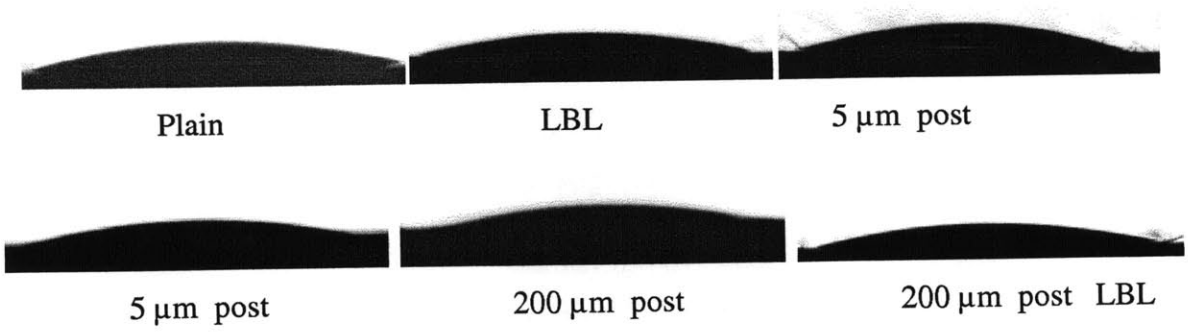

Figure 4-12: Representative Contact Angle Measurement

The surface roughness, *Rz* and *Ra* were measured using Confocal microscopy (Olympus LEXT OLS3000). The results for these measurements are shown in Table 4-10. The *Rz* was measured for all surfaces and are around the expected value. Note that the values *Rz* for posts with LBL layer on top are higher than those of the posts by themselves because the LBL layer creates additional thickness. The *Ra* values and the surface area (projected and actual) were only measured for the plain wafer and the LBL surface. For surface with posts, since the focus was mainly on one post, the value for *Ra* and areas would not be representative of the entire surface. Therefore, these values were calculated using the measured *Rz* for the entire heater surface. Overall, the surface roughness values are within expectations. The 3D Confocal images are shown in Figure 4-13. For the bare wafer, there was a strange drop at one corner. This might be due to noise and the roughness analysis excluded this corner. For the LBL coating one, part of the coating was scratched off to determine the thickness of the coating. The roughness analysis was done at the interface, and the thickness of the coating was approximately 1.02 μm.

Table 4-10: Summary of Confocal Data for Surface Roughness

Surface	Rz (μm) ±0.5 μm	Ra (μm) ±0.05 μm	Projected Area (μm^2)	Actual Area (μm^2)	Area Ratio
Bare	0.25	0.03	67747	68160	1.006
LBL	0.98	0.11	67614	67895	1.004
5 μm post	15.2	0.1*	NA		1.001*
200 μm post	15.4	2.08*			1.025*
5 μm post - LBL	16.9	0.12*			1.001*
200 μm post - LBL	17.6	2.43*			1.030*

*Calculated based on measured *Rz* values for the entire heater surface.

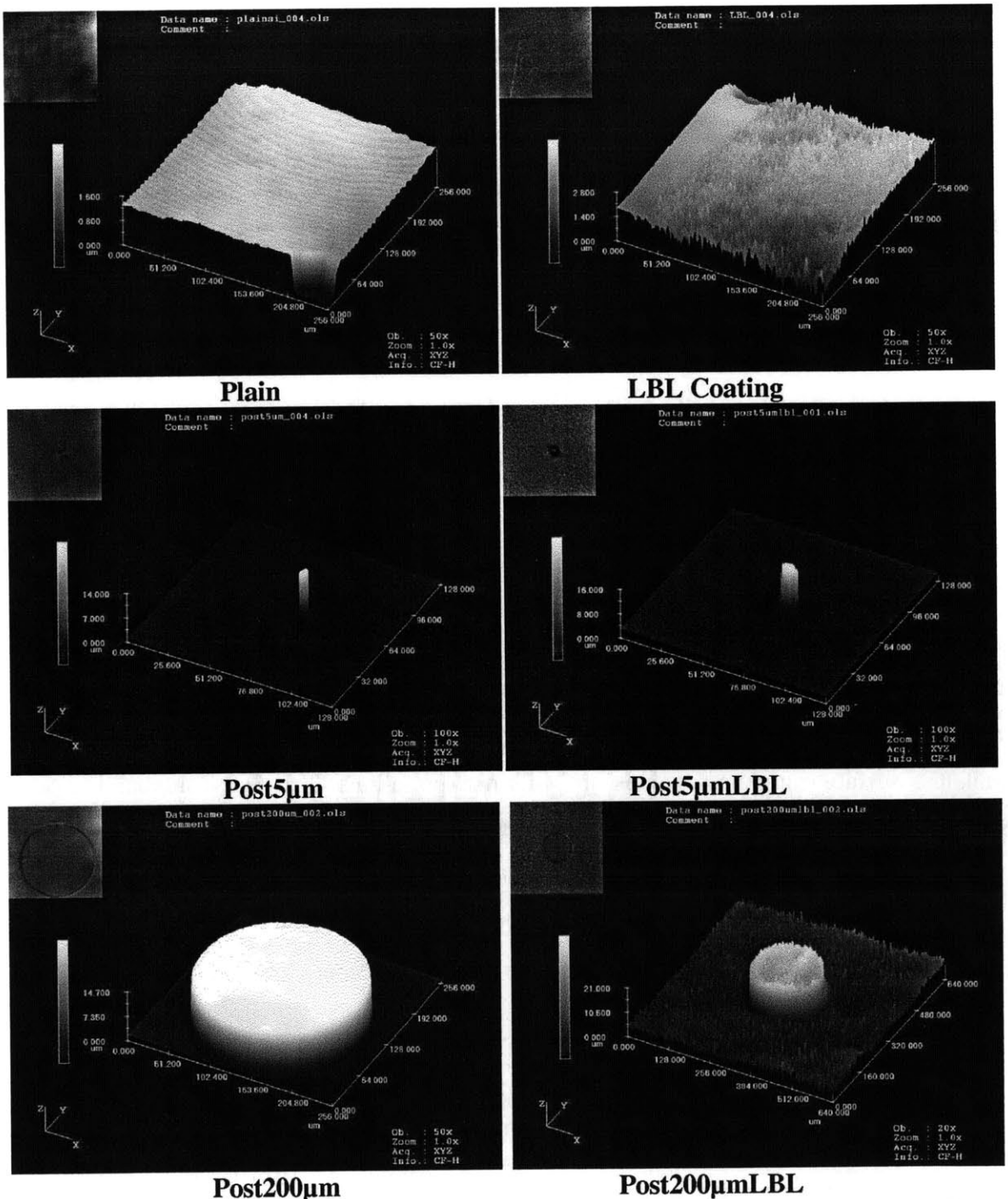

Figure 4-13: Representative Confocal Image for Surface Used in CHF Tests (256 µm x 256 µm)

The surface porosity of the LBL coated surface was measured with a spectroscopic ellipsometer (J.A. Woollam Co., INC model XLS-100 at the Institute for Soldier Nanotechnologies at MIT). This was done with the help of Phillips [81], who previously measured porosity for various LBL coating layer and described the detailed process in his thesis. In this currently study, the LBL

layer has porosity of approximately 40% with uncertainty of at least 5%. The porosity of various LBL coatings in Phillips [81] study ranges from 39% to 59% porosity. The spectroscopic ellipsometer can also provide the thickness of the coating layer, which in this case is 976 nm. The thickness here agrees with the value measured using confocal microscopy.

Another technique attempted to determine the porosity of the surface was using Focus Ion Beam (FIB). In the FIB technique, an ion beam is used to cut a cross-sectional area of a coating layer and then an SEM image is captured. In theory, one can continue using the beam to cut more and more cross-sectional areas and taking their SEM images. At the end, the 2D SEM images can be combined together to recreate a 3D profile of the coating structure to determine porosity. An examples of image of a cross sectional cut is shown in Figure 4-14 (left). The porous structure can be seen the higher magnified image in Figure 4-14 (right). Notice that some of the pores, even though they have diameter of less than 50nm, are filled with smaller particles. These particles come from the ion beam milling process, and can affect the overall porosity measurement. Therefore, this technique was not pursued further here.

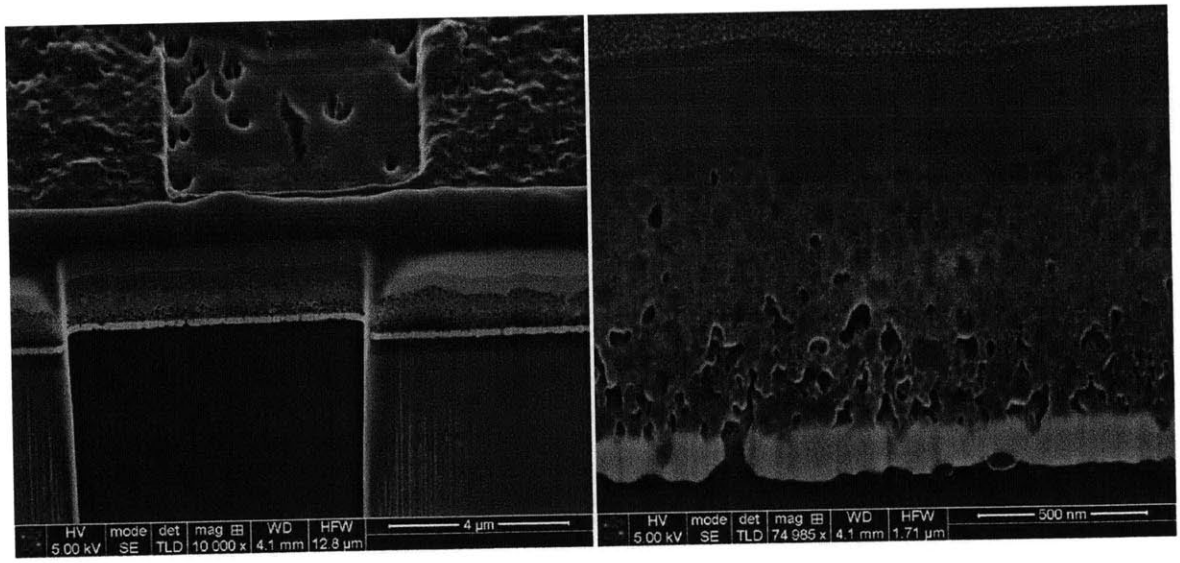

Figure 4-14: FIB Images - Left: Cross Sectional Cut Are; Right: The Porous Structure

4.5 Conclusions

In this chapter, separate surface effects on pool boiling CHF for a well-wetting fluid, FC-72, were determined experimentally using silicon wafer as heater. The surface parameters investigated were nanoporosity and surface roughness. The results were: Nanoporosity and/or increase in surface roughness had no effect on CHF of FC-72, a well-wetting fluid. Simultaneous addition of nanoporosity and increase in surface roughness, in both Rz and Ra, resulted in a minute CHF enhancement (17%) compared to the bare surface. However, such enhancement was not considered significant due to measurement uncertainty of 7.5%. The next chapter will analyze different CHF correlations and models in the literature in order to provide insights and possible explanations for the results obtained here.

5 Analysis of Effect of Surface Parameters on CHF

In Chapter 4, experimental data from of separate surface effect on CHF show that introducing nanoporosity and/or increasing surface roughness (both in *Rz* and *Ra*) had little effect on CHF and heat transfer coefficient of a well-wetting fluid, such as FC-72. However, experimental data reported in literature for microporous coating surface (uniform or modulated) show large enhancement in both heat transfer and CHF for well-wetting fluid. In this chapter, a review of CHF models will be presented first. Then explanation of how each of these surface parameters is taken into account in existing models will be investigated. The analysis will help provide better insights for explanation of the results in Chapter 4. The focus here will be in pool boiling since our separate-effects data are for pool boiling. Therefore, the analysis will focus on the surface parameters while the effect of convection due to flow boiling will not be considered.

5.1 Existing CHF Models

After many years of research on CHF, the exact mechanism of this complex phenomenon is not well understood. While there are many CHF models reported in the literature, most of them fall in one of the following categories: hydrodynamic instability theory, macrolayer dryout theory, microlayer theory, hot/dry spot theory, and bubble interaction theory. A brief description of each of these theory is outlined below before examining effects of surface parameter on CHF.

5.1.1 Hydrodynamic Instability Theory

As one of the earliest attempts to quantify CHF, the hydrodynamic instability theory was proposed by Kutateladze [82] initially, and later incorporated into a formal model by Zuber [80]. It hypothesizes that CHF happens when the interface of the larger vapor columns leaving the heated surface becomes unstable. Helmholtz instability prevents the liquid to penetrate the vapor layer to rewet the surface. At the same time, the vapor jets coalesce into one another and increase the size of the vapor layer covering the heater. The liquid underneath this large vapor blanket will eventually evaporate and cause CHF since there is a lack of liquid on top flowing through the vapor to replenish the evaporated liquid. The CHF can be calculated using energy balance, as refined by Lienhard and Dhir [83]

$$v_g = \frac{q''_{max}}{\rho_v h_{fg}}\left(\frac{A_{surf}}{A_{col}}\right) \tag{5-1}$$

where v_g, A_{surf}, A_{col} and h_{fg} are the critical Helmholtz velocity, the heated surface area, the area of a column of vapor and the heat of evaporation, respectively. The Helmholtz instability is [84]

$$v_g = \sqrt{\frac{2\pi\sigma}{\rho_v \lambda}} \tag{5-2}$$

where σ, λ are the surface tension and the Taylor instability wavelength. The critical wavelength, λ, is defined as [74]

$$\lambda = 2\pi\sqrt{\frac{3\sigma}{(\rho_v - \rho_l)g}} \tag{5-3}$$

The ratio $\left(\frac{A_{surf}}{A_{col}}\right)$ can be approximated

$$\left(\frac{A_{surf}}{A_{col}}\right) = \frac{\lambda_D^2}{\pi\left(\frac{\lambda_D}{4}\right)^2} = \frac{16}{\pi} \tag{5-4}$$

where λ_D is the size of a square unit cell containing four vapor columns of diameter $\frac{\lambda_D}{2}$. Substitution of equation (5-2) to (5-4) into (5-1), an expression for CHF can be obtained

$$q''_{max} = 0.149\rho_v h_{fg}\left[\frac{\sigma(\rho_l - \rho_g)g}{\rho_v^2}\right]^{\frac{1}{4}} \tag{5-5}$$

The constant on the right hand side, in Zuber's original model, is $\frac{\pi}{24} = 0.131$. One of the main criticisms of this model is that the model does not take into account of the heater geometry and/or the surface's condition.

5.1.2 Macrolayer Dryout Theory

The macrolayer dryout theory, proposed by Haramura and Katto [85], considers the formation and evaporation of a liquid macrolayer underneath a larger vapor mushroom as shown in Figure 5-1.

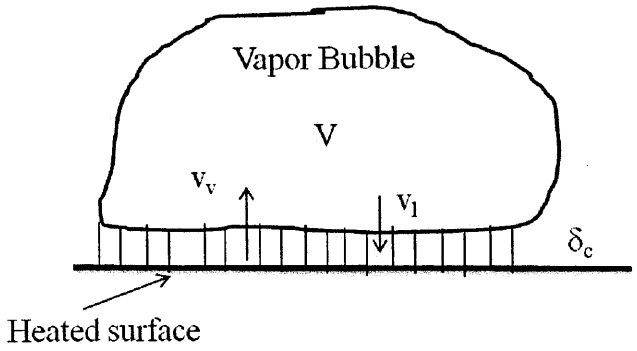

Figure 5-1: Vapor Mushroom and the Liquid Macrolayer

The vapor mushroom hovers on top of the heated surface for a time, τ_d, before departure. In the mean time, the liquid layer evaporates due to heat from the surface while it is being replenished by cold liquid. If the liquid film is not replenished with liquid from the bulk fluid due to Helmholtz instability of the vapor column, CHF occurs when the entire liquid macrolayer evaporates before the end of the hovering time of the bubble. The CHF for an infinite flat plate can be calculated using the heat balance

$$\tau_d q''_{max} A_w = \rho_l \delta_c (A_w - A_v) h_{fg} \tag{5-6}$$

where τ_d is the hovering time, δ_c is the thickness of the macrolayer, and A_w and A_v are the wetted area and area of vapor, respectively. The macrolayer thickness, δ_c, can be assumed to be approximately one-fourth of the critical wavelength, λ_H, for Helmholtz instability wavelength.

$$\delta_c = \frac{\lambda_H}{4} = \frac{\pi}{2}\sigma \frac{(\rho_l + \rho_v)}{\rho_l \rho_v}\left(\frac{A_v}{A_w}\right)^2 \left(\frac{\rho_v h_{fg}}{q''}\right)^2 \tag{5-7}$$

The hovering time for a bubble with volumetric flow rate, v_1, is defined as

$$\tau_d = \left(\frac{3}{4\pi}\right)^{\frac{1}{5}} \left[\frac{4(\xi\rho_l + \rho_v)}{(\rho_l - \rho_v)g}\right]^{\frac{3}{5}} (v_1)^{\frac{1}{5}} \tag{5-8}$$

with ξ is the volumetric ratio of the liquid to the moving bubble, which was estimated as $\frac{11}{16}$ in the model. The volumetric flow rate, v_1, of the bubble is defined as

$$v_1 = \frac{\lambda^2 q}{\rho_v h_{fg}} \tag{5-9}$$

where λ is the most dangerous wavelength presented in equation (5-3). Using equation (5-6) to (5-9), and expression for CHF can be obtained as

$$\frac{q''}{\rho_v h_{fg}} = \left(\frac{\sigma}{(\rho_v-\rho_l)g}\right)^{\frac{1}{4}}\left(\frac{\pi^4}{18}\right)^{\frac{1}{16}}\left(\frac{A_v}{A_w}\right)^{\frac{5}{8}}\left(1-\frac{A_v}{A_w}\right)^{\frac{5}{16}}\left(\frac{\rho_l}{\rho_v}+1\right)^{\frac{5}{16}}\left(\xi\frac{\rho_l}{\rho_v}+1\right)^{\frac{3}{16}} \quad (5\text{-}10)$$

The ratio $\frac{A_v}{A_w}$ for $\rho_v \ll \rho_l$, can be estimated as

$$\frac{A_v}{A_w} = 0.0584\left(\frac{\rho_v}{\rho_l}\right)^{0.2} \quad (5\text{-}11)$$

which is generally much less than 1 because the vapor to liquid density ratio is small. An assumption made is this model is that the fluid is well wetting. This model applies for both pool and flow boiling.

5.1.3 Dynamic Microlayer Theory

The dynamic microlayer theory proposed by Zhao et al. [86] is similar to the macrolayer dry out theory. However, in this model, the dryout area is the microlayer underneath each individual bubble rather than the macrolayer underneath the vapor mushroom. The macrolayer is assumed to never dry out due to continuous supply of liquid. The microlayer forms during initial growth period of the bubble. This microlayer evaporates with time and it cannot be replenished from the bulk liquid due to the extremely thin layer. Liquid is only resupplied to the area once the bubble departs. As the heat flux increase, the initial thickness of the microlayer decreases, which leads to shorter evaporation time and higher speed of partial dryout. CHF is predicted when the time average heat flux during departure period of bubble has a maximum point, i.e. $\frac{\partial q}{\partial \Delta T_{sat}} = 0$, where $\Delta T_{sat} = T_{wall}^{CHF} - T_{sat}$. The final expression for CHF is a function of the superheated temperature, the thermophysical properties, the departure period as well as the diameter of individual bubble at the end of the initial growth. However, using this model to predict CHF requires iteration.

5.1.4 Bubble Interaction Theory

The bubble interaction theory/model was first proposed by Rohsenow and Griffith [87] in 1956 but was not as widely used as the hydrodynamic theory. This theory states that as heat flux increases, the frequency and number of bubbles formed are so high such that they coalesce and reduce the interaction area between the heated surface and the liquid. Kolev[88] improved the theory further by considering the shear interaction between the departing and growing bubbles.

As the number of nucleation site density increases for high superheated temperature, the bubble diameter decreases. This means that less latent heat can be transferred out per bubble departure. The bubble departure time also decreases due to lower bubble diameter. At one point as the heat flux keeps on increasing, there is a reversal in the heat transfer coefficient, which is the point of CHF. Kolev's model also takes into account of the static contact angle and the model shows that higher contact angle leads to lower CHF. Also, this model originates from nucleate boiling prediction and does not require a separate CHF model. The final results for Kolev's expression for nucleate boiling heat flux is summarized as

$$q = \frac{2}{(0.84\pi)^{0.5}}\left(\frac{\rho_l k_l c_{pl}}{\rho_v h_{fg}}\right)(t_g f)^{0.5}\left(\frac{cN_{SD}^{\frac{1}{4}}}{\lambda_t^{0.5}}\right)(T_w - T_{sat})^2 \qquad (5\text{-}12)$$

In this equation, t_g, f, N_{SD}, c and λ_t are respectively the bubble departure time, the bubble departure frequency, the nucleation site density, a constant and the Rayleigh-Taylor instability wavelength, respectively. Using the appropriate bubble departure diameter and frequency proposed by Kolev[89], the plot of heat flux versus super heated temperature will have a reversal in the slope as mentioned before, and this indicates the point of CHF.

5.1.5 Hot/dry Spot CHF Theory

The hot/dry spot CHF theory/model postulates that hot/dry spots formed underneath the bubbles at the nucleation sites on a surface that are subjected to high heat flux. As these bubbles depart, these spots can be rewetted and they are considered reversible hot spots. However, if the surface has low wettability, these hot spots may not be rewetted, and they are considered irreversible hot spots. The temperature of the surface at these hot spots then increases sharply and the area of these irreversible hot spots will grow by radial conduction, eventually causing burn-out. To consider the effect of surface wettability on the rewetting of the hot spot, Theofanous and Dinh [90] proposed a model that considers the micro-dynamics of the solid-liquid-vapor line at the boundary of the hot/dry sport. In this model, CHF is predicted to occur when the recoil force driving the liquid meniscus to recede exceeds the surface tension force, which drives the meniscus to advance and rewet the hot/dry spot. The expression for the recoil force and the surface tension force are as follow.

$$F_v \sim \frac{1}{2}\rho_v U_v^2 \text{ with } U_v = \frac{q}{\rho_v h_{fg}} \tag{5-13}$$

$$F_\sigma \sim \sigma R \tag{5-14}$$

where R is the curvature, which is related to the capillary length as $R = \kappa\left(\frac{\sigma}{g(\rho_l-\rho_v)}\right)^{0.5}$

From equation (5-13) and (5-14), and expression for CHF can be found as

$$q''_{CHF} = \kappa^{-0.5} h_{fg}\rho_v \left[\frac{\sigma g(\rho_l-\rho_v)}{\rho_v}\right]^{0.25} \tag{5-15}$$

Kim et al. [17] derived an expression for κ base on geometry and Lord Rayleigh's formula for the volume of static liquid meniscus

$$\kappa = \left(1 - \frac{\sin(\theta)}{2} - \frac{\left(\frac{\pi}{2}-\theta\right)}{2\cos(\theta)}\right)^{-0.5} \tag{5-16}$$

where θ is the contact angle. However, equation (5-16) is only applicable for $\theta < 90°$. Also, a model by Kandlikar [53], which balances the momentum force due to evaporation against surface tension forces and gravitational force on the bubble, incorporates the effect of surface wettability on CHF. An expression for CHF as function of contact angle and other thermo physical properties is

$$q''_{CHF} = h_{fg}\rho_g \frac{1+\cos(\theta)}{16}\left[\frac{2}{\pi} + \frac{\pi}{4}(1+\cos(\theta_R))\cos(\phi)\right]^{0.5}\left[\frac{\sigma g(\rho_l-\rho_v)}{\rho_v}\right]^{0.25} \tag{5-17}$$

where θ and ϕ are the dynamic receding contact angle and the angle of orientation of the heater relative to horizontal surface. The model by Kandlikar is applicable for all contact angle.

5.1.6 Summary

The CHF models above mostly focus on the dynamic of the vapor/liquid interface as the mechanism for CHF instead of the surface properties. Only the hot and dry spot takes into account of surface wettability. Whether these models can describe the effect of surface roughness and porosity from porous coating is discussed next.

5.2 Effect of Surface Roughness on CHF

5.2.1 Surface Roughness Enhancing Heat Transfer Area and Wettability

Surface roughness, usually quantified by Ra, is defined as the arithmetic average of surface profile amplitude. Increase in surface roughness can affect CHF as follow. When the surface roughness increases, it can effectively enhance the surface wettability, which is known to raise CHF. When the roughness of a surface is increased, the contact angle is also changed according to the Wenzel's relation [91] or also known as the modified Young equation.

$$\cos(\theta) = r\cos\theta^* = r\frac{(\gamma_{SV} - \gamma_{SL})}{\sigma} \tag{5-18}$$

Equation (5-18) relates the apparent contact angle (θ) to the surface roughness factor (r) and the intrinsic contact angle (θ*). The intrinsic contact angle is determined by surface tensions of the solid-liquid (γ_{SL}), solid-vapor (γ_{SV}), and liquid-vapor (σ) interfaces. $\gamma_{SL} - \gamma_{SV}$ is the so-called adhesion tension. The surface roughness factor, r, is defined as the ratio of the effective contact area to the smooth contact area.

In this study, the increase in surface roughness (15 μm in *Rz* and/or 2μm in *Ra*) had little effect on CHF of a well-wetting fluid, FC-72. There was little change in the heater surface area due to the existence of the posts. The results here agree with those by Golobic and Ferjancic [92] who found very little CHF enhancement (6-12%) by changing *Ra* of a Steel ribbon heater from 0.07 μm up to 1.5 μm using sand paper. Similar study by Berenson [93] showed that surface roughness altered by sandpaper had very little effect on CHF of n-pentane but can change heat transfer coefficient by 500-600%. However, an extension of a study by Ferjancic and Golobic [40] showed CHF enhancement up to 15-20% for both FC-72 and water with steel ribbon heaters when the *Ra* of the surface increased from 0.07 μm up to 1.5 μm. However, they also found that etched surface with small *Ra* had much higher CHF enhancement. They concluded that *Ra* might not be the most appropriate parameter to describe effect on CHF. Ramilison et al. [94] increased surface roughness from a mirror finish surface using sand paper and found that CHF enhancement of 25 to 35%. However, the surface's parameter was not reported here, which made it hard to determine the actual mechanism for CHF enhancement. Rainey and You [95] created square pin-fin of 1 mm^2 base and height from 1 to 8 mm and measured CHF of saturated FC-72.

They found no CHF enhancement if they account for surface area of the fin. In fact, the 8mm long fin had CHF deteriorated by a factor of 2 from a flat surface (no fin). The CHF value for their flat surface was 18.8 kW/m^2.

Honda et al. [96] and Wei and Honda [97] also created square fin (thickness by height: 30 μm x60μm, 30 μm x120μm, 30 μm x60μm, 30 μm x200μm, 50 μm x60μm, 50 μm x 200μm and 50 μm x 270μm) at pitch of 2 times the thickness on silicon chip. They found CHF of FC-72 at various subcooled conditions (0K, 25K and 45K) higher than the surfaces without pins. However, their CHF values were calculated based on the base surface. They did not take into account of the extra area created by the fins. In fact, they reported an area enhancement factor of 2.2 for a surface with 50 μm x60μm fins and yet the CHF of this surface calculated using the base surface area, is only 75% higher than the flat surface. Other interesting data points in this study are of a smooth surfaces with a 3μm thick coating layer of SiO_2. The surface roughness and area did not change; yet, CHF enhancement of up to 40% was still observed. The mechanism for such CHF enhancement was not described.

As the data in this study and in the literature showed, surface roughness by itself seems not to be a primary effect. However, when changing the surface roughness via sanding or other macroscopic process, often the surface wettability is also changed as mentioned earlier. In this study, even with the array of posts of 200μm diameter, the surface roughness factor barely changed, which means that the contact angle on the surface should not change much at all, as already reported in Chapter 4. The effect of contact angle on CHF has been shown in equation (5-17). With the contact angle and other parameters remaining the same, the change in surface roughness had no effect on CHF was as expected.

5.2.2 Effect of Surface Roughness on Macrolayer Thickness

According to the macrolayer theory, the CHF is proportional to the initial macrolayer thickness. Using equation (5-7), the macrolayer thickness layer of FC-72 at CHF of 150 kW/m^2 on the plain wafer is approximately 68 μm. Notice that equation (5-7) has been verified to work fairly well by a study of Rajvanshi et al. [98], who measured the macrolayer thickness for various fluids. On the surface with micron-size posts of maximum height of 15 μm, the macrolayer total volume

could be reduced due to these micron-size posts. The size of the macrolayer is estimated as the most susceptible wavelength for Taylor instability, λ_D, which is approximately 7.8 mm for saturated FC-72.

$$\lambda_D = 2\pi\sqrt{3}\sqrt{\frac{\sigma}{g(\rho_l - \rho_v)}} \tag{5-19}$$

The reduction in the macrolayer volume can be estimated as

$$V_{red} = N_{post} * \pi * r_{post}^2 * H_{post} \tag{5-20}$$

where V_{red}, N, r_{post} and H_{post} are respectively the reduction in volume, the number of posts under the macrolayer, the radius of the post and the height of the post. The number of the posts at 500 μm pitch in a square of side 7.8 mm is approximately 250. Using equation (5-20), the volume reduction for surface with 200 μm posts is approximately 1.18E-10 m^3, which is approximately 3% of the total volume of the macrolayer of size 7.8 mm and thickness of 68μm. Considering the uncertainty in the approximation of macrolayer thickness, it can be determined that the macrolayer was not affected at all by the presence of the posts. This may explain why the CHF values for these surfaces were essentially not different from that of the bare surface.

5.3 Effect of Porosity on CHF

The effect of porosity (at least for surfaces with micron-size particles) on CHF has been investigated widely by many researchers as mentioned previously in Chapter one. However, the mechanism for CHF enhancement with porous layer is not entirely understood. This is because the porous coating layer usually changes many different characteristic at the same time: from increase in nucleation site density and enhanced wettability, surface roughness to create new feature such as capillary pumping effects. In this section, a review of existing correlations and models for CHF of porous surface and a comparison with the data in the literature will be presented. The focus here will be on pool boiling since the data for flow boiling CHF of porous surface are scarce and incomplete. Also, there exists virtually no model to describe mechanism for flow boiling CHF for porous surfaces.

5.3.1 CHF Models and Data for Porous Surface

5.3.1.1 Correlation of Porosity on CHF

The effect of how porous coating structure enhances CHF is still not clear. There are usually two types of porous coating applied on a surface: uniform coating layer or modulated coating layer. One of the models describing the effect of porosity on CHF was proposed by Polezhaev and Kovalez [36]. They derived a semi-empirical correlation, based on Zuber hydrodynamic theory, to establish a relationship between CHF and porosity ϵ, as well as the break through pore radius, R_{bg}, a valued determined from experimental data. Usually, one can assume it is half the particle diameter in the coating layer. The correlation only applies to uniform porous coating layer. The expression for CHF is as follow.

$$q''_{CHF} = 0.5\,\epsilon^{2.28} h_{fg} \left(\frac{\sigma \rho_l \rho_g}{(\rho_l + \rho_g) R_{bg}} \right)^{0.5} \tag{5-21}$$

Using equation (5-21), CHF of FC-72 as a function of particle diameter and porosity are plotted as shown in Figure 5-2. The data in this study and from some other studies in the literature are also shown for comparison. The average porosity for a randomly distribution porous coating layer of single size particle is about 40%. One can see that CHF decreases with increasing particle diameter but increases with increasing porosity. However, the very steep increase in CHF as particle diameter gets smaller may seem unrealistic. It seems that there should be a diameter where the curve flattens. Also, this correlation does not take into account the thickness of the coating layer either. Finally, while the approximation of R_{bg} as half of the particle diameter may be appropriate for micro-size particles, it may not make sense for nanoparticles since the bubble radius is usually much larger than nano scale.

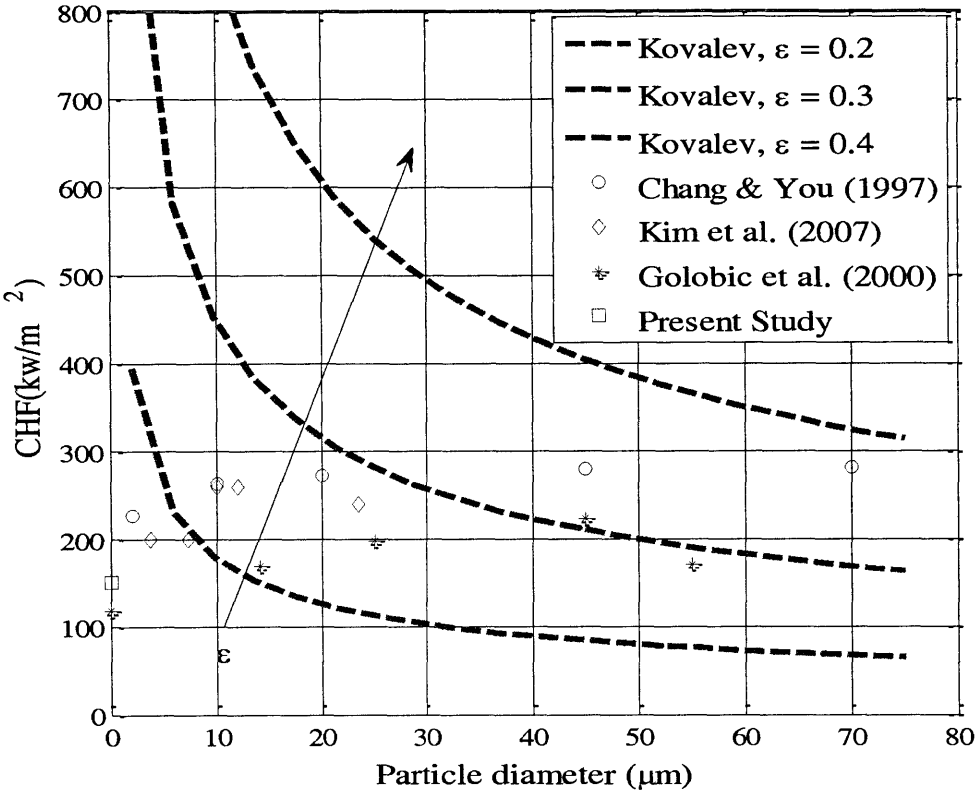

Figure 5-2: Effect of Particle Diameter and Porosity on CHF of FC-72

5.3.1.2 Udell Model for CHF of Porous Coating Layer

One of the earlier CHF models for porous coating was that of Udell [99]. In this model, three distinct regions exist above a heated surface. A vapor zone right on top of the heater, then the two-phase zone and finally a liquid zone. The CHF depends on the liquid and vapor counter current flow within the two-phase zone. Using Darcy's equation, the mass fluxes and pressure gradients of vapor and liquid within the two-phase zone are defined. With the capillary pressure defined as the difference between vapor and liquid pressure, and using relationship between capillary pressure and saturation data, an expression for thickness of the porous coating layer can be established as function of heat flux. The final expression is as follows [99]:

$$\frac{ds}{d\delta} = \frac{1 - \omega\left(\frac{1}{\kappa_{rv}} + \frac{\beta}{\kappa_{rl}}\right)}{f'} \tag{5-22}$$

where κ_{rv}, κ_{rl} are the relative permeability of vapor and fluid, respectively. s is the saturation function. s= 0 at the heater surface and $s = 1$ at the end of the two phase zone. f' is an empirical function of s. ω, β and δ are the dimensionless quantities, which are defined as $\omega = \frac{q'' v_v}{\left(\kappa h_{fg} g(\rho_l - \rho_g)\right)}$; $\beta = \frac{v_l}{v_v}$; and $\delta = \frac{x(\rho_l - \rho_g)}{\sigma}\left(\frac{\kappa}{\phi}\right)^{\frac{1}{2}}$. Using equation (5-22), and function of f' as

$$f = 1.417(1-s) - 2.120(1-s)^2 + 1.263(1-s)^3$$
$$f' = -1.417s + 2 * 2.120(1-s) - 3 * 1.263(1-s)^2 \quad (5\text{-}23)$$

with assumed value for the porosity and permeability, a relationship between heat flux and thickness of porous layer can be obtained. The expression for critical heat flux for the case of bottom heating is as follow

$$\frac{q''_{CHF} v_v}{\left(\kappa h_{fg} g(\rho_l - \rho_g)\right)} = \left[\frac{1}{1 + (\beta)^{\frac{1}{4}}}\right]^4 \quad (5\text{-}24)$$

where β is the ratio of kinematic viscosity of liquid to vapor, v_v is the kinematic viscosity of vapor. As equation (5-24) shows, the CHF only depends on κ, the porous surface's permeability, which has a dependence on particle diameter and porosity as

$$\kappa = \frac{d_p^2 \epsilon^3}{150(1-\epsilon)^2} \quad (5\text{-}25)$$

This means that the CHF increases with increasing particle diameter in the porous coating. This does not agree with the correlation of Polezhaev and Kovalez [36]. However, the two models agree that CHF is higher with higher porosity. To apply equation (5-24) for this current study, the value of κ, the permeability of the porous coating needs to be determined. Using equation (5-25) to evaluate κ for the LBL coating of 50 nm particles and porosity of 0.40 in this study, the value is of order 10E-19, which is not realistic. Therefore, we cannot apply this model for the data in this study, unless κ can be determined accurately.

5.3.1.3 Lu and Chang Model

Lu and Chang [100], using similar arguments to that of Udell [99], provided a model for CHF as function of coating thickness and particle diameter. In their model, some assumptions were

made, such as fixed bed of particles in porous layer, bottom heating, and permeability equations applied to both laminar and turbulent flow regime inside the porous structure. They defined CHF as the point at which the relative liquid saturation at the heater surface is 0. The relative liquid saturation, *Se,* is defined as

$$Se = \frac{s_l - s_{lp}}{1 - s_{lp}} \tag{5-26}$$

where s_l and s_{lp} are the volume fraction of liquid in the pores and the saturation of immobile water. A detailed derivation of the model is attached in the appendix. For very thick porous coating layer, the CHF increases with increasing particle diameter. The relationship between CHF and particle diameter can be separated out for laminar and turbulent flow dominant regimes in the pore channel. For laminar flow,

$$\log(q_{CHF}) = \log\left[\frac{B_{max}\Delta\rho g h_{fg}}{150\nu_v}\frac{\epsilon^3}{(1-\epsilon)^2}\right] + 2\log(d_p) \tag{5-27}$$

where $B_{max} = \frac{1}{\left(\frac{c_v}{\kappa_{rl}} + \frac{1}{K_{rv}}\right)}$

For turbulent flow regime,

$$\log(q_{CHF}) = \log\left[h_{fg}\sqrt{\frac{\rho_v\Delta\rho g h_{fg}}{1.75}\frac{\epsilon^3}{(1-\epsilon)^2}}B_{max}\sqrt{\psi}\right] + \frac{1}{2}\log(d_p) \tag{5-28}$$

and $B_{max}\sqrt{\psi} = \left[\frac{1}{\left(\frac{1}{K_{rl}c_\rho} + \frac{1}{K_{rv}}\right)}\right]^{0.5}$. Here c_v, c_ρ are kinematic and density ratios of the fluid to the vapor, respectively. As equation (5-27) and (5-28) show, as particle diameter increases, CHF increases for very thick porous medium (several hundreds of micrometer to several mm thick). This agrees with the model of Udell [99]. Also, for the same particle diameter, the larger the thickness, the lower the CHF. However, this deterioration saturates when the coating thickness is several centimeters. Of course, this model overall does not apply to the coating in this study, which has thickness of only about 1 μm. Furthermore, Figure 5-3 shows that the CHF decreases very quickly to zero as the particle diameter goes to the nanometer range, which is not realistic and contrasts with the current experimental data.

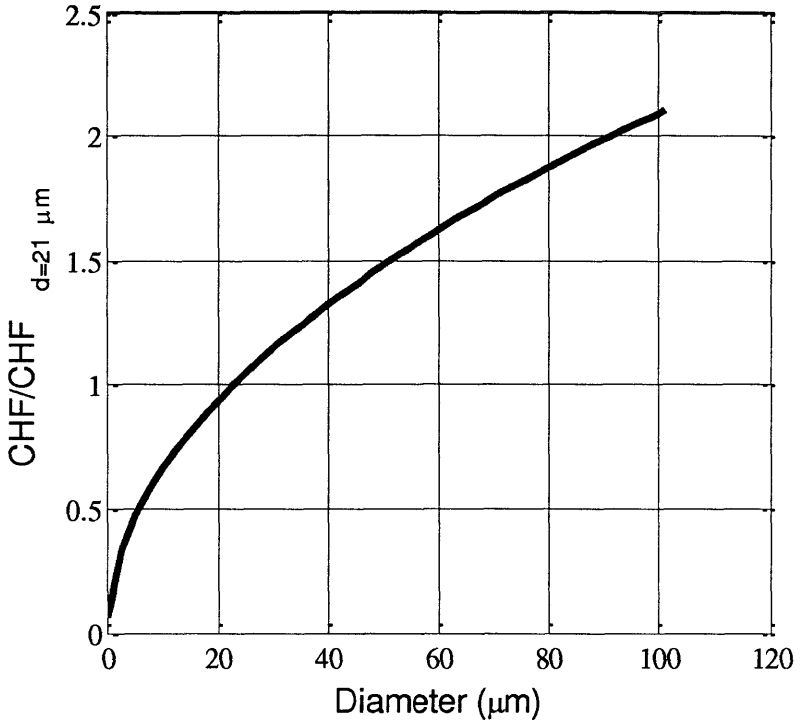

Figure 5-3: Effect of Particle Diameter on CHF - Lu & Chang Model [100]

5.3.1.4 Mori & Okuyama Model

Mori and Okuyama [101] ran CHF experiments using surface coated with honeycomb structures of different thickness (order of mm) and different channel widths. The pore size of the honey comb is 0.1 μm. They found highest CHF enhancement with the thinnest honeycomb. Using CHF model based on capillary limit, a relationship between CHF and different parameters of the honeycomb was derived. Using the balance of pressure, $\Delta P_c = \Delta P_l + \Delta P_v + \Delta P_a$, where $\Delta P_c = \frac{2\sigma}{r_{eff}}$ is the capillary pressure drop, $\Delta P_l = \frac{\mu_l Q_{max} \delta_h}{K A_w \rho_l h_{fg}}$ is the liquid pressure drop, $\Delta P_v = \frac{32 \mu_l Q_{max} \delta_h}{\rho_v n d_v^4 h_{fg}}$ is the vapor pressure drop and $\Delta P_a = \frac{\rho_v}{2}\left(\frac{(Q_{max})}{\rho_v n d_v^2 h_{fg}}\right)^2$ is the acceleration pressure drop, one can solve for the heat flux as

$$q_{CHF} = \frac{Q_{max}}{A} = \frac{-B + \sqrt{B^2 + 4 * \frac{2\sigma}{r_{eff}}}}{2AC} \tag{5-29}$$

with $B = \frac{\mu_l \delta_h}{\kappa A_w \rho_l h_{fg}} + \frac{32\mu_l \delta_h}{\rho_v n d_v^4 h_{fg}}$; $C = \frac{\rho_v}{2}\left(\frac{1}{h_{fg}\rho_v n d_v^2}\right)^2$, n is number of vapor escape channels, d_v is the vapor channel width and r_{eff} is the effective pore diameter. A is the heated area.

Figure 5-4 shows the effect of vapor channel diameter, d_v, in the honeycomb structure, on the CHF using the capillary limit model by Mori and Okuyama [101]. There seems to be an optimal vapor channel diameter for CHF. This model can be considered the middle point between the models by Polezhaev and Kovalez [36], and those by Udell [99], and Lu and Chang [100]. Reminding that Polezhaev and Kovalez [36] predicted higher CHF with smaller particle diameter while Udell [99], and Lu and Chang [100] predicted higher CHF with larger particle diameter. One should also notice that the CHF is highly sensitive to the permeability of fluid in the porous layer, which is usually not reported in the literature. Again, similar to Lu & Chang model, the CHF decreases to zero as the particle diameter approaches nanometer range, inconsistently with data in the present study.

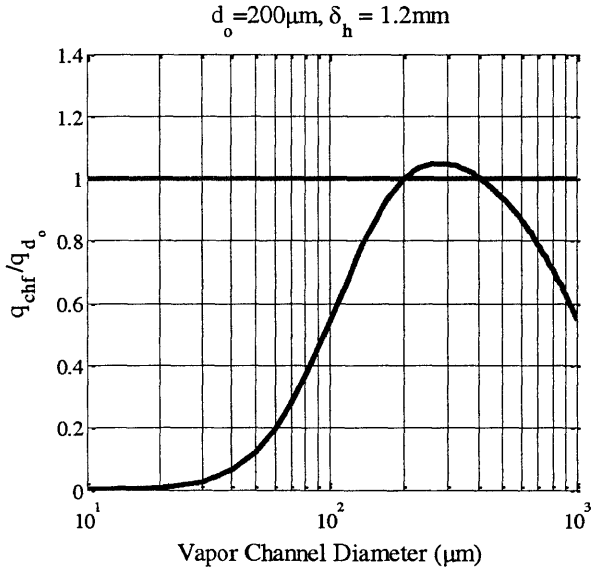

Figure 5-4: Effect of Vapor Channel on CHF by Mori & Okuyama Model [101]

5.3.1.5 Liter and Kaviany Model

Liter and Kaviany [60] coated heater surfaces with modulated porous coating layer, which contains spherical copper particles diameter of diameter of 200 μm molded into conical stacks. They measured CHF enhancement of more than 200% with the coated surface compared to the

plain one using pentane. To explain the observed CHF enhancement, they provided two models. The first one is known as hydrodynamic liquid-choking limit. This model is similar to the Zuber hydrodynamic instability model. However, it is only applicable to modulated porous coating surface (periodically non-uniform thickness). This modulated porous surface separate flow of liquid and vapor phase (similar to Mori & Okuyama [101] honeycomb structure). They proposed that the hydrodynamic instability is proportional to the distance between conical stack, λ_m, which is called modulation wavelength. The dependence of CHF on λ_m is as follow.

$$q''_{CHF,h} = \frac{\pi}{8} h_{fg} \left(\frac{\sigma \rho_g}{\lambda_m}\right)^{0.5} \tag{5-30}$$

Using equation (5-30), the CHF of pentane as a function of modulated wavelength is plotted in Figure 5-5. Experimental data from some other works using porous coating are included for comparison. The CHF is inversely proportional to $\lambda_m^{0.5}$. The theory seems to work well for porous surface with modulated wavelength larger than 1 mm. However, for modulate wavelength of less than 1 mm, the theory seems to over predict the experimental results. Again, this suggests that there is also a turn-around point for the modulated wavelength. The authors suggested that the limit for the modulated wavelength could be the particle diameter itself. At this point, the surface lost its modulated function, and approached the uniform porous coating limit. In addition, it should be noted that the model here does not take into account of the particle diameter and the pore size. Finally, it does not apply to a uniform porous coating structure either.

The second model by Liter and Kaviany [60], called the viscous-drag liquid-choking limit model for fluid flowing through a porous stack, was described earlier in Chapter 2. As stated earlier, this model depends on other models used to describe treating porous medium as well as the assumption of simplified liquid flow paths. In addition, it only applies for modulated porous coating, not for uniform porous coating layer. The minimum particle diameter that is applicable to the model by Liter and Kaviany [60] also in the micrometer range, which means that it cannot be used to evaluate the CHF of the LBL in this study. Nevertheless, these models still show that CHF is generally enhanced with higher porosity. However, other factors including particle diameters, wettability and material can have a strong influence on CHF.

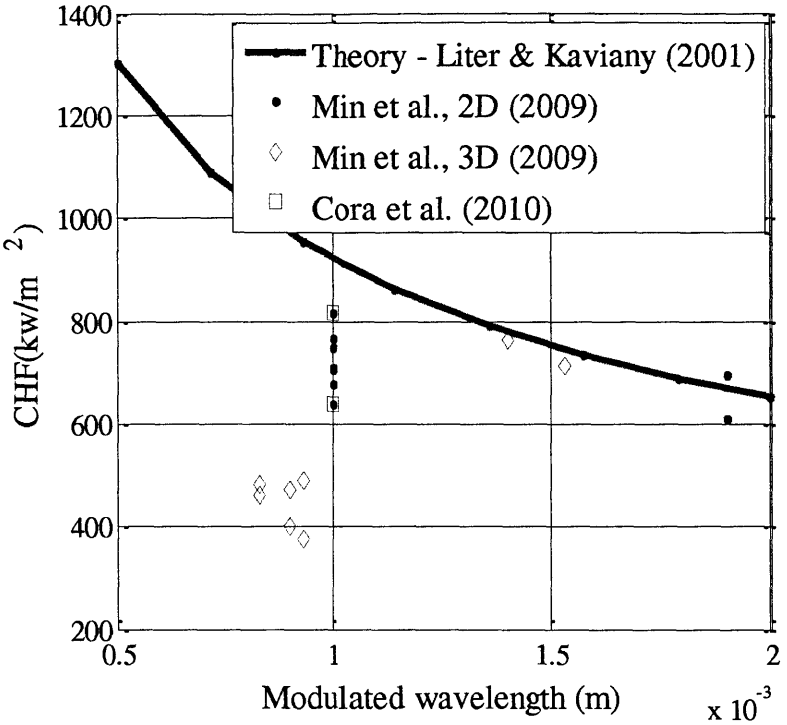

Figure 5-5: Effect of Modulated Wavelength on CHF - Liter and Kaviany Model [60]

5.3.1.6 Summary of CHF Models for Porous Coating Layer

The above models suggest that the parameters that seem to have large effects on CHF include diameter (particle or pore), coating thickness and porosity. However, there is no consensus regarding how these parameters individually affect CHF. For particle diameter, models by Liter and Kaviany [60] support that CHF decreases as particle diameter increases. This agrees with correlations by Polezhaev and Kovalez [36] while models by Lu and Chang [100] and Udell [99] indicate CHF increases with increasing particle diameter. On the other hand, results and model by Mori and Okuyama [101] suggest that there is an optimal particle diameter. All authors seem to agree that increasing porosity of the coating layer helps enhance CHF. For coating thickness, there is an optimal value at which increasing coating thickness beyond this value will cause deterioration of CHF. In the next section, a comparison of data in the literature for porous coating CHF will be presented to analyze which parameter of the porous coating seems to have the biggest effect on CHF.

5.3.2 Effect of Porous Coating Parameter on CHF

In this part, the effect of porous coating parameters, including mean particle diameter, average coating thickness and the ratio of coating thickness to particle diameter on pool boiling CHF enhancement relative to the plain surface will be summarized. The data come from different studies in the literature and are divided into two groups based on the fluids used in the experiments. The first group is for well wetting fluids such as refrigerants/pentane and the second group is for water.

5.3.2.1 Well-Wetting Fluids

Figure 5-6 plots the CHF enhancement ratio for well wetting fluid as a function of particle diameter. Most particles used in porous coating are in 10 and 100 μm diameter range and the majority of the CHF enhancement falls between 20% and 80%. There is virtually no data for nanometer size particle. The data by Im et al. [102] and Thiagarajan [103] are actually for surface coated with nanowire rather than nanoparticles. In Im et al. [102], the actual cavity size from the nanowire is on the order of 2 μm. For coating layer with particle diameter less than 100 nm, there seems to be no CHF enhancement at all. No clear trend of how particle diameter affecting CHF enhancement can be observed.

The effect of thickness of the porous coating layer on CHF enhancement ratio is not clear either, as shown in Figure 5-7. The coating thickness mostly falls in the range of 10s of micrometers to hundreds of micrometers. Finally, Figure 5-8 shows the effect of ratio of coating thickness to particle diameter on CHF enhancement. It is almost impossible to draw any conclusion based on the data here. Part of the reason may be due to the fact that the data comes from different coating particle materials, method of coating, base substrates and fluids. Detailed data are listed in the appendix.

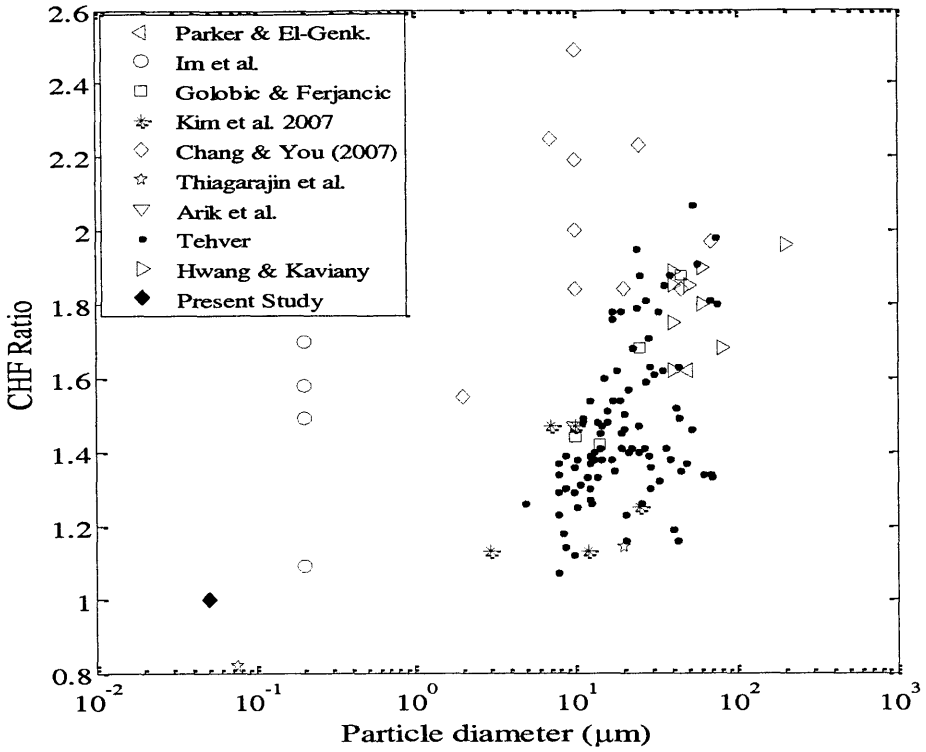

Figure 5-6: Effect of Particle Diameter on CHF Enhancement for Refrigerants

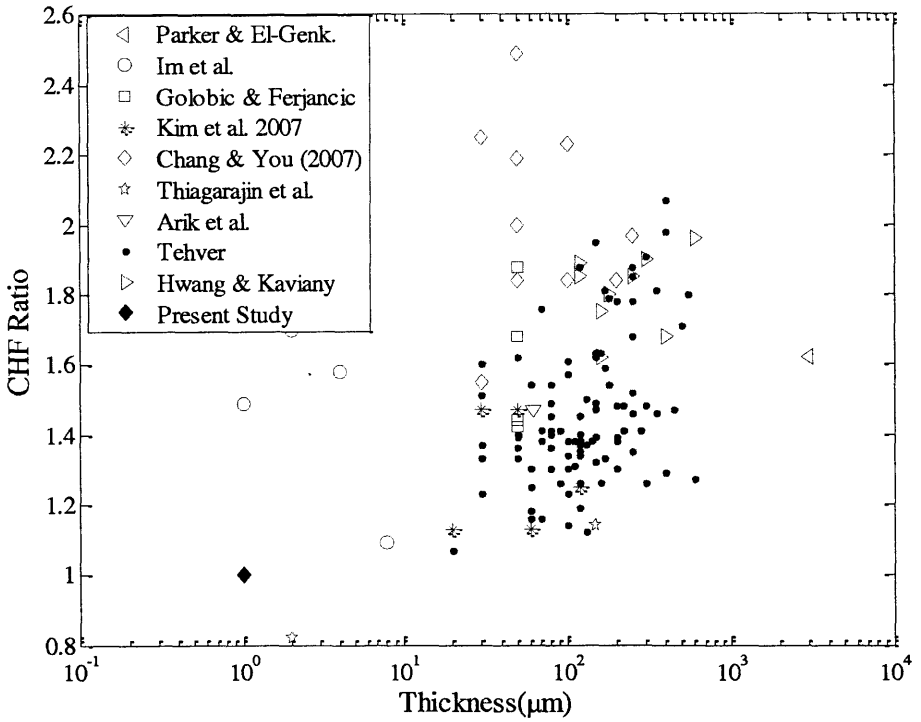

Figure 5-7: Effect of Thickness on CHF Enhancement for Refrigerants

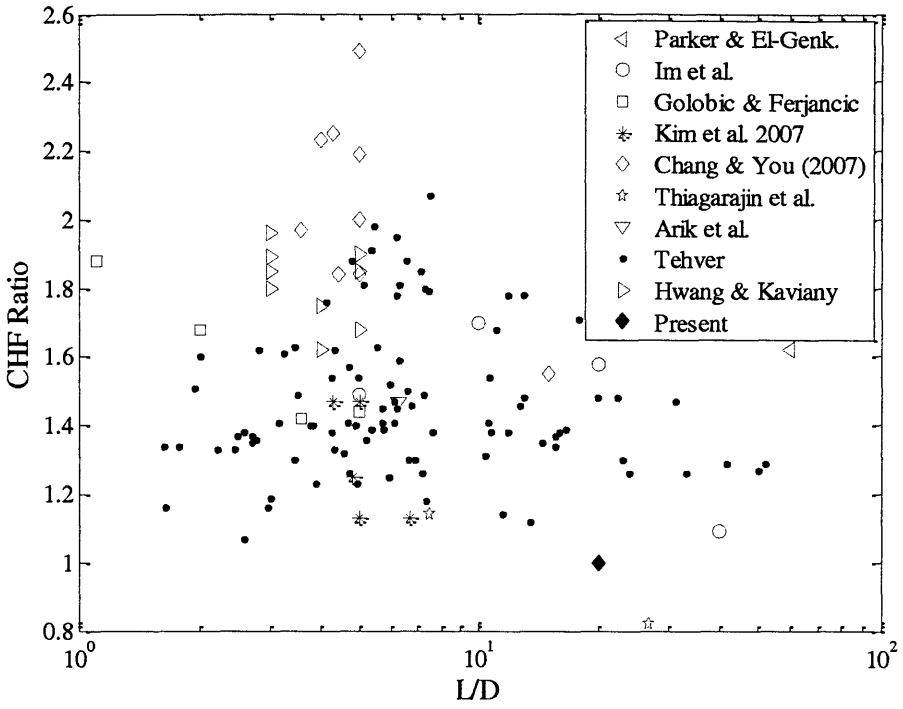

Figure 5-8: Effect of Thickness to Diameter Ratio on CHF Enhancement for Refrigerants

5.3.2.2 Water

Similar observations for porous coating surface enhancing CHF can be said for water as shown in Figure 5-9 to Figure 5-11. There is no clear trend of how the porous coating parameter affecting CHF enhancement ratio. One thing worth noticing is that the porous coating usually makes the surface become super-hydrophilic. According to Kandlikar correlation, a change in wettability by itself (from contact angle of 80° to 0°) can enhance CHF by a factor of about 2.1 without the need of porous structure. More than half of the data for water have CHF enhancement ratio less than 2.1, which makes it hard to quantify whether the porous structure has much effect on CHF enhancement at all.

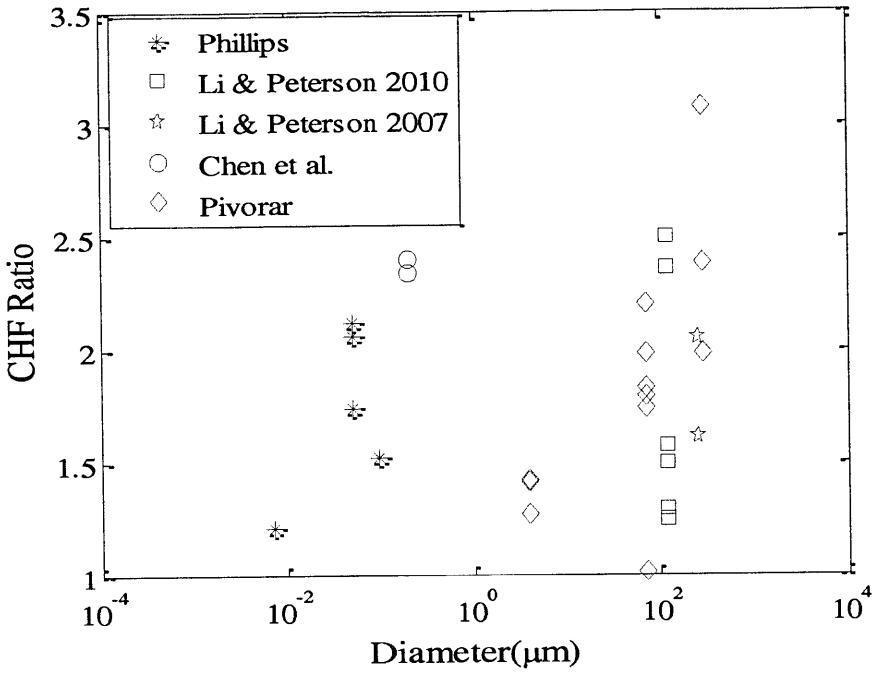

Figure 5-9: Effect of Particle Diameter on CHF Enhancement for Water

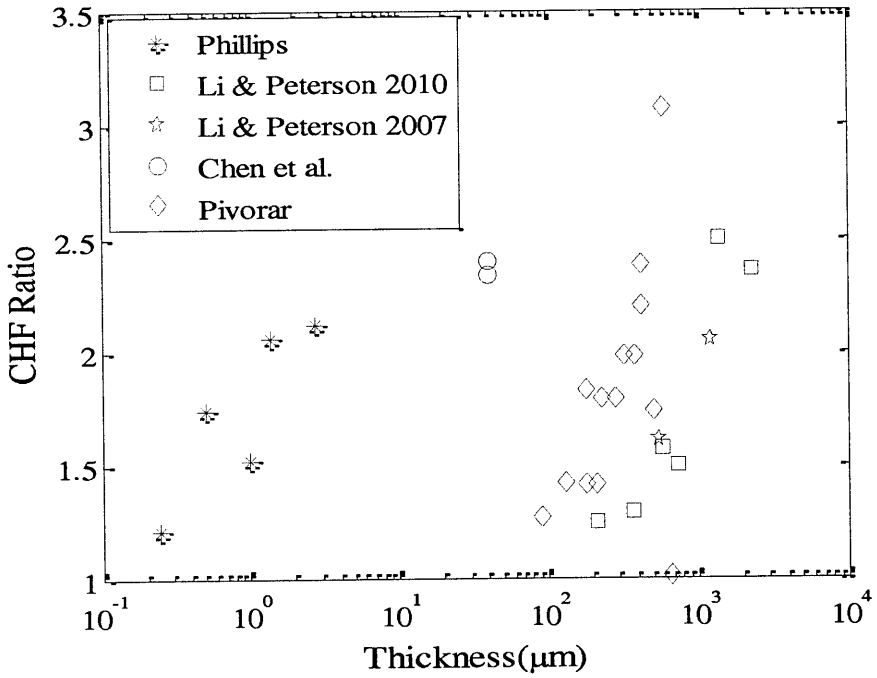

Figure 5-10: Effect of Coating Thickness on CHF Enhancement for Water

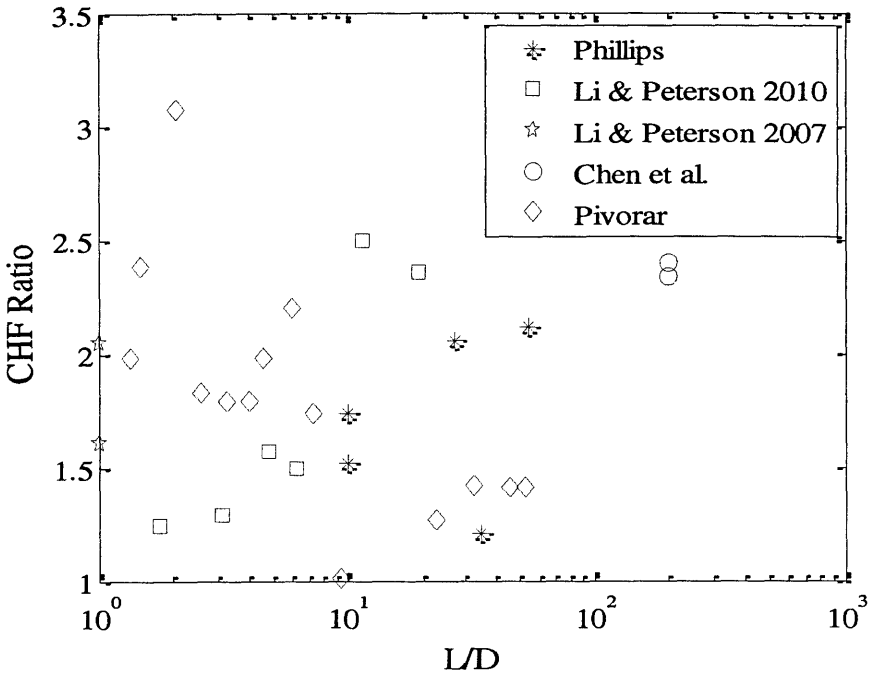

Figure 5-11: Effect of Thickness to Diameter Ratio on CHF Enhancement for Water

The effect of porosity on CHF enhancement ratio is shown in Figure 5-12. The trend is that higher porosity seems to provide higher CHF enhancement, which agrees with most models. Since only few studies reported the porosity of their porous coating, the data here are combined for both water and refrigerant.

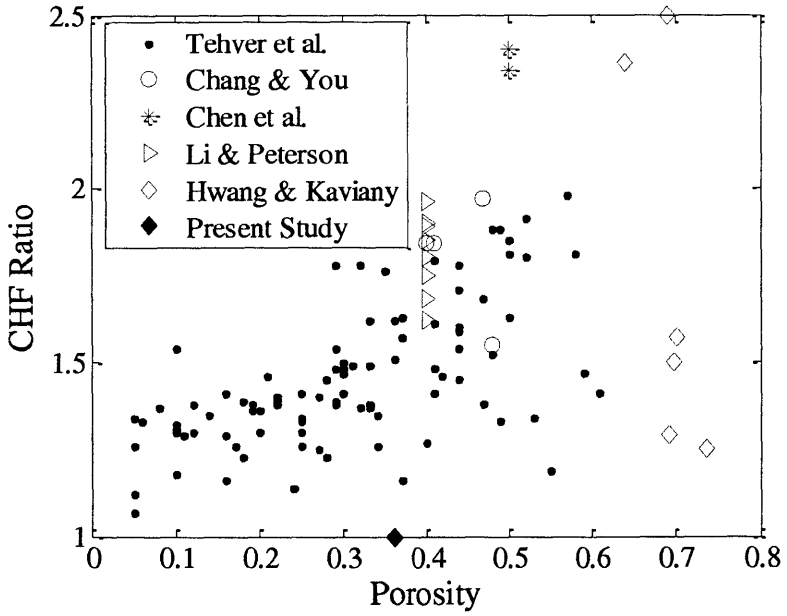

Figure 5-12: Effect of Porosity on CHF Enhancement for Porous Coating Surface

5.3.2.3 Summary of CHF Data for Porous Coating Surface

The data presented above suggest that there is no clear trend between the CHF enhancement and the porous coating parameters including particle diameter, coating thickness, the ratio of thickness to particle diameter, and porosity. One reason that none of the CHF model for porous coating seems to be able to capture the data is that most of these studies used micron-size particles for coating, which means that the coating layer effectively introduces/changes too many surface parameters at the same time. This makes it difficult to identify the most important parameter. The data in the current study show that the introduction of only nanoporosity by a porous coating of 50 nm diameter nanoparticles has no effect on CHF of FC-72, a well wetting fluid.

5.4 Summary

In this chapter, existing CHF models for bare and modified surfaces were reviewed to evaluate if they can explain CHF enhancement observed for surfaces with higher surface roughness and/or porous coating. Most conventional CHF theories usually do not take into account the surface structure (roughness and/or porosity). Existing CHF models for bare and modified surface fail to predict CHF enhancement of modified surface, especially those with porous coating. Data obtained for porous coating CHF enhancement as a function of particle diameter, coating thickness, thickness to particle diameter ratio, and porosity were shown to scatter over a wide range, possibly due to poorly characterized surface morphology. This makes it difficult to quantify the effect of porous structure on CHF and partly causes CHF models to fail to predict the data .

6 Conclusions and Future Work

6.1 Conclusions

This study evaluates the effect of heat transfer surfaces modified using nano fluid or micro/nano engineering features on critical heat flux (CHF) under flow and pool boiling conditions, and Leidenfrost point (LFP) during transition boiling. CHF marks the rapid deterioration of boiling heat transfer transitioning from nucleate to film boiling region, and the LFP corresponds to the lowest temperature of the surface for heat transfer in the film boiling regime. Both are critical phenomena in nuclear reactor design. By enhancing CHF and LFP, nuclear reactor fuel can be designed to operate at higher power density, thereby improving economic efficiency and safety.

In flow boiling experiments, the test section surfaces were pre-coated by boiling induced deposition of Alumina nanoparticle and/or polymeric particle (Poly(allylamine) hydrochloride - PAH) . For pool boiling and quenching experiments, nano-micro engineered surfaces were used. The engineered surfaces were fabricated with various nano- and micro-scale features, such as layer by layer (LBL) coating of nanoparticles and micron-size posts, for better control of surface morphology. The major findings are summarized as the following:

1) Using Alumina nanoparticle pre-coated test sections, it was confirmed that the nanoparticle deposited on the surface is responsible for the enhancement in subcooled flow boiling CHF of nanofluid up to 40% at 2500 kg/m^{2}s mass flux. The nanoparticle changed both surface wettability and porosity of the surface, which helped enhance CHF. However, current existing theory cannot explain the observed CHF enhancement. No change in heat transfer coefficient was observed between the coated test sections and the bare one. No CHF enhancement was observed for surfaces coated with Alumina/PAH at 2500 kg/m^{2}s or surfaced coated with Alumina at lower mass flux of 1500 kg/m^{2}s.

2) In single droplet quenching Leidenfrost point, nanoporosity (not solely wettability) is an essential feature for enhancing LFP up to 100 °C. The enhancement occurs via destabilization

of vapor film, which is caused by heterogeneous nucleation of bubbles. The combination of micro posts and nanoporous layer proved optimal for enhancing LFP.

3) Separate surface effects on CHF study shows that nanoporosity and roughness alone is not enough to affect pool boiling CHF of FC-72, a well-wetting fluid. Current CHF models for porous coating fail to predict existing experimental data due to two main reasons: a) Existing CHF models usually do not take into account of the porous surface parameters. b) the data for porous CHF scatter over a wide range and the surface structures are usually not well characterized.

6.2 Recommendations for Future Work

The last part of this study focused mostly on separate effects of surface parameters on pool boiling CHF of a well wetting fluid. For future work, the followings investigations are needed:

1. The single droplet quenching work here identified nanoporosity as the most important factor for LFP enhancement. Pool and flow quenching work with similar surface treatment should be performed to determine if such effect is retained.
2. Study the separate surface effect on pool boiling CHF for water. Care should be taken so that only one surface parameter is changed at a time. For water, the wettability is usually changed with the introduction of porous layer and/or roughness, and interface material. It is also necessary to have a thorough characterization of these surface parameters so that they can be used to explain the individual effect and/or to indentify the important ones.
3. Study separate surface effect on flow boiling CHF for both well wetting fluid and water. Visualization capabilities, including high speed video and infrared camera, if available, should be incorporated in the experimental design. This will provide better understanding of CHF mechanisms.
4. Identify the most important parameters, whether it is roughness, porosity, wettability or enhanced surface area, and incorporating them in existing or new models.
5. Based on the results in 4, perform an experimental and theoretical study on optimization of surface for CHF enhancement. For non-well wetting fluid such as water, the foci can include:

- Enhancing in surface wettability by oxide layer coating or nanoporous coating such as LBL. The durability of the coating needs to be considered for actual applications.
- Combination of the optimal micron-size post array geometry and the nanoporous layer coating.

6. The effects of oxide layer/crud deposited on the fuel cladding on CHF and quenching heat transfer should also be investigated. In some ways, the oxide layer/crud can be similar to the layer of deposited nanoparticles on heater surface.

Appendix A. Flow Boiling CHF Data Further Discussion

In Chapter 2, CHF results for batch number 5 (Test section 15Al to 18Al) and those for batch number 12 (C41Al to C43Al) were not included. This is because it was thought that the conditions of these test sections were different from the rest. While batch 5 test sections were coated in the same conditions as that of batch 4, no CHF enhancement was observed when batch 5 test sections were used to measure CHF of water. This was rather puzzling and it was suspected that there was no coating where CHF occurred, which was right below the top copper electrode. This could be due to an abrupt change from heating below the copper electrode and no heating inside the copper electrode. Since CHF in this case (DNB) is such a local phenomenon, even if a few locations right underneath the top copper electrode had no sufficient coating, there could be no CHF enhancement as observed here. Therefore, the coating loop and two-phase loop setup was changed slightly as shown in the figure below. Notice that the new pre-coated length was 11 cm but the heated length in two-phase loop was still 10 cm, starting from the bottom electrode. This change was made to coat C19Al test section and others afterward. This was to ensure that there will be a consistent coating layer of nanoparticle at the point right underneath the top copper electrode.

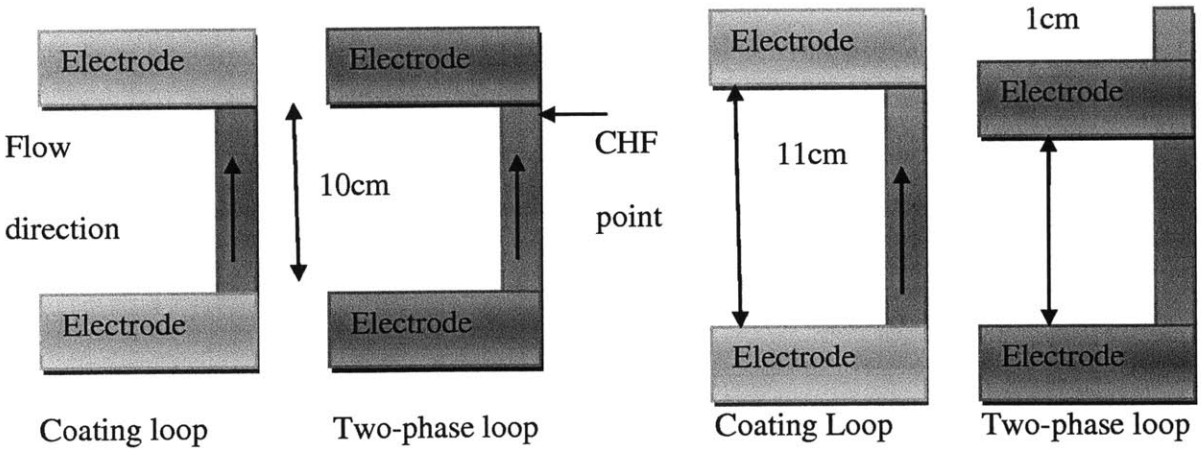

Figure A-1: Description of change in coating loop and two-phase loop test section set up after C19Al test section

For batch number 12, the test sections were coated under the same heat flux for 4 hours as in instead of 2 hours like in batch 5 and 6. However, no CHF enhancement was observed at G=2500 kg/m^{2}s with test sections in batch 12. This was not expected because longer coating time was expected to provide a better layer of Alumina nanoparticle. Too much coating could make the particles less adhered to the SS316 tube such that most of them could be removed due to shear force in the two-phase loop during degassing and heat flux increasing process. Surface characterization using SEM may provide an explanation. A possible reason for this is that these test sections had different initial surface finish (before coating) compared to the test section C14Al and C19Al. The SEM images below compare the surface structure of the different test sections. First, the **Bare-3** test section seems to have more features than the **As-Received** one does. Note that the **As-Received** test section comes from the same long tube as test section C41Al to C43Al while the **Bare-3** test section came from a different same long tube, where C14Al and C19Al were cut from. Note that **As-Received** here means that the test section was not run in any experiment before. The **As-Received** test section seems a lot smoother than **Bare-3**, which makes the coating of nanoparticles on the surface different. While all coated surfaces do not have uniform coating layer of Alumina nanoparticle, C14Al and C19Al coating seemed more durable because the nanoparticles locate inside the crevices on the bare surface. For C41Al and C42Al, the nanoparticles stuck in batches on top of the smooth surface. These could be washed away in flow conditions. There is more coating C14Al and C19Al test sections compared to that on test section C41Al and C42Al. The contact angle of water on C41Al and C42Al were also close to that on a bare tube. This suggests that the initial surface of the heater can affect the Alumina nanoparticle coating structure (both formation and durability), which can affect CHF.

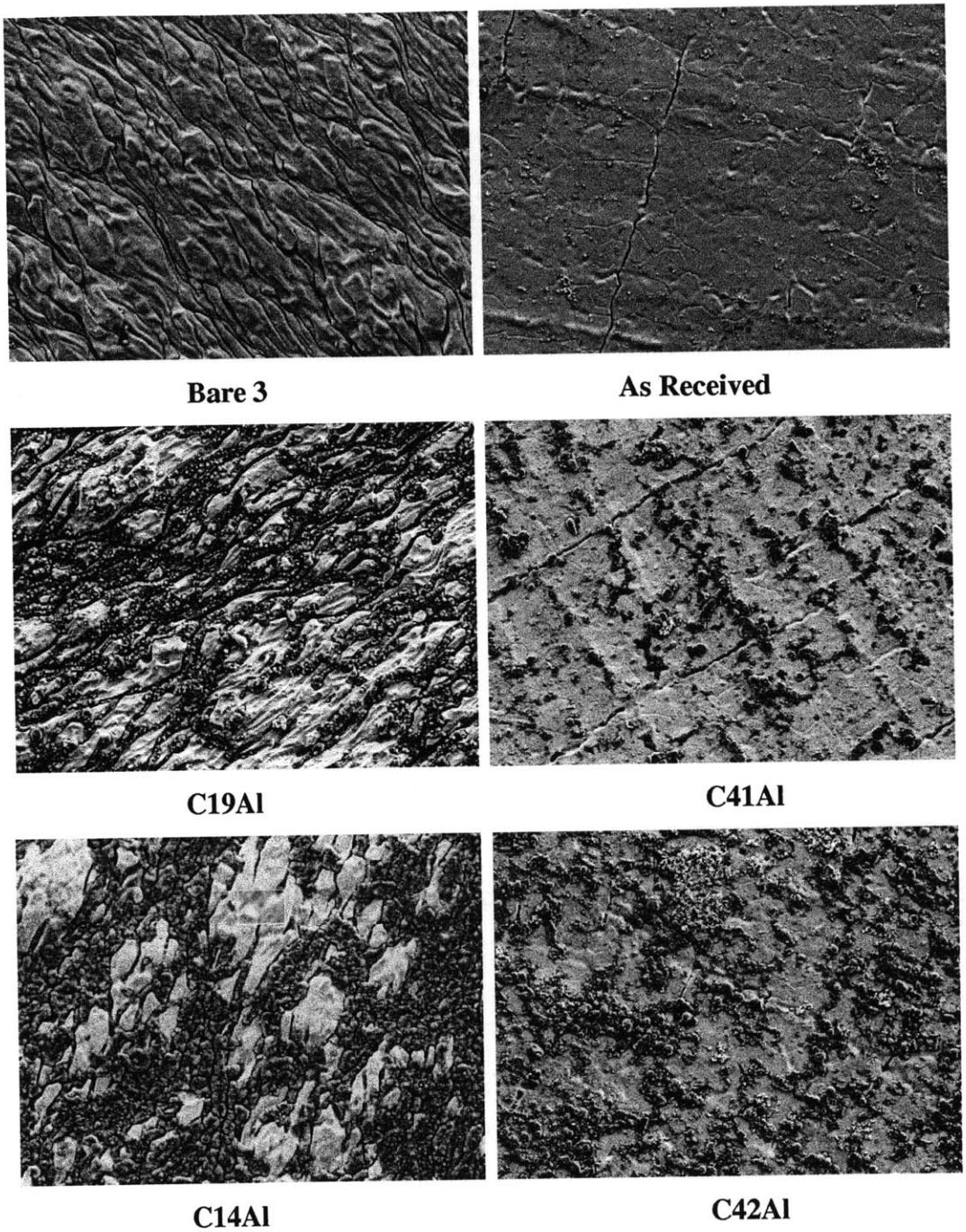

Figure A-2:Comparison of SEM Images (~1000X) Between Test Sections That Did (C19Al, C14Al) and Did not Enhanced CHF (C41Al and C42Al)

Appendix B. Tables of Data of Porous Coating CHF

This section lists the data for porous coating CHF that were compared in Chapter 5. The particle diameter and material, the coating thickness, coating technique, the base substrate materials and porosity are listed if they are available. The CHF values and enhancement ratio from the base surface are shown as well.

Arik and Bar-Cohen [39]
Base Substrate: Silicon Wafer; Fluid: FC-72; Particle: Diamond Powder; Coating method: Omegabond Epoxy with Methyl Ethyl Ketone Solution. Note: only use data point that is bolded. Base

Pressure	T_{bulk} (C)	Diameter (μm)	Thickness (μm)	CHF_Porous (kW/m^2)	CHF_bare	Enhancement
101.3	21	10	62.5	38.4	22.3	1.72
101.3	41	10	62.5	27.8	18.1	1.54
101.3	**55**	**10**	**62.5**	**19.4**	**13.2**	**1.47**
202.6	22	10	62.5	45.8	30.1	1.52
202.6	41	10	62.5	37.1	26.2	1.42
202.6	55	10	62.5	33.7	19.5	1.73
202.6	74	10	62.5	29.7	14.6	2.03
303.9	22	10	62.5	47	34.6	1.36
303.9	41	10	62.5	40.5	26.5	1.52
303.9	55	10	62.5	35.5	22.1	1.61
303.9	74	10	62.5	34.4	17.8	1.93

Kim et al. [38]
Base Substrate: Copper; Fluid FC-72; Alumina particles; ABM coating: Aluminum Devcon Brushable Ceramic with Methyl Ethyl Ketone.

Surface	Diameter (μm)	Thickness (μm)	CHF (kW/m^2)	ratio
Plain			17.63	1.00
#1	3-4.5	20	19.88	1.13
#2	4.5-10	30	26.00	1.47
#3	8-12.0	50	26.00	1.47
#4	10-14.0	60	19.88	1.13
#5	17-30	120	22.06	1.25

Chang and You [34]
Base Heater: Copper, Liquid: FC-72; Coating method: Different epoxy solutions.

Coating	Diameter (μm)	Thickness (μm)	Porosity	CHF (kW/m^2)	Ratio
Plain			0	12	1.00
Aluminum Particle	10	50	0.48	26.30	2.19
Copper	25	100	0.41	26.80	2.23
Diamond	10	50	0.4	24.00	2.00
Diamond	10	50	0.4	29.90	2.49
Silver	7	30	0.47	27.00	2.25

Golobic and K. Ferjancic [92]
Heater: Stainless Steel; Fluid: FC-72; Coating method: epoxy solution and copolymer

Coating	Diameter (μm)	Thickness (μm)	CHF (kW/m^2)	Ratio
Plain			118	1.00
Aluminum	10-100	50	170	1.44
Carbon, BaSO4,	14	50	168	1.42
Zn and ZnO	25	50	198	1.68
ZnO and CuO	45	50	222	1.88

Chen and Lu [104]
Fluid: water; Coating method: Electronless etching and electroplating

Surface	Thickness (μm)	Wire size (nm)	porosity	CHF (W/cm^2)	ratio
coating - Si nanowire	40	200	50%	192	2.34
coating -Cu nanowire	40	200	50%	197	2.40
plain surface				82	1.00

Phillips [81]
Heater: Indium Tin Oxide, Fluid: water; LBL coating

Surface	Thickness (μm)	Diameter (nm)	porosity	CHF (W/cm^2)	Ratio
Plain				907	1.00
1	240	7	0.39	109.6	1.21
2	500	50	0.59	158.3	1.74
3	1360	50	0.49	186.7	2.06
4	990	100	0.57	138.2	1.52
5	NA	50	NA	192.3	2.12

Li - Peterson [47]
Fluid: water; Particle: copper; Method: Sintering particle onto surface

	Diameter (μm)	thickness (μm)	CHF (W/cm^2)	Ratio
Uniform	250	550	227	1.61
Uniform	250	1200	290	2.05
Modulated	250	550	435	3.08
Plain			141.3	1.00

Li - Peterson [105]
Base substrate: Copper ; Fluid: water; Particle: Copper mesh screen; sintered to heater block

Surface	wire mesh (μm)	thickness (mm)	porosity	CHF (W/cm^2)	Ratio
1	119.2	0.21	0.737	175	1.25
2	119.2	0.37	0.693	180	1.29
3	119.2	0.57	0.701	220	1.57
4	119.2	0.74	0.698	210	1.50
5	119.2	1.38	0.69	350	2.50
6	119.2	2.3	0.64	330	2.36
Plain	0	0	0	140	1.00

Hwang & Kaviany [41]
Base Substrate: copper; Fluid: Pentane; Particle: copper; Coating method: Brazing

Surface	Diameter(μm)	Thickness(μm)	Porosity	CHF(W/m^2)	ratio
Plain				215	1
1	80	400	0.4	412	1.68
2	200	600	0.4	480	1.96
3	50	250	0.4	454	1.85
4	60	180	0.4	441	1.8
5	60	300	0.4	467	1.9
6	40	160	0.4	430	1.75
7	40	120	0.4	464	1.89
8	40	120	0.4	454	1.85
9	40	160	0.4	398	1.62

Pivovar [106]
Base substrate: Copper; Fluid: water ; Particle: copper; Coating method: Brazing at high temperature

Surface	Diameter(μm)	Thickness(μm)	CHF(W/m^2)	ratio
1	4	90	103	1.27
2	4	130	115	1.42
3	4	180	114	1.41
4	4	210	114	1.41
5	70	180	148	1.83
6	70	230	145	1.79
7	70	280	145	1.79
8	70	320	160	1.98
9	70	420	178	2.20
10	70	510	141	1.74
11	70	660	82	1.01
12	285	380	160	1.98
13	285	420	193	2.38
14	285	590	249	3.07
plain			81	1.00

Im et al. [102]

Liquid: FC-72; Material: Copper nanowire; Method: Electrochemically assisted grown wire and then using epoxy to attach to bare surface.

Surface	Diameter (nm)	Thickness (μm)	CHF (W/cm^2)	Ratio
1	200	1	17.1	1.49
2	200	2	19.5	1.70
3	200	4	18.2	1.58
4	200	8	12.5	1.09
Plain	0	0	11.5	1.00

Tehver et al. [107]
Base Substrate: Copper Rod; Fluid: F113; Coating method: Plasma Spray. Particle materials

Substrate		Material	Thickness (μm)	Porosity	pore radius (μm)	CHF (kW/m^2)	Ratio
Plain						212.3	1.00
1	AB	Al - Bronze	0.09	0.17	2.6	267	1.26
2	AB		0.03	0.18	1.6	261	1.23
3	AB		0.1	0.28	4.2	261	1.23
4	AB		0.08	0.28	2.9	307	1.45
5	AB		0.11	0.29	3	294	1.38
6	AB		0.05	0.2	2	289	1.36
7	AB		0.06	0.29	2.5	328	1.54
8	AB		0.05	0.18	1.8	296	1.39
9	AB		0.06	0.27	2.1	266	1.25
10	AB		0.16	0.5	6	345	1.63
11	AB		0.25	0.47	4.7	356	1.68
12	AB		0.5	0.44	5.8	364	1.71
13	AB		0.03	0.44	3.1	340	1.60
14	AB		0.03	0.36	3.2	320	1.51
15	AB		0.09	0.41	4	300	1.41
16	AB		0.15	0.59	5.1	312	1.47
17	AB		0.22	0.61	7.5	300	1.41
18	AB		0.1	0.53	12.7	284	1.34
19	AB		0.2	0.19	2.6	292	1.38
20	AB		0.25	0.14	3.6	287	1.35
21	AB		0.05	0.25	2.4	282	1.33
22	AB		0.08	0.44	3.9	327	1.54

23	AB		0.2	0.29	2.5	295	1.39
24	AB		0.1	0.24	1.8	242	1.14
25	AB		0.28	0.16	5.5	300	1.41
26	AB		0.12	0.08	1.6	291	1.37
27	CB	Copper Bronze	0.25	0.5	7.3	392	1.85
28	CB		0.07	0.3	4.6	300	1.41
29	CB		0.08	0.31	2.3	316	1.49
30	CB		0.12	0.49	5.2	400	1.88
31	CB		0.25	0.29	4	377	1.78
32	CB		0.07	0.33	3.4	292	1.38
33	CB		0.22	0.3	2.3	315	1.48
34	CB		0.6	0.4	2.5	270	1.27
35	CB		0.3	0.41	2.8	315	1.48
36	AC	Aluminum - Copper	0.13	0.3	4.1	318	1.50
37	AC		0.17	0.44	5.6	338	1.59
38	AC		0.12	0.44	4	308	1.45
39	AC		0.08	0.2	2.5	275	1.30
40	AC		0.1	0.41	6.4	341	1.61
41	AC		0.45	0.3	3	313	1.47
42	AC		0.2	0.1	1.8	276	1.30
43	AC		0.3	0.25	2.6	267	1.26
44	AC		0.4	0.16	2	274	1.29
45	AC		0.12	0.05	1.6	284	1.34
46	AC		0.16	0.05	1	268	1.26
47	AC		0.06	0.12	1.8	276	1.30
48	AC		0.4	0.11	1.6	273	1.29
49	AC		0.06	0.1	1.7	250	1.18
50	AC		0.13	0.05	2	238	1.12
51	AC		0.02	0.05	1.6	228	1.07
52	AC		0.12	0.34	9.2	287	1.35
53	AC		0.08	0.19	6	289	1.36
54	AC		0.12	0.22	5.1	297	1.40
55	AC		0.15	0.37	9	345	1.63
56	AC		0.07	0.37	8.8	247	1.16
57	AC		0.15	0.22	5.8	296	1.39
58	AC		0.1	0.25	6	275	1.30
59	AC		0.15	0.33	8.9	316	1.49
60	AC		0.06	0.16	4.2	246	1.16
61	AC		0.1	0.47	8	293	1.38
62	AC		0.03	0.32	2.5	290	1.37
63	AC		0.08	0.27	4.4	298	1.40

64	AC		0.25	0.48	8.7	322	1.52
65	AC		0.35	0.42	10.8	311	1.46
66	AC		0.4	0.57	15.2	420	1.98
67	AC		0.55	0.52	15.7	383	1.80
68	AC		0.15	0.28	5	415	1.95
69	AC		0.12	0.34	5.3	267	1.26
70	AC		0.15	0.36	7.2	344	1.62
71	AC		0.2	0.32	3.5	377	1.78
72	AC		0.25	0.48	7.9	400	1.88
73	AC		0.18	0.41	5	381	1.79
74	AC		0.2	0.44	6.7	377	1.78
75	AC		0.3	0.52	11.6	406	1.91
76	AC		0.35	0.58	14.2	384	1.81
77	AC		0.13	0.33	10	290	1.37
78	AC		0.17	0.49	14.4	282	1.33
79	CC	copper-copper	0.08	0.25	2.9	300	1.41
80	CC		0.1	0.37	4.4	334	1.57
81	CC		0.17	0.5	5.6	384	1.81
82	AA	Al - Al	0.15	0.1	6.8	280	1.32
83	AA		0.12	0.25	14	285	1.34
84	AA		0.14	0.22	2.7	293	1.38
85	AA		0.25	0.21	4.1	309	1.46
86	AA		0.11	0.1	2.2	279	1.31
87	AA		0.12	0.12	2.1	293	1.38
88	AA		0.03	0.06	2.8	283	1.33
89	AA		0.18	0.1	3.5	328	1.54
90	AA		0.05	0.33	3.7	344	1.62
91	AA		0.05	0.22	2.7	298	1.40
92	AA		0.2	0.29	3.2	314	1.48
93	AA		0.07	0.35	3.5	374	1.76
94	AA		0.12	0.55	8.3	253	1.19
95	AA		0.4	0.32	11.1	440	2.07

Appendix C. Derivation of Equations

In this appendix, derivations of important equations in different chapters are shown.

Inner wall temperature for flow boiling experiment in Chapter 2:

The heat conduction equation in cylindrical coordinate for the test section in Chapter 2 is as follow:

$$\frac{1}{r}\frac{d}{dr}kr\frac{dT}{dr} = q'''$$

where r, k, T and q''' are the radius, thermal conductivity, temperature and volumetric heat generation. Integration provides

$$\boldsymbol{kr\frac{dT}{dr} = \frac{q'''r^2}{2} + C_1}$$

Applying the first boundary condition, no heat loss at outer surface.

$$\left(k\frac{dT}{dr}\right)_{r_o} = 0$$

$$0 = \frac{q'''r_o^2}{2} + C_1$$

$$C_1 = -\frac{q'''r_o^2}{2}$$

$$kr\frac{dT}{dr} = \frac{q'''r^2}{2} - \frac{q'''r_o^2}{2}$$

$$dT = \left(\frac{1}{k}\frac{q'''r}{2} - \frac{1}{k}\frac{q'''r_o^2}{2r}\right)dr$$

$$\boldsymbol{T(r) = \left(\frac{1}{k}\frac{q'''r^2}{4} - \frac{1}{k}\frac{q'''r_o^2}{2}\ln(r)\right) + C_2}$$

Applying the second boundary condition, $T(r_o) = T_{wo}$

$$T_{wo} = \left(\frac{1}{k}\frac{q'''r_o^2}{4} - \frac{1}{k}\frac{q'''r_o^2}{2}\ln(r_o)\right) + C_2$$

$$T_{wo} - \left(\frac{1}{k}\frac{q'''r_o^2}{4} - \frac{1}{k}\frac{q'''r_o^2}{2}\ln(r_o)\right) = C_2$$

$$T(r) = \left(\frac{1}{k}\frac{q'''r^2}{4} - \frac{1}{k}\frac{q'''r_o^2}{2}\ln(r)\right) + T_{wo} - \left(\frac{1}{k}\frac{q'''r_o^2}{4} - \frac{1}{k}\frac{q'''r_o^2}{2}\ln(r_o)\right)$$

$$T(r) = \left(\frac{1}{k}\frac{q'''(r_o^2 - r^2)}{4} + \frac{1}{k}\frac{q'''r_o^2}{2}\ln\left(\frac{r_o}{r_i}\right)\right) + T_{wo}$$

$$\boldsymbol{T(r_i) = \left(\frac{1}{k}\frac{q'''(r_o^2 - r_i^2)}{4} + \frac{1}{k}\frac{q'''r_o^2}{2}\ln\left(\frac{r_o}{r_i}\right)\right) + T_{wo}}$$

The heat flux can be obtained from the volumetric heat generation at:

$$q'''LA_c = q"A_s$$

$$q'''L\pi(r_o^2 - r_i^2) = q"L2\pi r_i$$

$$q''' = \frac{2q"r_i}{r_o^2 - r_i^2}$$

Substitution and simplification:

$$T(r_i) = \left(\frac{1}{k}\frac{\frac{2q"r_i}{r_o^2 - r_i^2}(r_o^2 - r_i^2)}{4} + \frac{1}{k}\frac{\frac{2q"r_i}{r_o^2 - r_i^2}r_o^2}{2}\ln\left(\frac{r_o}{r_i}\right)\right) + T_{wo}$$

$$T(r_i) = \left(\frac{1}{k}\frac{q"r_i}{2} + \frac{1}{k}\frac{\frac{2q"r_i}{r_o^2 - r_i^2}r_o^2}{2}\ln\left(\frac{r_o}{r_i}\right)\right) + T_{wo}$$

$$T(r_i) = \left(\frac{1}{k}\frac{q"r_i}{2} + \frac{1}{k}q"r_i\frac{r_o^2}{r_o^2 - r_i^2}\ln\left(\frac{r_o}{r_i}\right)\right) + T_{wo}$$

$$T(r_i) = \frac{1}{k}q"r_i\left(\frac{1}{2} + \frac{r_o^2}{r_o^2 - r_i^2}\ln\left(\frac{r_o}{r_i}\right)\right) + T_{wo}$$

$$T(r_i) = \frac{1}{k}q"r_i\left(\frac{1}{2} + \frac{r_o^2}{r_o^2 - r_i^2}\ln\left(\frac{r_o}{r_i}\right)\right) + T_{wo}$$

$$T(r_i) = T_{wo} - \frac{1}{k}q"r_i\left(\frac{r_o^2}{r_o^2 - r_i^2}\ln\left(\frac{r_o}{r_i}\right) - \frac{1}{2}\right)$$

$$T(r_i) = T_{wo} - \frac{1}{k}q"r_i\left(\frac{r_o^2}{r_o^2 - r_i^2}\ln\left(\frac{r_o}{r_i}\right) - \frac{1}{2}\right)$$

$$T(r_i) = T_{wo} - \frac{1}{k}q"r_i\left(\frac{r_o^2}{r_i^2 - r_o^2}\ln\left(\frac{r_i}{r_o}\right) - \frac{1}{2}\right)$$

$$T(r_i) = T_{wo} - \frac{q'' D_i}{k2}\left(\frac{D_o^2}{D_i^2 - D_o^2}\ln\left(\frac{D_i}{D_o}\right) - \frac{1}{2}\right)$$

This is equation (2-4) in Chapter 2.

Macrolayer CHF Model Final Equation:

The CHF for an infinite flat place can be calculated using heat balance

$$\tau_d q''_{max} A_w = \rho_l \delta_c (A_w - A_v) h_{fg}$$

where τ_d is the hovering time, δ_c is the thickness of the macrolayer, and $A_w$and A_v are the area of liquid and vapor, respectively. The macrolayer thickness, δ_c, can be assumed to be approximately one-fourth of the critical wavelength, λ_H for Helmholtz instability

$$\delta_c = \frac{\lambda_H}{4} = \frac{\pi}{2}\sigma\frac{(\rho_l + \rho_v)}{\rho_l \rho_v}\left(\frac{A_v}{A_w}\right)^2\left(\frac{\rho_v h_{fg}}{q''}\right)^2$$

The hovering time for a bubble with volumetric flow rate, v_1, is defined as

$$\tau_d = \left(\frac{3}{4\pi}\right)^{\frac{1}{5}}\left[\frac{4(\xi\rho_l + \rho_v)}{(\rho_l - \rho_v)g}\right]^{\frac{3}{5}}(v_1)^{\frac{1}{5}}$$

with ξ is the volumetric ratio of the liquid to the moving bubble, which was estimated as $\frac{11}{16}$ in the model. The volumetric flow rate, v_1, of the bubble is defined as

$$v_1 = \frac{\lambda^2 q}{\rho_v h_{fg}}$$

Substitutions of the above 3 equations and simplification as below will provide:

$$\left(\frac{3}{4\pi}\right)^{\frac{1}{5}}\left[\frac{4(\xi\rho_l + \rho_v)}{(\rho_l - \rho_v)g}\right]^{\frac{3}{5}}\left(\frac{\lambda^2 q}{\rho_v h_{fg}}\right)^{\frac{1}{5}} q''_{max} A_w = \rho_l \frac{\pi}{2}\sigma\frac{(\rho_l + \rho_v)}{\rho_l \rho_v}\left(\frac{A_v}{A_w}\right)^2\left(\frac{\rho_v h_{fg}}{q''}\right)^2 (A_w - A_v) h_{fg}$$

Bringing all the term q to the LHS

$$\left(\frac{3}{4\pi}\right)^{\frac{1}{5}}\left[\frac{4(\xi\rho_l + \rho_v)}{(\rho_l - \rho_v)g}\right]^{\frac{3}{5}}\left(\frac{\lambda^2}{\rho_v h_{fg}}\right)^{\frac{1}{5}} q^{\frac{16}{5}} A_w = \rho_l \frac{\pi}{2}\sigma\frac{(\rho_l + \rho_v)}{\rho_l \rho_v}\left(\frac{A_v}{A_w}\right)^2\left(\frac{\rho_v h_{fg}}{1}\right)^2 (A_w - A_v) h_{fg}$$

Combining the term $\rho_v h_{fg}$

$$\left(\frac{3}{4\pi}\right)^{\frac{1}{5}}\left[\frac{4(\xi\rho_l + \rho_v)}{(\rho_l - \rho_v)g}\right]^{\frac{3}{5}}\left(\frac{\lambda^2}{1}\right)^{\frac{1}{5}}\frac{1}{(\rho_v h_{fg})^{\frac{16}{5}}} q^{\frac{16}{5}} A_w \rho_v = \rho_l \frac{\pi}{2}\sigma\frac{(\rho_l + \rho_v)}{\rho_l \rho_v}\left(\frac{A_v}{A_w}\right)^2 (A_w - A_v)$$

Moving all constant to the RHS

$$\left(\frac{12\pi^2\sigma}{(\rho_v-\rho_l)g}\right)^{\frac{1}{5}}\left(\frac{q}{\rho_v h_{fg}}\right)^{\frac{16}{5}}A_w\rho_v=\frac{1}{\left(\frac{3}{4\pi}\right)^{\frac{1}{5}}}\left[\frac{4(\xi\rho_l+\rho_v)}{(\rho_l-\rho_v)g}\right]^{\frac{5}{3}}\rho_l\frac{\pi}{2}\sigma\frac{(\rho_l+\rho_v)}{\rho_l\rho_v}\left(\frac{A_v}{A_w}\right)^2(A_w-A_v)$$

$$\left(\frac{\sigma}{(\rho_v-\rho_l)g}\right)^{\frac{4}{5}}\left(\frac{q}{\rho_v h_{fg}}\right)^{\frac{16}{5}}A_w\rho_v$$

$$=\frac{1}{(12\pi^2)^{\frac{1}{5}}\left(\frac{3}{4\pi}\right)^{\frac{1}{5}}}\left[\frac{4(\xi\rho_l+\rho_v)}{1}\right]^{\frac{5}{3}}\rho_l\frac{\pi}{2}\frac{(\rho_l+\rho_v)}{\rho_l\rho_v}\left(\frac{A_v}{A_w}\right)^2(A_w-A_v)$$

Simplification of constant

$$\left(\frac{\sigma}{(\rho_v-\rho_l)g}\right)^{\frac{4}{5}}\left(\frac{q}{\rho_v h_{fg}}\right)^{\frac{16}{5}}=\frac{\frac{1}{(9\pi)^{\frac{1}{5}}}\left[\frac{4(\xi\rho_l+\rho_v)}{1}\right]^{\frac{5}{3}}\rho_l\frac{\pi}{2}\frac{(\rho_l+\rho_v)}{\rho_l\rho_v}\left(\frac{A_v}{A_w}\right)^2(A_w-A_v)}{A_w\rho_v}$$

Solving for q and simplification

$$\frac{\left(\frac{q}{\rho_v h_{fg}}\right)}{\left(\frac{\sigma}{(\rho_v-\rho_l)g}\right)^{\frac{1}{4}}}=\left(\frac{\frac{1}{(12\pi^2)^{\frac{1}{5}}\left(\frac{3}{4\pi}\right)^{\frac{1}{5}}}\frac{\pi}{2}4^{\frac{5}{3}}\left[\frac{4(\xi\rho_l+\rho_v)}{1}\right]^{\frac{5}{3}}\rho_l\frac{(\rho_l+\rho_v)}{\rho_l\rho_v}\left(\frac{A_v}{A_w}\right)^2(A_w-A_v)}{A_w\rho_v}\right)^{\frac{5}{16}}$$

$$\frac{\left(\frac{q}{\rho_v h_{fg}}\right)}{\left(\frac{\sigma}{(\rho_v-\rho_l)g}\right)^{\frac{1}{4}}}=\left(\frac{\frac{1}{(9\pi)^{\frac{1}{5}}}\frac{\pi}{2}4^{\frac{5}{3}}\left[\frac{(\xi\rho_l+\rho_v)}{1}\right]^{\frac{5}{3}}\rho_l\frac{(\rho_l+\rho_v)}{\rho_l\rho_v}\left(\frac{A_v}{A_w}\right)^2(A_w-A_v)}{A_w\rho_v}\right)^{\frac{5}{16}}$$

$$\frac{\left(\frac{q}{\rho_v h_{fg}}\right)}{\left(\frac{\sigma}{(\rho_v-\rho_l)g}\right)^{\frac{1}{4}}} = \left(\frac{1}{(9\pi)^{\frac{1}{5}}}\frac{\pi}{2}\left[\frac{(\xi\rho_l+\rho_v)}{1}\right]^{\frac{5}{3}}\left(\frac{\rho_l}{\rho_v}+1\right)\left(\frac{A_v}{A_w}\right)^2\left(1-\frac{A_v}{A_w}\right)\right)^{\frac{5}{16}}$$

$$\frac{\left(\frac{q}{\rho_v h_{fg}}\right)}{\left(\frac{\sigma}{(\rho_v-\rho_l)g}\right)^{\frac{1}{4}}} = \left(\frac{1}{(9\pi)^{\frac{1}{5}}}\frac{\pi}{2}\left[\frac{4\left(\frac{\xi\rho_l}{\rho_v}+1\right)}{1}\right]^{\frac{5}{3}}\left(\frac{\rho_l}{\rho_v}+1\right)\left(\frac{A_v}{A_w}\right)^2\left(1-\frac{A_v}{A_w}\right)\right)^{\frac{5}{16}}$$

$$\frac{\left(\frac{q}{\rho_v h_{fg}}\right)}{\left(\frac{\sigma}{(\rho_v-\rho_l)g}\right)^{\frac{1}{4}}} = \frac{1}{(9)^{\frac{1}{16}}}\frac{\pi^{\frac{1}{4}}}{2^{\frac{1}{16}}}\left(\frac{A_v}{A_w}\right)^{\frac{5}{8}}\left(1-\frac{A_v}{A_w}\right)^{\frac{5}{16}}\left(\frac{\rho_l}{\rho_v}+1\right)^{\frac{5}{16}}\left[4\left(\frac{\xi\rho_l}{\rho_v}+1\right)\right]^{\frac{3}{16}}$$

$$\frac{\left(\frac{q}{\rho_v h_{fg}}\right)}{\left(\frac{\sigma}{(\rho_v-\rho_l)g}\right)^{\frac{1}{4}}} = \frac{1}{(9)^{\frac{1}{16}}}\frac{\pi^{\frac{1}{4}}}{2^{\frac{1}{16}}}\left(\frac{A_v}{A_w}\right)^{\frac{5}{8}}\left(1-\frac{A_v}{A_w}\right)^{\frac{5}{16}}\left(\frac{\rho_l}{\rho_v}+1\right)^{\frac{5}{16}}\left(\xi\frac{\rho_l}{\rho_v}+1\right)^{\frac{3}{16}}$$

One obtained the final expression for CHF, as in equation **(5-10)**

$$\frac{\left(\frac{\boldsymbol{q}}{\boldsymbol{\rho_v h_{fg}}}\right)}{\left(\frac{\boldsymbol{\sigma}}{\boldsymbol{(\rho_v-\rho_l)g}}\right)^{\frac{1}{4}}} = \left(\frac{\boldsymbol{\pi^4}}{\mathbf{18}}\right)^{\frac{1}{16}}\left(\frac{\boldsymbol{A_v}}{\boldsymbol{A_w}}\right)^{\frac{5}{8}}\left(\mathbf{1}-\frac{\boldsymbol{A_v}}{\boldsymbol{A_w}}\right)^{\frac{5}{16}}\left(\frac{\boldsymbol{\rho_l}}{\boldsymbol{\rho_v}}+\mathbf{1}\right)^{\frac{5}{16}}\left(\boldsymbol{\xi}\frac{\boldsymbol{\rho_l}}{\boldsymbol{\rho_v}}+\mathbf{1}\right)^{\frac{3}{16}}$$

The Lu & Chang [100] Model (adapted from Udell Model [99]):

Assumptions on Model:

Porous layer is a fixed bed of particles.
Heating is from the bottom based surface
Permeability equations applicable in both laminar and turbulent flow
Porosity: 0.5 - 0.6
Average particle size: d_p
Dryout heat flux: heat flux at which relative liquid saturation at heater surface is 0.

Pressure drop of flow in tube of diameter D

$$\tau_w = -\frac{\Delta P}{L}\frac{D}{4} = f\rho u_l^2 \tag{31}$$

$\tau_w \equiv$ wall shear stress
$P \equiv$ pressure
$L \equiv$ Length
$D \equiv$ diameter
$f \equiv$ friction factor
$\rho \equiv$ density
$u_l \equiv$ liquid velocity

For a porous layer, the diameter is the effective pore diameter, D/4 is defined as

$$d'_m = \frac{e}{s(1-e)}$$

where
$s \equiv$ specific surface area
$e \equiv$ porosity

Ergun equation for friction factor

$$f = \frac{4.17}{Re_l} + 0.29 \quad where \;\; Re_l = \frac{\left[\frac{e}{s(1-e)}\right] u_l}{\nu} \tag{32}$$

this is only valid for

$$1 < \frac{Re_l}{1-e} < 2000$$

substitute for equation (32) in equation (31)**Error! Reference source not found.** and using pore diameter, one gets

$$\tau_w = -\frac{\Delta P}{L}\frac{\frac{e}{s(1-e)}}{4} = \left(\frac{4.17}{Re_l} + 0.29\right)\rho u_l^2$$

$$\tau_w = -\frac{\Delta P}{L}\frac{\frac{e}{s(1-e)}}{1} = \left(\frac{4.17}{\frac{\left[\frac{e}{s(1-e)}\right]u_l}{\nu}} + 0.29\right)\rho u_l^2$$

$$-\frac{\Delta P}{L} = \frac{1}{\frac{e}{s(1-e)}}\left(\frac{4.17}{\frac{\left[\frac{e}{s(1-e)}\right]u_l}{\nu}} + 0.29\right)\rho u_l^2$$

$$-\frac{\Delta P}{L} = \frac{s(1-e)}{e}\left(\frac{4.17\nu\rho}{\left[\frac{e}{s(1-e)}\right]u_l} + 0.29\right)\rho u_l^2$$

$$-\frac{\Delta P}{L} = \frac{s(1-e)}{e}\left(\frac{4.17\nu\rho s(1-e)}{eu_l} + 0.29\right)\rho u_l^2$$

$$-\frac{\Delta P}{L} = \frac{4.17\nu\rho s^2(1-e)^2}{e^2 u_l} + 0.29\frac{4s(1-e)}{e}\rho u_l^2$$

let $u = u_l e$ superficial velocity

$$-\frac{\Delta P}{L} = \frac{4.17\nu\rho u s^2(1-e)^2}{e^3} + 0.29\frac{s(1-e)}{e^3}\rho u^2$$

$$-\frac{\Delta P}{L} = \frac{u\mu}{\frac{36e^3}{150[s^2(1-e)^2]}} + \frac{1.75}{6}\frac{s(1-e)}{e^3}\rho u^2$$

$$-\frac{\Delta P}{L} = \frac{\mu}{K}u + \frac{\beta}{K}\rho u^2 \qquad (33)$$

first term is laminar contribution (as in Darcy Law), the second term is turbulent distribution

$\beta = \frac{1.75 d_p}{150(1-e)}$

$K = \frac{d_p^2 e^3}{150(1-e)^2}$ permeability

substitute K and β back into (33) to check if this is correct.

$$-\frac{\Delta P}{L} = \frac{\mu u}{\frac{d_p^2 e^3}{150(1-e)^2}} + \frac{\frac{1.75 d_p}{150(1-e)}}{\frac{d_p^2 e^3}{150(1-e)^2}}\rho u^2$$

$$-\frac{\Delta P}{L}=\frac{\mu u}{\frac{d_p^2 e^3}{150(1-e)^2}}+\frac{\frac{1.75 d_p}{150(1-e)}}{\frac{d_p^2 e^3}{150(1-e)^2}}\rho u^2$$

$$\boxed{-\frac{\Delta P}{L}=\frac{\mu u}{\frac{d_p^2 e^3}{150(1-e)^2}}+\frac{1.75(1-e)}{d_p e^3}\rho u^2}$$ this is not the same as (33)

unless $d_p=\frac{6}{s}$ which makes senses for sphere. s is the specific area = Area/Volume $=\frac{4\pi R^2}{\frac{4}{3}\pi R^3}=\frac{3}{R}=\frac{6}{D}$

Equation (33) can be applied to both vapor and liquid phase

$$-\frac{dP_v}{dy}=\frac{\mu_v}{K_v}u_v+\frac{\beta}{K_v}\rho_v u_v|u_v|+\rho_v g \tag{34}$$

$$-\frac{dP_l}{dy}=\frac{\mu_l}{K_l}u_l+\frac{\beta}{K_l}\rho_l u_l|u_l|+\rho_l g \tag{35}$$

define $P_c=P_v-P_l$ and subtracting (35) from (34), one gets the **capillary pressure** gradient

$$-\frac{dP_c}{dy}=\left(\frac{\mu_v}{K_v}u_v-\frac{\mu_l}{K_l}u_l\right)+\beta\left(\frac{\rho_v u_v|u_v|}{K_v}-\frac{\rho_l u_l|u_l|}{K_l}\right)-(\rho_l-\rho_v)g \tag{36}$$

mass balance requires

$$\rho_l u_l=-\rho_v u_v$$

and the heat flux is

$$q''=\rho_v u_v h_{fg}$$

$$(\rho_l-\rho_v)=\Delta\rho$$

substitute these two equations in (36), one gets,

$$-\frac{dP_c}{dy}=\left(\frac{\nu_v\rho_v}{K_v}u_v+\frac{\nu_l\rho_l}{K_l}u_l\right)+\beta\left(\frac{\rho_v u_v|u_v|}{K_v}-\frac{\rho_v u_v|u_l|}{K_l}\right)-\Delta\rho g$$

$$-\frac{dP_c}{dy}=\rho_v u_v\left(\frac{\nu_l}{K_l}+\frac{\nu_v}{K_v}\right)+\beta\rho_v u_v\left(\frac{|u_v|}{K_v}-\frac{|u_l|}{K_l}\right)-\Delta\rho g$$

$$-\frac{dP_c}{dy}\frac{1}{\Delta\rho g}=\frac{\rho_v u_v}{\Delta\rho g}\left(\frac{\nu_l}{K_l}+\frac{\nu_v}{K_v}\right)+\beta\frac{\rho_v u_v}{\Delta\rho g}\left(-\frac{|u_l|}{K_l}+\frac{|u_v|}{K_v}\right)-1$$

$$-\frac{dP_c}{dy}\frac{1}{\Delta\rho g} = \rho_v \frac{\rho_v}{\Delta\rho g}\frac{q^{"}}{\rho_v h_{fg}}\left(\frac{\nu_l}{K_l}+\frac{\nu_v}{K_v}\right)+\beta\rho_v\frac{\rho_v}{\Delta\rho g}\frac{q^{"}}{\rho_v h_{fg}}\left(-\frac{|u_l|}{K_l}+\frac{|u_v|}{K_v}\right)-1$$

Let $P_{cd}=\frac{P_c}{\Delta\rho g L}$ where L is thickness of porous layer coating.

$y_c=\frac{y}{L}$; $K_{rl}=\frac{K_l}{K}$; $K_{rv}=\frac{K_v}{K}$; $c_\nu=\frac{\nu_l}{\nu_v}$, $c_\rho=\frac{\rho_l}{\rho_v}$,

$$-\frac{dP_{cd}}{dy_d} = \frac{\nu_v q^{"}}{\Delta\rho g h_{fg}}\frac{1}{K}\left(\frac{c_\nu}{Kr_l}+\frac{1}{K_{rv}}\right)+\beta\frac{q^{"}}{\Delta\rho g h_{fg}}\frac{1}{K}\left(-\frac{\rho_l}{\rho_v}\frac{|u_l|}{K_{rl}}\frac{1}{c_\rho}+\frac{\rho_v}{\rho_v}\frac{|u_v|}{K_{rv}}\right)-1$$

$$-\frac{dP_{cd}}{dy_d} = \frac{\nu_v q^{"}}{\Delta\rho g h_{fg}}\frac{1}{K}\left(\frac{c_\nu}{Kr_l}+\frac{1}{K_{rv}}\right)+\beta\frac{q^{"}}{\Delta\rho g h_{fg}}\frac{1}{K}\left(\frac{\rho_v}{\rho_v}\frac{|u_v|}{K_{rl}}\frac{1}{c_\rho}+\frac{\rho_v}{\rho_v}\frac{|u_v|}{K_{rv}}\right)-1$$

let $B=\frac{\nu_v q^{"}}{\Delta\rho g h_{fg}}\frac{1}{K}$

$$-\frac{dP_{cd}}{dy_d} = B\left(\frac{c_\nu}{Kr_l}+\frac{1}{K_{rv}}\right)+\beta\frac{q^{"}}{\Delta\rho g h_{fg}}\frac{1}{K}|u_v|\left(\frac{1}{K_{rl}c_\rho}+\frac{1}{K_{rv}}\right)-1$$

$$-\frac{dP_{cd}}{dy_d} = B\left(\frac{c_\nu}{Kr_l}+\frac{1}{K_{rv}}\right)+\beta\frac{q^{"}}{\Delta\rho g h_{fg}}\frac{1}{K}\frac{q^{"}}{\rho_v h_{fg}}\left(\frac{1}{K_{rl}c_\rho}+\frac{1}{K_{rv}}\right)-1$$

let $\psi=\frac{\beta K\Delta\rho g}{\rho_v\nu_v^2}$

$B^2\psi=\left(\frac{\nu_v q^{"}}{\Delta\rho g h_{fg}}\frac{1}{K}\right)\left(\frac{\nu_v q^{"}}{\Delta\rho g h_{fg}}\frac{1}{K}\right)\frac{\beta K\Delta\rho g}{\rho_v\nu_v^2}=\beta\left(\frac{q^{"}}{\Delta\rho g h_{fg}}\frac{1}{K}\right)\frac{q^{"}}{h_{fg}\rho_v}$. Therefore, we have

$$-\frac{dP_{cd}}{dy_d} = B\left(\frac{c_\nu}{Kr_l}+\frac{1}{K_{rv}}\right)+B^2\psi\left(\frac{1}{K_{rl}c_\rho}+\frac{1}{K_{rv}}\right)-1 \qquad (37)$$

$K_{rl}=Se^n$; $K_{rv}=(1-Se)^2(1-Se^m)$ where $n=3+\frac{2}{\lambda}$ and $m=1+\frac{2}{\lambda}$ and λ is the index of pore size distribution, which is experimentally determined. Here S_e is the relative saturation, which can be related to the absolute saturation S, maximum saturation S_m and S_r, residual saturation as $s_e=\frac{S-S_r}{S_m-S_r}$, where saturation is defined as *fraction of volume occupied by wetting phase/porosity*

Udell Model [99]

Udell proposed

$$\boldsymbol{L_d P_{cd}} = \frac{\boldsymbol{P_c}}{\boldsymbol{\sigma}}\sqrt{\frac{\boldsymbol{\kappa}}{\boldsymbol{e}}} = \boldsymbol{f(S_e)} \tag{38}$$

$$f(Se) = a(1-S_e) - b(1-S_e)^2 + c(1-S_e)^3$$

$$L_d = \frac{\Delta\rho g L}{\sigma}\sqrt{\frac{K}{e}}$$

where *a, b, c* are empirical constants.
Substitute (38) in to (37), one have

$$-\frac{d(\frac{f(S_e)}{L_d})}{B\left(\frac{c_v}{Kr_l}+\frac{1}{K_{rv}}\right)+B^2\psi\left(\frac{1}{K_{rl}c_\rho}+\frac{1}{K_{rv}}\right)-1} = dy_d$$

$$\frac{d(a(1-S_e)-b(1-S_e)^2+c(1-S_e)^3)}{B\left(\frac{c_v}{Kr_l}+\frac{1}{K_{rv}}\right)+B^2\psi\left(\frac{1}{K_{rl}c_\rho}+\frac{1}{K_{rv}}\right)-1} = L_d dy_d$$

$$\frac{(a-2b(1-Se)+3c(1-S_e)^2)}{B\left(\frac{c_v}{Kr_l}+\frac{1}{K_{rv}}\right)+B^2\psi\left(\frac{1}{K_{rl}c_\rho}+\frac{1}{K_{rv}}\right)-1}dSe = L_d dy_d$$

$$\int_{S_{e_0}}^{S_e}\frac{(\boldsymbol{a-2b(1-Se)+3c(1-S_e)^2})}{\boldsymbol{B\left(\frac{c_v}{Kr_l}+\frac{1}{K_{rv}}\right)+B^2\psi\left(\frac{1}{K_{rl}c_\rho}+\frac{1}{K_{rv}}\right)-1}}\boldsymbol{dS_e} = \int_0^{y_d}\boldsymbol{L_d dy_d} = \boldsymbol{L_d y_d} \tag{39}$$

$S_{e_0} = 0$ indicates dry out. S_e limit is 0. One needs to find S_e at $\boldsymbol{L_d}$

The following method was used to fine S_{e_L}

$$P_c = \frac{4\sigma}{d} \tag{40}$$

where d is twice the radius of the meniscus curvature at that point. Substitute (40)into (38) and using the definition of κ, one gets

$$\frac{4\sigma}{d}\frac{1}{\sigma}\sqrt{\frac{d_p^2 e^3}{150(1-e)^2}} = f(S_e)$$

$$\frac{d_p e}{1-e}\frac{4}{d}\frac{1}{\sqrt{150}} = f(S_e)$$

$$\frac{\boldsymbol{d}}{\boldsymbol{d_p}} = \frac{\boldsymbol{4}}{\sqrt{\boldsymbol{150}}\boldsymbol{f(S_e)}} \frac{\boldsymbol{e}}{\boldsymbol{1-e}} \tag{41}$$

Reynolds number for vapor and liquid flow using true velocity is

$$Re_{l,v} = \frac{\left[\frac{e}{s(1-e)}\right] u_{l,v}\rho_v}{\mu_v}$$

substitute $s = \frac{6}{d_p}$ and $u_{l,v} = u_v/e$

$$\psi = \frac{\beta K \Delta\rho g}{\rho_v \nu_v^2} = \frac{1.75}{150^2}\left(\frac{d_p e}{1-e}\right)^3 \left(\frac{\Delta\rho g}{\rho_v \nu_v^2}\right) \; ; \qquad B = \frac{\nu_v q^{"}}{\Delta\rho g h_{fg}} \frac{1}{K}$$

$$Re_{l,v} = \frac{\left[\frac{d_p e}{6(1-e)}\right] u_{l,v}\rho_v}{\mu_v}$$

$$Re_{l,v} = B \frac{\left[\frac{d_p e}{d_p(1-e)}\right] u_{l,v}\rho_v}{\mu_v} K * \frac{\Delta\rho g h_{fg}}{\nu_v q^{"}}$$

$$Re_{l,v} = B \frac{\left[\frac{d_p e}{6(1-e)}\right] u_v \rho_v}{\mu_v e} \frac{d_p^2 e^3}{150(1-e)^2} * \frac{\Delta\rho g h_{fg}}{\nu_v q^{"}}$$

$$Re_{l,v} = B \frac{\left[\frac{d_p}{6(1-e)}\right] u_v}{\nu_v} \frac{d_p^2 e^3}{150(1-e)^2} * \frac{\Delta\rho g h_{fg}}{\nu_v q^{"}}$$

$$Re_{l,v} = \left[\frac{B}{6*150}\right] \frac{u_v}{\nu_v} \frac{d_p^3 e^3}{(1-e)^3} * \frac{\Delta\rho g h_{fg}}{\nu_v \rho_v u_v h_{fg}}$$

$$Re_{l,v} = \left[\frac{B}{6*150}\right] \frac{d_p^3 e^3}{(1-e)^3} * \frac{\Delta\rho g}{\rho_v \nu_v^2}$$

$$\boldsymbol{Re_{l,v} = \left[\frac{150}{6*1.75}\right] B\psi}$$

For liquid phase,

$$Re_{l,l} = \frac{\left[\frac{e}{s(1-e)}\right] u_{l,l}\rho_l}{\mu_l}$$

$$Re_{l,v} = \left[\frac{B}{6*150}\right] \frac{d_p^3 e^3}{(1-e)^3} * \frac{\Delta\rho g}{\rho_v \nu_v^2} \left(\frac{\rho_v \nu_v}{\rho_l \nu_l}\right)$$

$$\boldsymbol{Re_{l,l} = \left[\frac{150}{6 * 1.75}\right] B\psi \left(\frac{\rho_v \nu_v}{\rho_l \nu_l}\right)}$$

$$Re_{l,l} = Re_{l,v}\left(\frac{\rho_v \nu_v}{\rho_l \nu_l}\right)$$

$$\int_{Se_0}^{Se} \frac{(a - 2b(1 - Se) + 3c(1 - S_e)^2)}{B\left(\frac{c_v}{Kr_l} + \frac{1}{K_{rv}}\right) + B^2\psi\left(\frac{1}{K_{rl}c_\rho} + \frac{1}{K_{rv}}\right) - 1} dS_e =$$

$$\left.\frac{(a(Se) + b(1 - Se)^2 - c(1 - S_e)^3)}{B\left(\frac{c_v}{Kr_l} + \frac{1}{K_{rv}}\right) + B^2\psi\left(\frac{1}{K_{rl}c_\rho} + \frac{1}{K_{rv}}\right) - 1}\right]_{Se_0}^{Se_L} =$$

$$\frac{(a(Se_L - Se_0) + b[(1 - Se)^2 - (1 - Se_0)\text{^}2] - c[(1 - Se_L)^3 - (1 - Se_0)^3])}{B\left(\frac{c_v}{Kr_l} + \frac{1}{K_{rv}}\right) + B^2\psi\left(\frac{1}{K_{rl}c_\rho} + \frac{1}{K_{rv}}\right) - 1} = L_d y_d$$

CHF/dryout occurs when $Se_0 = 0$

$$\boldsymbol{\frac{(a(Se_L) + b[(1 - Se_L)^2 - 1] - c[(1 - Se_L)^3 - 1])}{B\left(\frac{c_v}{Kr_l} + \frac{1}{K_{rv}}\right) + B^2\psi\left(\frac{1}{K_{rl}c_\rho} + \frac{1}{K_{rv}}\right) - 1} = L_d y_d}$$

For very thick porous layer, L is very larger

$$B\left(\frac{c_v}{Kr_l} + \frac{1}{K_{rv}}\right) + B^2\psi\left(\frac{1}{K_{rl}c_\rho} + \frac{1}{K_{rv}}\right) - 1 = 0$$

Solving for B here, one can get CHF since $\boldsymbol{B = \frac{\nu_v q''}{\Delta\rho g h_{fg}}\frac{1}{K}}$

For laminar flow only (bed with small particles), ψ is equal to 0, $= \frac{1}{\left(\frac{c_v}{Kr_l} + \frac{1}{K_{rv}}\right)}$, which means

$$\boldsymbol{q'' = \frac{\Delta\rho g h_{fg} K}{\nu_v} \frac{1}{\left(\frac{c_v}{Kr_l} + \frac{1}{K_{rv}}\right)}} \quad (42)$$

Remind, $\kappa = \frac{d_p^2 e^3}{150(1-e)^2}$; $\psi = \frac{\beta K \Delta\rho g}{\rho_v \nu_v^2} = \frac{1.75}{150^2}\left(\frac{d_p e}{1-e}\right)^3 \left(\frac{\Delta\rho g}{\rho_v \nu_v^2}\right)$

$$\boldsymbol{q_{dry} = B_{max}\frac{(1 - e)}{d_p}\left(\frac{150}{1.75}\rho_v \nu_v h_{fg} \psi\right)} \quad (43)$$

For highly turbulence flow (large particles), $B\left(\frac{c_v}{Kr_l}+\frac{1}{K_{rv}}\right)\approx 0$, the laminar contribution will be negligible.

$$B\sqrt{\psi}=\left[\frac{1}{\left(\frac{1}{K_{rl}c_\rho}+\frac{1}{K_{rv}}\right)}\right]^{0.5} \tag{44}$$

Writing the dryout heat flux in term of the particle diameter, for the laminar flow case, one gets

$$\log(q_{dry})=\log\left[\frac{\Delta\rho g h_{fg}}{\nu_v}\frac{d_p^2 e^3}{150(1-e)^2}B_{max}\right]$$

$$\log(q_{dry})=\log\left[\frac{B_{max}\Delta\rho g h_{fg}}{150\nu_v}\frac{e^3}{(1-e)^2}\right]+2\log(d_p) \tag{45}$$

For case with turbulent flow,

$$\log(q_{dry})=\log\left[h_{fg}\sqrt{\frac{\rho_v\Delta\rho g h_{fg}}{1.75}\frac{e^3}{(1-e)^2}}B_{max}\sqrt{\psi}\right]+\frac{1}{2}\log(d_p) \tag{46}$$

References:

[1] W. M. Rohsenow, J. P. Hartnett, and Y. I. Cho, "Handbook of Heat Transfer, Chapter 10, 3rd ed., 1998, McGraw-Hill.

[2] S.J. Kim, "Subcooled Boiling Heat Transfer and Critical Heat Flux in Water Based Nanofluids at Low Pressure", PhD. Thesis, MIT, 2009.

[3] B. Truong, " Critical Heat Flux Enhancement via Surface Modification Using Colloidal Dispersions of Nanoparticles (Nanofluids)", Master Thesis, MIT 2008.

[4] S. Choi, "Enhancing thermal conductivity of fluids with nanoparticles". *ASME FED*, **231**, 1995, 99–103.

[5] S. Kakac and A. Pramuanjaroenkij, "Review of Convective Heat Transfer Enhancement with Nanofluids", *Int. J. Heat and Mass Transfer*, **52**, 2009, 3187-3196.

[6] J. Buongiorno, D. C. Venerus, N. Prabhat, T. McKrell, J.Townsend, R.Christianson, Y. V. Tolmachev, P. Keblinski, L.W. Hu, J. L. Alvarado, I.C. Bang, S. W. Bishnoi, M. Bonetti, F Botz, A. Cecere, Y. Chang, G. Chen, H. Chen, S. J. Chung, M. K. Chyu, S. K. Das, R. Di Paola, Y. Ding, F. Dubois, G.Dzido, J. Eapen, W. Escher,D. Funfschilling, Q. Galand, J. Gao, P. E. Gharagozloo, K. E. Goodson, J. G. Gutierrez, H. Hong,M. Horton, K. S. Hwang, C. S. Iorio, S. P. Jang, A. B. Jarzebski, Y. Jiang, L. Jin, S. Kabelac, A. Kamath, M. A. Kedzierski, L.G. Kieng, C. Kim, J. H. Kim, S. Kim, S. H. Lee, K. C. Leong, I. Manna, B. Michel, R. Ni, H. E. Patel,J. Philip, D. Poulikakos, C. Reynaud, R. Savino, P. K. Singh, P. Song, T. Sundararajan, E. Timofeeva, T. Tritcak, A. N. Turanov, S.V. Vaerenbergh, D. Wen, S. Witharana, C. Yang, W. H. Yeh, X.-Z. Zhao, and S.-Q. Zhou, "A Benchmark Study on the Thermal Conductivity of Nanofluids", *J. Applied Physics,* **106**, 2009, 094312.

[7] S. M. You, J. Kim, and K. H. Kim, Effect of nanoparticles on critical heat flux of water in pool boiling heat transfer, *Applied Physics Letters* **83** (16), 2003, 3374-3376.

[8] H. Kim, J. Kim, and M. Kim, Experimental study on CHF characteristics of water-TiO2 nano-fluids, *Nuclear Engineering and Technology* **38** (1), 2006.

[9] P. Vassallo, R. Kumar, and S. D'Amico, Pool boiling heat transfer experiments in silica-water nano-fluids, *Int. J. of Heat and Mass Transfer* **47,** 2004, 407-41.

[10] J. P.Tu, N. Dinh, T. Theofanous, An experimental study of nanofluid boiling heat transfer, Proceedings of 6th International Symposium on Heat Transfer, Beijing, China. 2004.

[11] H. D. Kim and M. H. Kim, Critical heat flux behavior in pool boiling of water-TiO2 nano-fluids, Proceedings of Fourth Japan-Korea Symposium on Nuclear Thermal Hydraulics and Safety, Sapporo, Japan, Nov. 28-Dec 1, 2004.

[12] G. Moreno Jr., S. Oldenburg, S. M. You, and J. H. Kim, Pool Boiling Heat Transfer of Alumina-Water, Zinc Oxide-Water and Alumina-Water Ethylene Glycol Nanofluids, Proceedings of HT2005, San Francisco, California, USA, July 17-22, 2005.

[13] I. C. Bang and S. H. Chang, Boiling Heat Transfer Performance and Phenomena of Al2O3-Water Nano-fluids from a Plain Surface in a Pool, Int. J. of Heat and Mass Transfer, **48**, 2005, 2407-2419.

[14] D. Milanova, R. Kumar, S. Kuchibhatla, S. Seal, Heat transfer behavior of oxide nanoparticles in pool boiling experiment, Proc. of 4th International Conference on Nanochannels, Microchannels and Minichannels, Limerick, Ireland, June 19-21, 2006.

[15] J. E. Jackson, B. V. Borgmeyer, C. A. Wilson, P. Cheng, and J. E. Bryan, Characteristics of nucleate boiling with gold nanoparticles in water, Proceedings of IMECE 2006, Chicago, 2006.

[16] D. Wen and Y. Ding, Experimental Investigation into the Pool Boiling Heat Transfer of Aqueous Based γ-alumina nanofluids, *Journal of Nanoparticle Research* **7**, 2005, 265-284.

[17] S. J. Kim, I. C. Bang, J. Buongiorno, and L. W. Hu, "Surface Wettability Change during Pool Boiling of Nanofluids and its effect on Critical Heat Flux", *Int. J. Heat Mass Transfer* **50,** 2007, 4105-4116.

[18] R. Kathiravan, R. Kumar, A. Gupta and R. Chandra, "Characterization and Pool Boiling Heat Transfer Studies of Nanofluids", *J. Heat Transfer,* **131**, 2009, 81902-1:81902-5.

[19] S.M. Kwark, R.Kumar, G.Moreno, J. Yoo, and S. M. You , " Pool boiling characteristics of low concentration nanofluids", *International Journal of Heat and Mass Transfer*, **53,** 2010, 972–981.

[20] S. D Park, S. W. Lee, S. Kang, I. C. Bang, J. H. Kim, H. S. Shin, D. W. Lee and D. W. Lee, "Effects of Nanofluids Containing Graphene/Graphene-oxide Nanosheets on Critical Heat Flux", *Applied Physics Letters*, **97**, (2010) .023103.

[21] T.I. Kim, Y.H. Jeong, S.H. Chang, "An experimental study on CHF enhancement in flow boiling using Al2O3 nano-fluid", *Int. J. Heat Mass Transfer,* **53,** 2010, 1015–1022.

[22] S. J. Kim, T. McKrell, J. Buongiorno, L. W. Hu, "Experimental Study of Flow Critical Heat Flux in Alumina-Water, Zinc-oxide-Water and Diamond-Water Nanofluids", *ASME J. Heat Transfer*, **131**, 2009, 043204.

[23] Z.-H. Liu and Y.-H. Qui, Boiling Heat Transfer Characteristics of Nanofluids Jet Impingement on a Plate Surface, *J. Heat Mass Transfer*, 43, 699-706 (2007).

[24] H.S Park, D. Shiferaw, B. R. Sehgal, D. K. Kim and M. Muhammed, "Film boiling heat transfer on a high temperature sphere in nanofluid", *In: Proceedings of 2004 ASME Heat Transfer/Fluids Engineering Summer Conference*, Charlotte, NC, pp. 1–8.

[25] S. Y. Chun, I. C. Bang, Y. J. Choo and C. H Song, " Heat Transfer Characteristics of Si and SiC Nanofluids during a Rapid Quenching and Nanoparticle Deposition Effects", *Int. J. Heat Mass Transfer*, **54**, 2011, p.1217-1223.

[26] K. Babu and T. S. P. Kumar, "Effect of CNT Concentration and Agitation on Surface Heat Flux During Quenching in CNT Nanofluids", *Int. J. Heat Mass Transfer*, **54**, 2011, p.106-107.

[27] V. Jagannath and K. N. Prabhu, "Severity of Quenching and Kinetics of Wetting of Nanofluids", *J. ASTM Int*, **6**, 2009, p. 1-9.

[28] H.S. Xue, J.R. Fan, R.H. Hong and Y.C. Hu, Characteristic boiling curve of carbon nanotube nanofluid as determined by the transient calorimeter technique, *Appl. Phys. Lett.* **90,** 2007, p. 184107.

[29] H. Kim, G. DeWitt, T. McKrell, J. Buongiorno, and L.-W. Hu, "On the quenching of steel and zircaloy spheres in water-based nanofluids with alumina, silica and diamond nanoparticles", *Int. J. Multiphase Flow*, **35**(5), 2009, pp. 427-438.

[30] H. Kim, J. Buongiorno, L.-W. Hu, T. McKrell, " Nanoparticle deposition effects on the minimum heat flux point and quench front speed during quenching of rodlets and spheres in water-based alumina nanofluids", *Int. J. Heat Mass Transfer*, **53**, 2010, pp. 1542-1553.

[31] P. L. Berenson, "Film-boiling heat transfer from a horizontal surface", *J. Heat Transfer*, **83**, 1961, pp. 351-358.

[32] R. E. Henry, "A correlation for the minimum film boiling temperature", AIChE Symp. Ser., **70**, No. 138, 1974, pp. 81-90.

[33]B. Palm, "Boiling on Porous Surface", *ECI International Conference on Boiling Heat Transfer*, Florianopolis-SC-Brazil, 3-7, May 2009.

[34] J. Y. Chang and S. M. You, "Boiling Heat Transfer Phenomena from Micro-porous and Porous Surfaces in Saturated FC-72", *Int. J. Heat Mass Transfer*, **40** (18), 1997,4437-4447.

[35] J. Tehver, "Influence of Porous Coating on Boiling Burnout Heat Flux", *Recent Advances in Heat Transfer*, 1992, 231-242

[36] Y. V. Polezhaev and S. A. Kovalev, "Modeling Heat Transfer with Boiling on Porous Structures", *Thermal Engineering,* **37** (12), 1990, 617-620.

[37] G. -S. Hwang and M. Kaviany, "Critical Heat Flux in Thin, Uniform Particle Coatings", *Int. J. Heat and Mass Transfer,* **49**, 2006, p.844-849.

[38] J. H. Kim, S. M. Kwark, M. R. Kashinath and S. M. You, "Optimization of Microporous Structures in Enhancing Pool Boiling Heat Transfer of Saturated R-123, FC-72 and Water", *Proceeding of HT2007*, July8-12, 2007, Vancouver, Canada

[39] M. Arik, A. Bar-Cohen and S. M. You, "Enhancement of Pool Boiling Critical Heat Flux in Dielectric Liquids by Microporous Coating", *Int. J. Heat Mass Transfer*, **50,** 2007, 997-1009.

[40] K. Ferjancic and I. Golobic, "Surface Effect on Pool Boiling CHF", *Exp. Thermal and Fluid Science*, **25**, 2002, 565-571.

[41] J. Yang, M. B. Dizon, J. L. Rempe, K. Y. Suh and S. B. Kim, "CHF Enhancement by Vessel Coating for External Reactor Vessel Cooling" *Proceedings or ICAPP 2004 Pittsburgh, PA USA, June 13-17, 2004.*

[42] S. Vemuri and K. J. Kim, "Pool Boiling of Saturated FC-72 on Nano-porous Surface", *Int. Communication in Heat and Mass Transfer*, **32,** 2005, p. 27-31.

[43] D. H. Min, G. S. Hwang, Y. Usta, O. N. Cora, M. Koc, M. Kaviany, "2-D and 3-D Modulated Porous Coatings for Enhanced Pool Boiling", *Int. J. Heat Mass Transfer*, **52**, 2009, 2607-2613.

[44] O. N. Cora, D. Min, M. Koc and M. Kaviany, "Microscale-modulated Porous Coatings: Fabrication and Pool Boiling Heat Transfer Performance ", *J. Micromech. Microeng.* , **20**, 2010, 03520 (9pp).

[45] E. Melendez and R. Reyes, "The Pool Boiling Heat Transfer Enhancement from Experiments with Binary Mixtures and Porous Heating Cover", *Exp. Thermal and Fluid Science*, **30**, 2006, p. 185-192.

[46] C. H. Li, T. Li and B. Kanney, "Two-Phase Heat Transfer Enhancement on Sintered Copper Microparticle Porous Structure Module Surface", *Proceedings of MNHMT2009*, 18292 Shanghai, China, December 18-21, 2009.

[47] C. H. Li and G. P. Peterson, "Experimental Study of Enhanced Nucleate Boiling Heat Transfer on Uniform and Modulated Porous Structures", *Frontier in Heat and Mass Transfer*, **1**, 2010, 023007.

[48] J. S. Ahn, P. T. Hammond, M. F. Rubner, I. Lee, "Self-assembled particle monolayers on polyelectrolyte multilayers: particle size effects on formation, structure, and optical properties", *Colloids and Surfaces A: Physicochemical and Engineering Aspects*, **259**, Issues 1-3, (2005), 45-53.

[49] E. Forrest, E. Williamson, J. Buongiorno, L.W. Hu, M. Rubner and R. Cohen, "Augmentation of Nucleate Boiling Heat Transfer and Critical Heat Flux Using Nano-particle Thin-Film Coating", *I. J. Heat Mass Transfer*, **53**, (2010), 58-67.

[50] D. C. Groeneveld, J. Q. L.K.H. Leung, P. L. Kirillov, V.P. Bobkov, I. P. Smogalev, V.N. Vinogradov, X.C. Huang and E. Royer, "The 1995 CHF Look-up Table for Critical Heat Flux in Tube", *Nuclear Engineering and Design*, 163, 1-23, 1996.

[51] American Society of Mechanical Engineers (ASME). *Boiler and Pressure Vessel Code*. Case N-47-30, Section III, Division I. 1992.

[52] N. E. Todreas and M. S. Kazimi, "Nuclear System 1", Chapter 12, p.540-543, Taylor & Francis Group, New York, 1990.

[53] S. G. Kandlikar, "A Theoretical Model to Predict Pool Boiling CHF Incorporating Effects on Contact Angle and Orientation", *J. Heat Transfer*, **123**, 1071-1079, (2001).

[54] S. G. Kandlikar, "A Scale Analysis Based Theoretical Force Balance Model for Critical Heat Flux (CHF) During Saturated Flow Boiling in Microchannels and Minichannels", *Proceedings of the ASME MNHMT 2009,* Shanghai, December 18-21, 2009.

[55] W. K. Kuan and S. G. Kandlikar, "Experimental Study and Model on Critical Heat Flux of Refrigerant-123 and Water in Microchannels", *J. Heat Transfer*, **130,** 034503-1, 2008.

[56] D. Schroeder-Richter, S. Yildiz and G. Bartsch, "Effect of Porous Coating on Critical Heat Flux", *Int. Comm. Heat Mass Transfer*, **23**(4), 1996, 463-471.

[57] M. S. Sarwar, Y. H. Jeong and S. H. Chang, "Subcooled Flow Boiling CHF Enhancement with Porous Surface Coatings", *Int. J. Heat Mass Transfer,* **50**(17-18), 2007,3649-3657.

[58] K. N. Rainey, G. Li and S. M. You, "Flow Boiling Heat Transfer From Plain and Microporous Coated Surfaces in Subcooled FC-72", *J. Heat Transfer*, **123**, 2001, 918-925.

[59] S. Vafaei and D. Wen, "Critical Heat Flux of Subcooled Flow Boiling of Alumina Nanofluids in a Horizontal Microchannel", *J. Heat Transfer*, **132**, 102404.

[60] S. G. Liter, M. Kaviany," Pool-boiling CHF Enhancement by Modulated Porous-layer Coating: Theory and Experiment", *Int. J. Heat and Mass Transfer*, **44**, (2001), 4287-4311.

[61] J. Shen, J. A. Liburdy, D. V. Pence and V. Narayanan, "Droplet Impingement Dynamics: Effect of Surface Temperature during Boiling and Non-boiling Condition", *J. Phys.: Condens. Matter*, **21**, 2009, 464133-464147.

[62] A.L. N. Moreira, A. S. Moita and M. R. Panao, "Advances and Challenges in Explaining Fuel Spray Impingement: How much of Single Droplet Impact Research is Useful?", *Progress in energy and Combustion Science, (2010, doi: 10.1016/j.pecs.2010.01.002).*

[63] A.L. Yarin, "Drop Impact Dynamics: Splashing, Spreading, Receding, Bouncing...", *Annu. Rev. Fluid Mech.,* **38**, 2006, p.159-192.

[64] S. Chandra and C. T. Avedisian, " On the collision of a droplet on a solid surface", *Proc R Soc London A,* **432,** 1991, p.13–41

[65] T. Mao, D.C.S Kuhn, and H. Tran " Spread and rebound of liquid droplets upon impact on flat surfaces" *AIChE J.,* **43**, 1997, p. 2169–2179.

[66] M. Pasandideh-Fard , S. Chandra and J. Mostaghimi , "A three-dimensional model of droplet impact and solidification", *Int. J. Heat Mass Trans,* **45**, 2002, p. 2229–2242.

[67] S. L. Manzello and J. C. Yang, "An Experimental Investigation of Water Droplet Impinged on a Heated Wax Surface", *Int. J. Heat Mass Transfer*, **47**, 2004, p. 1701-1709.

[68] D. Lee, M. F. Rubner, and R. E. Cohen, "All-nanoparticle thin-film coatings", *Nano Letters*, **6** (10) , 2006, pp. 2305-2312.

[69] R. N. Wenzel, "Resistance of solid surfaces to wetting by water", *Ind. Eng. Chem.* , **28** (8), 1936, pp. 988-994.

[70] S. C. Yao and K. Y. Cai, "The dynamics and Leidenfrost temperature of drops impacting on a hot surface at small angles", Exp. Therm. Fluid Sci. , **1**, 1988, pp. 361–371

[71] W. S. Bradfield, "Liquid-solid contact in stable film boiling", *Ind. Eng. Chem. Fundamen.* , **5** (2), 1966, pp. 200-204.

[72] A. L. Biance, C. Clanet and D. Quere, "Leidenfrost Drops", *Physics of Fluids,* **15** (2), 2003, 1632-1637.

[73] J. D. Bernardin and I. Mudawar, " A Cavity Activation and Bubble Growth Model of the Leidenfrost Point", *J. Heat Transfer*, **124**, 2002, pp. 864-874.

[74] Van P. Carey, "Liquid-Vapor Phase-Change Phenomena", 2nd ed., *Taylor & Francis*, New York, 2008, pp. 112-121.

[75] S. M. M. Ramos,† A. Benyagoub, B. Canut, and C.Jamois, " Superoloephobic Behavior Induced by Nanofeatures on Oleophilic Surfaces", *Langmuir*, **26** (7), 2010, p. 5141-5146.

[76] H. Zhao, K.-Y. Law and V. Sambhy, "Fabrication, Surface Properties, and Origin of Superoleophobicity for a Model Textured Surface", *Langmuir*, **DOI:** 10.1021, April 2011.

[77] Y. Gao, Y. Huang, S. Feng, G. Gu and F..-L Qing, " Novel superhydrophobic and highly oleophobic PFPF-modified Silica Nanocomposite", *J. Mater. Science*, **45**, 2010, p. 460-466.

[78] M.S. El-Genk and J. L. Parker, "Nucleate Boiling of FC-72 and HFE-7100 on Porous Graphite at Different Orientations and Liquid Subcooling", *Energy Conversion and Management,* **49**, 2008, p. 733–750.

[79] A. F. Mills, "Heat Transfer", 2nd Edison, p. 328, Prentice Hall, New Jersey, 1999.

[80] N. Zuber, "On the Stability of boiling heat transfer", *Trans. ASME. J. Heat Transfer,* **80**, 3, 1958, p.711 – 720.

[81]B. A. Phillips, "Nano-Engineered the Boiling Surface for Optimal Heat Transfer Rate and Critical Heat Flux", *M.S. Thesis*, 2011, MIT.

[82] S. S. Kutateladze, "On the Transition to Film Boiling Under Natural Convection", *Kotloturbostroenie,* **3**, 1948, p.10.

[83] J. H. Lienhard and V. K. Dhir, " Extended Hydrodynamic Theory of Peak and Minimum Pool Boiling Heat Flux", *NASA CR 2270*, July 1973.

[84] V. P. Carey, " Liquid-Vapor Phase-Change Phenomena", 2nd Ed., Chapter 4 - 7, Taylor & Francis Group, New York, 2008.

[85] Y. Haramua and Y. Katto, "A New Hydrodynamic Model of Critical Heat Flux, Applicable Widely to Both Pool and Forced Convection Boiling on Submerged Bodies in Saturated Liquids", *Int. J. Heat Mass Transfer,* **26** (3), 1983, p.389-399.

[86] Y.-H. Zhao, T. Masuoka, and T. Tsuruta, "Unified Theoretical Prediction of Fully Developed Nucleate Boiling and Critical Heat Flux Based on a Dynamic Microlayer Model", *Int. J. Heat Mass Transfer,* **45**, 2002, p. 3189-3197.

[87] W. Rosenhow and P. Griffith, "Correlation of Maximum Heat Flux Data for Boiling of Saturated Liquids", *Chem. Eng. Prog. Symp. Ser* **52** (18), 1956, p.47-49.

[88] N. I. Kolev, "How Accurately Can We Predict Nucleate Boiling", *Experimental Thermal and Fluid Science,* **10:3,** 1995, p. 370-378.

[89] N. I. Kolev, "The Influence of Mutual Bubble Interaction on the Bubble Departure Diameter", *Experimental Thermal and Fluid Science*, **8**, 1994, p. 167-174.

[90] T. G. Theofanous and T. N. Dinh, "High Heat Flux Boiling and Burnout as Microphysical Phenomena: Mounting Evidence and Opportunities", *Multiphase Science and Technology*, **18** (1), 2006, p. 1-26.

[91] R. N. Wenzel, "Surface roughness and contact angle", *J. Physical Colloid Chemistry*, **53**, 1949, p. 1466-1469.

[92] I. Golobic and K. Ferjancic, "The Role of Enhanced Coated Surface in Pool Boiling CHF", *Heat and Mass Transfer*, **36**, 2000, p. 525-531.

[93] P. J. Berenson, "Experiments on Pool-Boiling Heat Transfer", *Int. J. Heat and Mass Transfer*, **5**, 1962, p. 985-999.
[94] J. M . Ramilison, P. Sadasivan and J. M. Lienhard, "Surface Factors Influencing Burnout on Flat Heater", *J. Heat Transfer*, **114**, 1992, p.287-290.

[95] K. N. Rainey and S. M. You, "Pool Boiling Heat Transfer from Plain and Microporous Square Pin-Finned Surfaces in Saturated FC-72", *J. Heat Transfer*, **122**, 2000, p. 509-516.

[96] H. Honda, H. Takamastu and J. J. Wei, "Enhance Boiling of FC-72 on Silicon Chips with Micro-Pin-Fins and Submicron-Scale Roughness", *J. Heat Mass Transfer*, **124**, 2002, p.383-p.390.

[97] J. J. Wei and H. Honda, "Effect of Fin Geometry on Boiling Heat Transfer from Silicon Chips with Micro-pin-fins Immersed in FC-72", *Int. J. Heat Mass Transfer*, **46**, 2003, p.4059-4070.

[98] A. K. Rajvanshi, J. S. Saini and R. Prakash, "Investigation of Macrolayer Thickness in Nucleate Pool Boiling at High Heat Flux", *Int. J. Heat Mass Transfer*, **35**(2), 1992, p. 343 - 350.

[99] K. S. Udell, "Heat Transfer in Porous Media Considering Phase Change and Capillary", *Int. J. Heat Mass Transfer,* **28**(2), 1985, 485-495.

[100] S. M. Lu and R. H. Chang, "Pool Boiling from a Surface with a Porous Layer", *AiChE Journal*, **33** (11), 1987, 1813-1828.

[101] S. Mori, K. Okuyama, "Enhancement of the Critical Heat Flux in Saturated Pool Boiling Using Honeycomb Porous Media", *Int. Journal of Multiphase Flow*, **35**, (2009), 946-951.

[102] Y. Im, Y. Joshi, C. Dietz and S. S. Lee, "Enhanced Boiling of Dielectric Liquid on Copper Nanowire Surfaces", *Int. J. Micro-Nano Scale Transport*, **1**(1), 2010, p. 79 -95.

[103] S. J. Thiagarajan, W. Wang, R. Yang, S. Narumanchi and C. King, "Enhancement of Heat Transfer with Pool and Spray Impingement Boling on Microporous and Nanowire Surface Coatings", *Proc. 14th International Heat Transfer Conference,* Washington D.C., August 8=13, 2010.

[104] R. Chen, M. Lu, V. Srinivasan, A. Wang, H. Cho and A. Majumdar, "Nanowires for Enhanced Boiling Heat Transfer", *Nanoletter*, **9**(2), 2009, p. 546-553.

[105] C. Li and G. P. Peterson, "Parametric Study of Pool Boiling of Horizontally Microporous Coated Surfaces", *J. Heat Transfer*, **129**, 2007, p. 1465-1475.

[106] R. E. Pivovar, "High Temperature Microporous Coating: The Effects of Wetting and Wicking on Nucleate Boiling and CHF", *Master Thesis*, May 2009, University of Texas Arlington.

[107] J. Tehver, H. Sui and V. Temkina, "Heat Transfer and Hysterisis Phenomena in Boiling on Porous Plasma-Sprayed Surface", *Experimental Thermal Fluid Science*, **5**, 1992, p. 714-727.